CONTROLLED PROTEIN ADSORPTION FOR MICROIMMUNOASSAYS

THÈSE N^{O} 3419 (2006)

PRÉSENTÉE À LA FACULTÉ SCIENCES DE BASE

Institut des sciences et ingénierie chimiques

SECTION DE CHIMIE ET GÉNIE CHIMIQUE

ÉCOLE POLYTECHNIQUE FÉDÉRALE DE LAUSANNE

POUR L'OBTENTION DU GRADE DE DOCTEUR ÈS SCIENCES

PAR

Andrea LIONELLO

laurea in chimica, Università degli studi di Genova, Italie
de nationalité italienne

acceptée sur proposition du jury:

Prof. H. Girault, directeur de thèse
Dr E. Delamarche, rapporteur
Dr A. Fisher, rapporteur
Prof. Ph. Renaud, rapporteur

Lausanne, EPFL
2006

Thanks (random order):

Léa Loïc Hubert Leonardo Verdi

Chris la mamma Bin Maria Hugh

Michel Greg Christophe Henrik

Anita Laura Daphne

Celeste Massi Joseph Valérie Anna C. Häusler (amersham biosciences) Jacqueline

Matthieu Laura Nicolas H. Stone P.-A. Thonney (GMP SA)

Momo Giovanni Sorina Xiao Xia Elisa

Guccini Chris tophe la sorella

Felicie Daniela Niels Maurizio

Erika Chen

Giovanni

Nicolò Jacques Ste Mannoia

...Ci muoviamo in un pulviscolo

madreperlaceo che vibra,

in un barbaglio che invischia

gli occhi e un poco ci sfibra.

Eugenio Montale - *Ossi di seppia*

"Too little signal compared to the noise: the problem kept frustrating me."

Marvin Minsky

...e sono lì, che miagolo nel buio e cerco una risposta,

e poi ti arriva la risposta, la risposta finalmente arriva...

...epperò è sbagliata!

Rocco Smitherson

"Boh!"

Andrea L., martedì pomeriggio, aprile 2002 e giovedì mattina, maggio 2003

Abstract

This dissertation addresses the adsorption of proteins in microchannels with the aim of improving the result of an immunoassay. To observe the adsorption of fluorescently labelled immunoglobulins G in laser ablated polymer microchannels, a confocal microscope was built. By optically scanning the specimen, and observing one focal plane at time, this tool allows for a high signal-to-background, which leads to a low limit of detection (10^{-9} M).

A numerical model for the adsorption kinetics of proteins on the walls of a microchannel has been developed using the finite element method (FEM). The model illustrates the adsorption limitation sometimes observed when the microdimensions of these systems induce a global depletion of the bulk solution. A new non-dimensional parameter is introduced to predict the final value of the coverage of any microsystem under static adsorption. A working curve and a criteria ($h/K\Gamma_{max} > 10$) are provided in order to choose, for given adsorption characteristics, the value of the volume-to-surface ratio (*i.e.* the channel height h) avoiding depletion effects on the coverage (relative coverage at least 90% of the theoretical one).

Simulations were compared with confocal microscopy measurements of IgG antibody adsorption on the walls of a PET (poly(ethylene terephthalate)) microchannel. The fit of the model to the experimental data show that the adsorption is under apparent kinetic control.

Two ways of loading proteins on microchannel surfaces for immunological applications have been analysed with the FEM model: the "stop-flow" and the continuous flow processes. The "stop-flow" method consists of successive static incubation periods where the bulk solution depletes upon the adsorption process. A multi-step "stop-flow" protein coating is studied and compared to a coating under continuous flow conditions. For the "stop-flow", a non-dimensional

parameter is here introduced, indicating the adsorbing capacity of the system, by which it is possible to calculate the number of loads necessary to reach the optimum coverage.

For the continuous flow, the effects on the adsorption of the kinetic rates, flow velocity and wall capacity have been considered. This study shows the importance of a careful choice of the fluid velocity to minimise the sample waste. For diffusion controlled and kinetics controlled processes, two flow velocity criteria are provided in order to obtain the best possible coverage, with the same amount of sample as with the "stop-flow".

Surface modifications have been conceived in order to improve the adsorption and the activity of the physisorbed antibodies. The microchannels have been coated with titania nanomaterials, chosen because of their biocompatible properties. Crystalline and amorphous TiO_2 have been used and the adsorption with respect to the native PET was improved by 3 times. A study of adsorption as a function of the pH solution and different ionic strengths has been done in order to infer the forces acting during the adsorption: it was found that hydrophobic forces helped by electrostatic ones occur during IgG adsorption onto titania phases.

The "stop-flow" method was employed to coat the TiO_2 modified microchannels with the capture antibodies and improve the result of a microimmunoassay. When strong adsorbing phases are used, the limit of detection of the assay was lowered by one order of magnitude.

The FEM model was used to obtain the kinetic rates of adsorption and desorption of IgG antibodies on PET with a novel biosensor conceived in this lab, which measures capacitive changes in the surface microchannel while the adsorption takes place. As the FEM model foresees a three-dimension region where the adsorption might take place, it can be used to study the adsorption in TiO_2 gels developed in our lab.

Résumé

Ce travail de thèse s'interesse à l'adsorption de protéines dans des microcanaux dans le but d'améliorer le résultat d'un immunoassay. Pour observer l'adsorption des immunoglobulines G dans des microcanaux polymériques un microscope confocal a été construit. Cet instrument permet de sectionner optiquement le spécimen, en observant un plan focal à la fois. On obtient ainsi un intense signal par rapport au bruit de fond, ce qui mène à une basse limite de détection (10^{-9} M). Un modèle numérique pour la cinétique d'adsorption des protéines sur les parois d'un microcanal a été développé en utilisant la méthode des éléments finis (FEM). Le modèle illustre la limitation d'adsorption parfois observée quand les microdimensions de ces systèmes induisent un épuisement global de la solution. Un nouveau paramètre adimensionnel est présenté pour prévoir la valeur finale de la couverture de n'importe quel microsystème sous adsorption statique. Un critère ($h/K\Gamma_{max} > 10$) est fournis afin de choisir, pour des caractéristiques données d'adsorption, la valeur du rapport de volume-à-surface (c.-à-d. la taille du canal h) évitant des effets d'épuisement sur la solution (couverture relative au moins 90% que la théorique). Les simulations ont été comparées aux mesures par microscopie confocale de l'adsorption d'IgG sur les parois d'un microcanal en PET (poly(ethylene terephthalate)). L'interpolation du modèle aux données expérimentales prouve que l'adsorption s'effectue sous contrôle cinétique. Deux manières de charger des protéines sur des surfaces de microcanal pour des applications immunologiques ont ensuite été analysées avec le modèle FEM : le "stop-flow" et l'écoulement continu. Le "stop-flow" se compose des périodes successives d'incubation statique où la solution s'épuise via le processus d'adsorption. Une couverture de protéines obtenue par "stop-flow" successifs est étudiée et comparée à une couverture obtenue avec l'écoulement continu. Pour le "stop-flow", un paramètre adimensionnel est présenté. Il permet d'indiquer la capacité

adsorbante du système. Il est alors possible de calculer le nombre de charges nécessaires pour atteindre la couverture optimale. Pour l'écoulement continu, les effets sur l'adsorption des constantes cinétiques, de la vitesse d'écoulement et de la capacité de la paroi ont été considérées. Cette étude montre l'importance d'un choix soigneux de la vitesse de la solution afin de réduire au minimum la perte de reactif. Concernant les contrôles diffusionel et cinétique, deux critères pour la vitesse d'écoulement sont fournis afin d'obtenir la meilleure couverture, avec la même quantité de solution qu'avec le "stop-flow".

Des modifications de surface ont été conçues afin d'améliorer l'adsorption et l'activité des anticorps adsorbés. Les microcanaux ont été recouverts par des nanomatériaux de TiO_2, choisi en raison de leurs propriétés biocompatibles. Les TiO_2 cristallin et amorphe ont été employés et l'adsorption dans un microcanal a été améliorée par 3 fois. Une étude de l'adsorption en fonction du pH et des différentes concentrations ioniques a été faite afin d'evaluer les forces agissant pendant l'adsorption.

La méthode "stop-flow" a été utilisée pour accrocher des anticorps de capture sur les parois des microcanaux modifiés et pour améliorer le résultat d'un microimmunoassay. Quand des phases adsorbantes fortement sont employées, la limite de la détection de l'analyse a été abaissée par un ordre de grandeur.

Le modèle FEM a été employé pour obtenir les vitesses d'adsorption et de désorption des anticorps d'IgG sur de microcanaux en PET, par mesure de capacitance avec un nouvel biodétecteur conçu dans ce laboratoire. Comme le modèle FEM prévoit une région tridimensionnel où l'adsorption pourrait avoir lieu, ce dernier peut être employé pour étudier l'adsorption dans des gels de TiO2 développés au laboratoire.

Table of Contents

Controlled Protein Adsorption for Microimmunoassays

Introduction

1.1 From Babylonia to Immunoassays

Yesterday, as I was browsing a booklet from the city library of Lausanne, some lines and illustrations about the history of documents, from the clay tablets of Babylonia (Fig. 1.1) to the modern DVD, struck me. They were vague lines about the magic virtues or simply the usefulness of writing. However, it astonished me that of all the things to say about these different kinds of documents, what was underlined were the density of signs per cm^2 and the duration of each

Figure 1.1. Photo of a cuneiform tablet from the Archaeological Museum of Baghdad.

A. D. 1374. — **Xenophon,** Anabasis, lib. III.
Mediol. Biblioteca Ambrosiana, A. 18. parte inferiore, fol. 39.

Figure 1.2. Manuscript of the Anabasis (1374), by Xenophon, Milan, Biblioteca Ambrosiana.

document. So I learnt that in an Egyptian papyrus (about 200 b.C.) we can find 1 sign per cm^2 and it can last 5000 years; that a medieval manuscript like the one depicted in Fig. 1.2 (XIII century) has 15 signs per cm^2 and it lasts 1000 years; a newspaper (XIX century) 25 signs/cm^2 and we can read it for 100 years, while an "old" floppy disk has 20000 "signs" and a "modern" DVD 500 000 000 and they are supposed to last 15 and 10 years respectively. And yet we cannot reach the density of signs/cm^2 (whatever it means) achievable in our brain, lasting, unfortunately (or not?) one life.

Anyway, documents have become denser, so that they can be smaller and more practical and portable. And they last less time: do people today say things that are less important than the things said by the Babylonians?

The same path towards small dimensions (and short times) can be perceived in many technology domains (if we agree that clay tablets are a first form of technology). The first cuneiform sign was engraved in the stone of immunoassays by Rosalyn Yalow and Solomon Berson. Immunoassays are exquisite analytical tests that use antibodies, so that it is nature that provides us the fundamental tools we use to study biological processes. An immunoglobulin G antibody is schematically represented in Fig. 1.3. Immunoassays derive their unique characteristics from three important properties of antibodies: 1-their ability to bind to an extremely wide range of natural and manmade chemicals, biomolecules, cells and viruses. This is because antibodies are proteins, and the binding sites are derived from a huge number of potential combination of amino acid sequences; 2-exceptional specificity for the substance, called antigen, to which each antibody binds; 3-the strength of the binding between an antibody and its target.

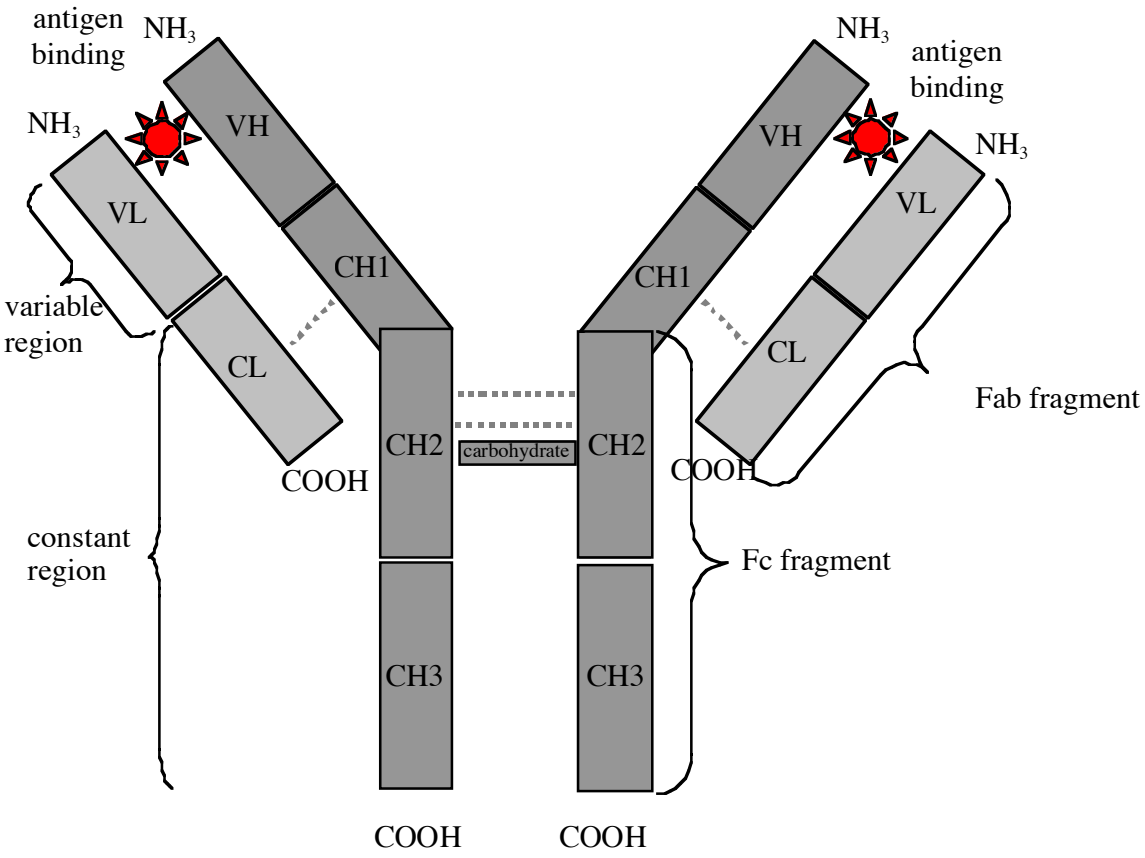

Figure 1.3. Scheme of an immunoglobulin G molecule. The heavy chain is in heavy gray; the light chain is in light gray. The dotted lines represent the disulfide bridges connecting the heavy to the light region and the two heavy regions together. Among the different domains composing the antibody, we can notice the variable region, made up by a domain in the light and one in the heavy chain. The two "arms" of the molecule are the antigen-binding fragment.

1.2 Towards the first immunoassay *(homogeneous radioimmunoassay)*

Yalow and Berson performed the first immunoassay, a radioimmunoassay (RIA) for insulin. It was not a sudden discovery but the results of years of research on diabetes. At the beginning of the 50's, Mirsky[1] had hypothesised that diabetes might not be due to a deficiency of insulin secretion, but rather to an abnormally rapid degradation of insulin by hepatic insulinase. To check this hypothesis, Yalow and Berson studied the metabolism of I^{131}-labelled insulin in patients who had already received insulin in the past (both for treatment of diabetes or as a shock

therapy for schizophrenia – the 50's were years of pioneering in many domains and in many ways!), observing that insulin disappeared more slowly from their organism than from the plasma of patients who never received insulin.[2] The suspicion arose that the delay in the disappearance of insulin was due to the binding of insulin to antibodies that had developed in response to the administration of exogenous insulin. As classical immunological techniques were not sensible enough at that time, they introduced radioisotopic methods with high sensitivity.

At that time Rosalyn Yalow was a health physicist at the Veterans Administration Hospital in the Bronx. Looking beyond the atomic bombing of Hiroshima, she became adsorbed with the potential of radioactivity in medicine. Berson succeeded in enrolling in New York University Medical School (after 109 medical school rejections). Radioactivity in medicine was the leitmotif of their research.

With radioactivity they detected the antiinsulin-insulin complexes and demonstrated the ubiquitous presence of insulin-binding antibodies in insulin treated patients. The paper describing these findings[2] was rejected by Science and initially rejected by the Journal of Clinical Investigation: when awarded the Nobel Prize for medicine in 1977, Rosalyn Yalow entertained the audience with the story of this rejection.[3] The concept purported about by that paper was too far ahead for the immunologists of the 50's, so that, in order to publish, they had to change "insulin transporting antibody" with "insulin binding globulin" in the title, and they had to document that the binding globulin was indeed an antibody by showing how it met the definition of antibody given in a standard textbook of bacteriology and immunity: theirs was a difficult revolution, as they had to upset the classical concepts using the widely accepted bases.

What was difficult to accept at that time was that small proteins like insulin and small peptides such as vasopressin and oxytocin are antigenic in some species, and that the equilibrium

constants for the antigen-antibody reaction can be as great as 10^{12} litres per mole. Today antibodies are produced for most different molecules, as small as caffeine and trinitrotoluene.

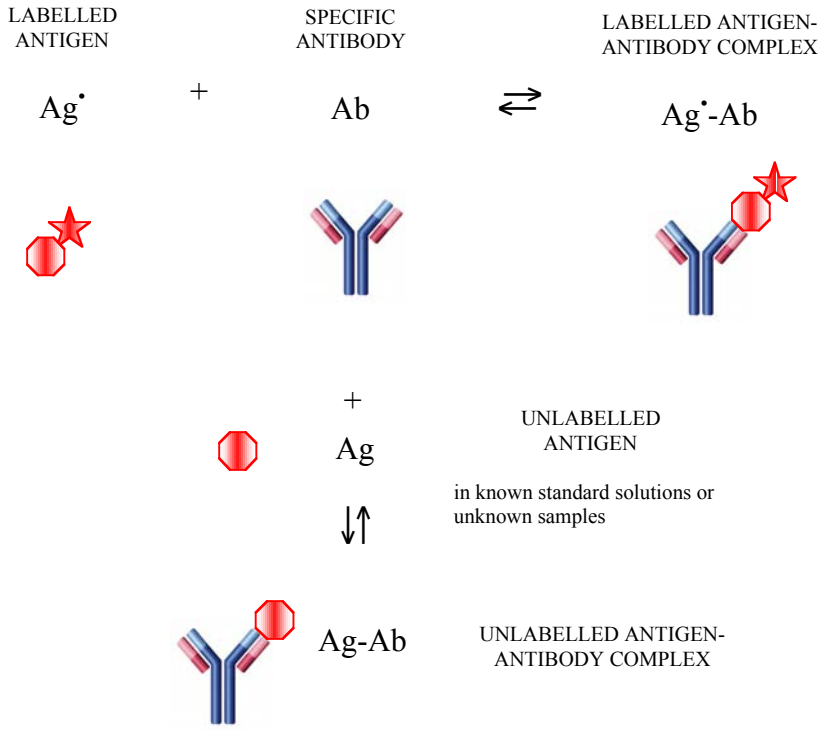

Figure 1.4. Competing reactions that form the basis of radioimmunoassay (RIA). Adapted from Yalow R. S. (1977).

In that paper they also reported that the binding of labelled insulin to a fixed concentration of antibody is a quantitative function of the amount of insulin present, thus posing the bases for the radioimmunoassay in plasma. Years of research and experiments had yet to pass before the theoretical concepts could be translated into an immunoassay.

Radioimmunoassay is simple in principle. The competing reactions that form the basis of RIA are shown in Fig. 1.4. The concentration of unknown unlabelled antigen is obtained by comparing its inhibitory effect on the binding of radioactively labelled antigen to the specific antibody with the inhibitory effect of known standards. The validity of RIA (as well as of all the

other kind of competitive immunoassays, as we will see) is dependent on the identical immunological behaviour of the antigen in unknown samples with the antigen in known standards. The immunogenic reaction is so specific that it can permit ready distinction, for instance, between corticosterone and cortisol, steroids which differ only in the absence of or presence of respectively a single hydroxyl residue, or caffeine and theophylline, differing in just one methyl group.

The cascade reactions following a revolution are often many and unpredictable. RIA clarified our understanding of diabetes and the physiology of glucose homeostasis. It demonstrated that type 1 diabetes was an insulin deficient state, whereas type 2 was characterised by a resistivity to insulin.[4] Berson and Yalow demonstrated also that sometimes obesity can be associated with hyperinsulinemia and insulin resistance.[5]

Radioimmunoassay was applied to many diverse areas in biomedical investigation and clinical diagnosis. Up to the seventies RIA was still much used. However, it has been slowly replaced by fluorescent immunoassay, which has high sensitivity and an obvious advantage in safety. On the annual report of an immunoassay company it was related that their market of RIA decreased by only 11% from 1977 to 1999 (while the sales for their system for chemiluminescence increased linearly with the years).

1.2.1 Homogeneous and heterogeneous immunoassays

Today, an incredible number of different types of immunoassay exists, with different configurations, exploiting the most diverse principles for detection. The variety of assay types stems from the advantages of each for different types of analytes and samples.

In this dissertation heterogeneous assays will be treated, *i.e.* assays in which the antigen or the antibody is bound to a support. Solid phase (heterogeneous) immunoassays (SPI) were

introduced by Catt and Tregear in 1967.[6] SPI has become one of the most used kinds of immunoassay. The principle of SPI is based on the ability of antibody-coated polymers to bind an antigen. The materials originally used for the support were poly-(tetrafluoroethylene-*g*-isothiocyanatostyrene)[7] or sephadex-isothiocyanate[8] but it soon became apparent that some unsubstituted polymers like polypropylene and polystyrene may adsorb antibodies that can then bind an adequate quantity of antigen. Until Catt and Tregear immunoassays were performed in the homogeneous way.

1.2.2 Sandwich and competitive immunoassays

Homogeneous and heterogeneous immunoassays can also be classified as unlabelled and labelled ones. Labels are molecules attached to the antibody or the antigen allowing the detection, as they normally are fluorescent or radioactive. When no label is used, secondary immune reactions such as precipitation and agglutination are used. The labelled immunoassays can be divided into sandwich (or "two site assay") and competitive. There is a lack of agreement on the denomination of competitive immunoassay, so that the definitions of "type I-reagent observed" for the sandwich and "type II-analyte-observed" for the competitive immunoassay are preferred. The classical configuration for the "type I" is with the capture antibody bound to a surface, which binds the antigen, which, in turn binds a labelled antibody. Clearly, to perform this assay, the antigen must be big enough to bind to two different antibodies. The maximal sensitivity is attained as the amount of capture antibodies on the support approaches infinity, for which femtomolar detection limit of antigen can be detected; the theoretical sensitivity of the assay is one molecule of analyte; the antigen-antibody reaction is less influenced by substances such as salt and urea; the assay time is relatively rapid. An advantage of this technique is also the

enhanced specificity obtained from two separate recognition steps provided by the two antibodies that are generally selected to recognise two different epitopes on the antigen.

"Type II" assay is basically the one invented by Berson and Yalow and it can be used to quantitate both substances of high molecular weight and haptens (a small separable part of an antigen that reacts specifically with an antibody). To have the maximal sensitivity, the concentration of the capture antibody must be the lowest possible, in order to give way to the competition between the labelled and the non-labelled antigen. However, the sensitivity of the assay is dependent upon the affinity constant of the antibody: theoretically it is about 10^{-14} M, two orders of magnitude higher than with a "sandwich assay".[9] The assay reaction is slow since equilibrium must be reached.

The first choice normally falls onto the "type I", both for the sensitivity and for the time-to-result. Of course, when the antigen is too small (less than 1000 Da) or the two epitopes are too close to each other to allow two antibodies to bind, a "type II" assay is the only choice we have. Further subclassifications come in play depending on the size of the immunogenic couple antigen-antibody, their affinity, and the species in which the antibodies are raised. For instance, six kinds of different "type II" assays can be performed,[10-15] and even subtler subdivisions are possible. [16, 17]

Today, one of the most used kind of immunoassay is the enzyme linked immunosorbent assay (ELISA) born with the aim of amplifying the signal of the test thanks to an enzyme covalently linked to the antigen, generating a fluorescence probe. The enzyme should permit fluorimetric, luminometric or colorimetric measurements. The enzymes of choice are normally alkaline phosphatase (ALP) and peroxidase. The first removes 5' phosphate groups from DNA and RNA, but also from nucleotides and proteins; the second catalyses a reaction in the form ROOR' +

electron donor ($2e^- + 2H^+$) → ROH + R'OH. The substrates normally used are the *p* – nitrophenyl-phosphate (PAPP) for ALP and H_2O_2 / 3,3',5,5'-tetramethylbenzidine (TMB) for the second. In both cases a fluorescent molecule that can be detected at 405 and 450 nm, which is also electroactive, is produced. In general, they increase the detection limit of a sandwich immunoassay by 2-10 times, which permits a visual evaluation in large-scale screenings.

1.2.3 Microimmunoassay: a door opened to better performance and new research domains

An obvious breakthrough of immunoassays is towards high throughput analysis, shorter times for the response, less amount of reagents used…all that leads to talk about miniaturisation. Widman and his group at Ciba Geigy sowed the seed for a miniaturised total chemical analysis system (μTAS) in 1990[18] rendering clear the advantages of miniaturisation (and eventually the results have given him reason). Evolving towards "micro", heterogeneous immunoassays benefit from the high surface-to-volume ratio in the microchannel, and homogeneous assays typically take advantage of the multiplexing and very fast electrophoretic separations made possible by microchip format.

Inevitably, with the advantages, the problems raised, stimulating other domains of research. For instance in Fig. 1.5 the detection limits as a function of the detection volume for different techniques are reported.[18] It is clearly shown that μTAS requires very sensitive techniques to have the same limit of detection as for larger systems.

All the detection techniques for microimmunoassays can be divided into optical and electrochemical. The most commonly observed form of detection is fluorescence, primarily due to its high sensitivity and ease of integrating a label.[15] Fluorescein based probes were very used until recently, but the research in fluorolabels has resulted in products that have extraordinary characteristics like low photobleaching, high quantum efficiency when bound to proteins or

nucleic acids, pH insensitivity allowing maintenance of fluorescence intensity over a broad range, unlike fluorescein which loses fluorescence below pH 8.0.

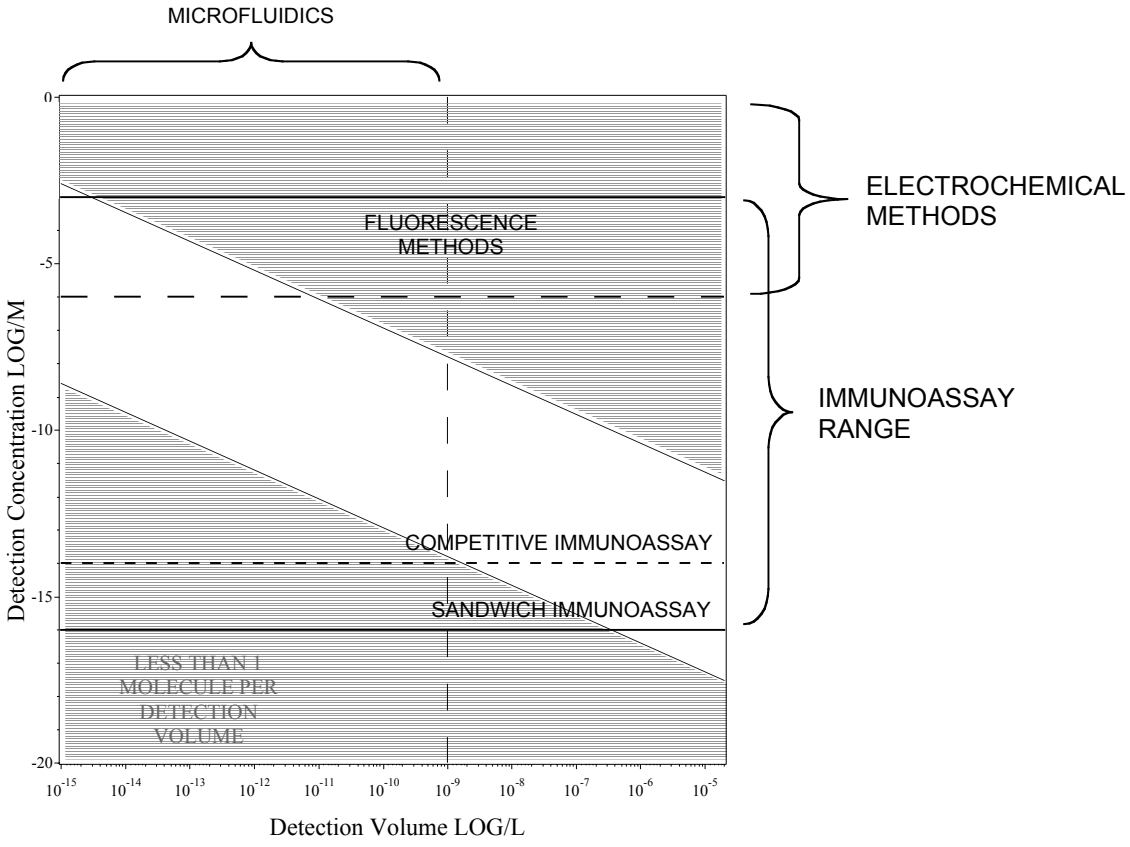

Figure 1.5. Detection limits as a function of the detection volume for electrochemical and fluorescence methods. The range of detection for immunoassays is shown, with the limits for competitive and sandwich immunoassays. The area at the bottom left corner represents the concentrations at which less than 1 molecule per volume of detection occurs.

A promising type of fluorescence is fluorescence polarisation, which detects the change in anisotropy caused by the slower rotation of bound with respect to the free label. [19] Chemiluminescence, which requires no external light, and light scattering are other ways of exploiting light for detection. [20-24]

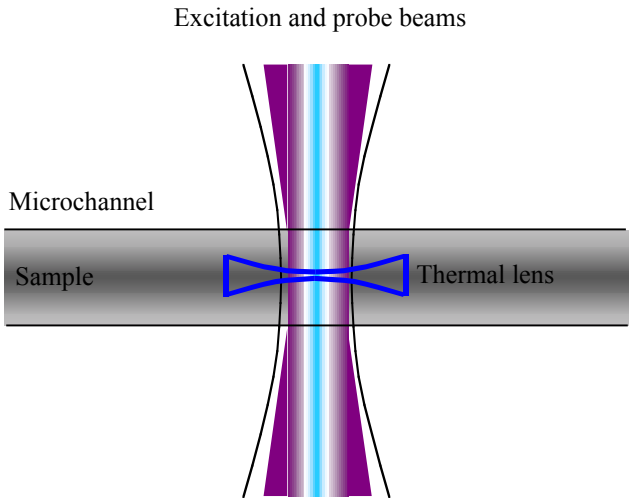

Figure 1.6. The coaxial excitation and probe beams are focused into the liquid sample causing localized temperature increase. The refractive index of the material is thus modified in such a way that the medium behaves as a lens by temperature increase of the material: this is the "Thermal Lens Effect". Since the size of thermal lens linearly depends on the amount of the absorbed molecules, quantitative analysis can be carried out by measuring the probe beam divergency.

Kitamori applied the thermal lens concept in microimmunoassays.[25] The thermal lens effect (see Fig. 1.6), discovered by Gordon et al.,[26] is a photothermal effect and results when energy from a laser beam passing through a sample is absorbed, causing heating of the sample along the beam path. The lens is created through the temperature dependence of the sample refractive index. The lens usually has a negative focal length since most materials expand upon heating and the refractive index is proportional to the density. This negative lens causes beam divergence and the signal is detected as a time dependent decrease in power at the centre of the beam. With this tool, detecting the secondary antibody conjugated with colloidal gold, secretory human immunoglobulin A,[27] carcinoembrionic antigen,[28] and interferon-γ[29] were successfully determined with good sensitivity, reducing the time-to-response from tens of hours to some minutes.

Electrochemistry is the other detection branch for immunoassays, and among all the electrochemical techniques, voltammetry is the one of choice since its performance improves when using microelectrodes.[30, 31] In the micrometer range, in fact, a shift from planar to non-planar (*e.g.* hemispherical) diffusion occurs, causing an increase in the collection efficiency of the electroactive species at the surface. [32] The practical result is an increase in the signal-to-noise ratio, which generally translates into a lower detection limit. Our lab presented a sandwich immunoassay for the detection of the D-dimer, an important element of the blood coagulation mechanism, performed in a disposable polyethylene terephthalate (PET) microfluidic chip.[33]

1.3 Proteins onto Surfaces

The surface activity of proteins is a fundamental property of these complex macromolecules that derives from their large size, amphipathic nature, and the many types of chemical interactions that can occur between proteins and surfaces. Therefore, interfaces of almost any type that come into contact with protein solutions tend to become quickly occupied by proteins, leading to profound alterations in the physicochemical and biological properties of the interfaces. Proteins at interfaces are important in many applied areas, including separation and purification, the biocompatibility of biomaterials, mammalian and bacterial cell adhesion, blood coagulation at solid and membrane surfaces and, of course, solid phase immunoassays and biosensor development. Despite a fairly long history of study of proteins at interfaces, many of the fundamental mechanisms remain only partly understood, and research on proteins at interfaces remains very active.[34]

Protein surface adsorption was already under study to find blood-compatible plastics[35] when the first heterogeneous immunoassays came out. In the 1960's thrombogenicity of plastics was

already known as the major drawback to their use in artificial organs in contact with blood, and surface modifications were already envisaged to avoid clot events.[36, 37]

Heterogeneous immunoassay have profited from the know-how of that time and triggered further studies in antibody adsorption on different surfaces. The goals to reach in immunoassays and medical devices are opposite: while in the first case good adsorption is needed to improve the final response, in the latter adsorption is to be avoided, or possibly, just the proteins that could render the prosthesis compatible (like heparin) are to be adsorbed.

Surface modifications to enhance the adsorption of the capture antibodies must also keep into account the denaturation of the antibody due to the adsorption process.[38] In 1992 Butler said that "in the area of SPI, the technological cart is ahead of the scientific horse". Actually, he observed that immunoassay technology has had already expanded, largely because of convenience and simplicity, without regard for an understanding of the immunochemistry of those antigen-antibody interactions which occur in close proximity to hydrophobic, synthetic solid phases to which one reactant has been immobilised, most typically by passive adsorption. The activity of adsorbed antibodies, in fact, is found to be even less than 1% of the original one.

The best solutions for this problem seemed to be the binding of the antibodies to the surface through the avidin-biotin system.[39] In any case the best stability and sensitivity are achieved when antibodies are covalently attached to a polymer.[40]

In miniaturised systems, non-specific binding effects can easily become a dominant and limiting factor. In addition, the amount of reagent immobilised is relatively low as compared to "macro" systems and thus, the stability of the biological reagents becomes of paramount importance. The problem of the non-specific binding was brilliantly resolved[39] by depositing sequentially a biotinylated Immunoglobulin G IgG, neutravidin and biotinylated dextran. The resulting

hydrophilic surface easily resists the adsorption of proteins. In addition, the dextran surface layer can be replaced by any biotinylated probe or antibody to efficiently functionalise the surface. Beads have also been used because they can dramatically increase the surface area in a small fluid volume.[28, 41] Polystyrene beads with a paramagnetic iron core can be collected by a magnet for the detection, after the capture step.[42-46]

1.4 Computational Models for Immunoassays

We can now imagine that setting up a novel immunoassay can be time consuming and expensive. Modelling can help by saving both time and money, predicting the optimal conditions (antigen concentration, primary and secondary antibody titers, and time for chromogen development) for the linear dependence of absorbance on antigen concentration. An enormous number of models are created to predict, simulate and improve immunosystems, especially in the immunosensor domain. The microdimensions and the fluidics add even more parameters to the study.

Computational models in immunology first arose to describe the antigen-antibody interaction.[47] The phrase "computational model" does not have a simple definition. "Model" implies a simplification of the system under study, while "computational" entails the use of some form of quantitative technique to deduce information relating to the system. The use of a computational model involves an attempt to use both data gathered and assumptions and knowledge of the system under study to infer additional information regarding the system. If the assumptions are true and the model was carefully constructed, the predictions of the model should be eventually observed, or the experiments can be planned on the base of these predictions. I have to add the depressing note by Merrill[48] that "verifying the predictions does not prove that the assumptions are true, only that they may not be inconsistent with observations". In the study of a complex

system, such as an immunosystem, models are essential even if they can be very simple. If a model, based on a collection of hypotheses and assumptions, reveals that there are no contradictions between these hypotheses, it means that these assumptions are at least sufficient to specify a simplified version of the system. Then, the assumptions and the purpose of the model must be evaluated critically, as well as the reasonableness of the results obtained from applying the model. A comprehensive bibliography on models for protein adsorption and immunosensors is presented in the following chapters.

1.5 Thesis plan

In this dissertation, adsorption of proteins in microchips is studied by a confocal microscope built-on-purpose, and laser induced fluorescence. A finite element model (FEM) has been implemented to simulate the systems studied and find new ways to coat microchannels in order to have an efficient immunoassay. Surface modifications have also been developed in this aim.

In particular, in chapter 2 it is described how the confocal microscope was conceived and built. As we have just seen, fluorescence detection is the method of choice for microsystems because of its high sensitivity. Confocal microscopy enhances this aspect of fluorescence. The samples are “optically sectioned”, so that the background signal can be rejected, obtaining high signals compared to the background.

In chapter 3 the FEM model is described and calibrated on the Langmuir assumptions, which are the most general and those with which a lot of systems can be studied by simply changing the base assumptions (many derivations from the Langmuir assumptions can be found[49-51]). Adsorption in microsystems is studied and the huge amount of data obtained from simulations is

gathered to draw a picture of the effects of the microsystem surface-to-volume ratio on the protein adsorption.

In chapter 4 two ways of coating microchannels in view of an immunoassay are described. The continuous flow is normally used in microfluidic systems, as it allows hyphenation with numerous other techniques. The "stop-flow" method consists on stopping the flow to allow the analyte more time to diffuse to the active wall. It was proposed in 1962,[52] mainly in chromatography[53-55] and its effect on the analyses has been studied.[52,56] The "stop-flow" methodology is here simulated in a multi-step way and the adsorption obtained is compared with that obtained in flowing conditions.

In chapter 5 a study of protein adsorption on TiO_2 coated microchannels is presented. The detection is done by way of the confocal microscope. TiO_2 is very interesting for its biocompatible characteristics. Normally, protein adsorption is studied in macro-systems. With this study the behaviour of TiO_2 microchannels is already at hand for immuno-applications (and it allows to save a lot of money, as labelled fluorescent molecules are very expensive). The effects of the sorbent phase on the activity of the antibody are observed.

In chapter 6 the "stop-flow" method is applied to immunoassays performed in TiO_2 modified microchannels. The results are compared to those obtained in non-coated PET microchips without "stop-flow", especially in terms of the final sensitivity of the tests.

As with the confocal microscope it was difficult to observe the protein adsorption in "real-time" under flowing condition, in chapter 7 the FEM model is used to interpret data obtained in flow conditions with a new technique (Super-Capacitance-Admittance-Tomoscopy) developed in our lab to study protein adsorption and bioreactions in microsystems. The FEM model is flexible enough to describe different systems, enabling their deeper knowledge.

References:

(1) Mirsky, I. A. *Recent Progress in Hormone Research* **1952**, *7*, 437-467.

(2) Berson, S. A.; Yalow, R. S.; Bauman, A.; Rothschild, M. A.; Newerly, K. *Journal of Clinical Investigation* **1956**, *35*, 170-190.

(3) Yalow, R. S. *Science* **1978**, *200*, 1236-1245.

(4) Yalow, R. S.; Berson, S. A. *Journal of Clinical Investigation* **1960**, *39*, 1157-1175.

(5) Yalow, R. S.; Glick, S. M.; Roth, J.; Berson, S. A. *Annals of the New York Academy of Sciences* **1965**, *131*, 357-&.

(6) Catt, K.; Tregear, G. W. *Science* **1967**, *158*, 1570-&.

(7) Catt, K.; Niall, H. D.; Tregear, G. W. *Biochemical Journal* **1966**, *100*, C31-&.

(8) Wide, L.; Porath, J. *Biochimica Et Biophysica Acta* **1966**, *130*, 257-&.

(9) Wild, e. D. *The immunoassay handbook*, 3rd ed. ed.; Elsevier: Amsterdam, 2005.

(10) Rowley, G. L.; Rubenstein, K. E.; Huisjen, J.; Ullman, E. F. *Journal of Biological Chemistry* **1975**, *250*, 3759-3766.

(11) Gibbons, I.; Skold, C.; Rowley, G. L.; Ullman, E. F. *Analytical Biochemistry* **1980**, *102*, 167-170.

(12) Haga, M.; Sugawara, S.; Itagaki, H. *Analytical Biochemistry* **1981**, *118*, 286-293.

(13) Burd, J. F.; Wong, R. C.; Feeney, J. E.; Carrico, R. J.; Boguslaski, R. C. *Clinical Chemistry* **1977**, *23*, 1402-1408.

(14) Morris, D. L.; Ellis, P. B.; Carrico, R. J.; Yeager, F. M.; Schroeder, H. R.; Albarella, J. P.; Boguslaski, R. C.; Hornby, W. E.; Rawson, D. *Analytical Chemistry* **1981**, *53*, 658-665.

(15) Bange, A.; Halsall, H. B.; Heineman, W. R. *Biosensors & Bioelectronics* **2005**, *20*, 2488-2503.

(16) Carrico, R. J.; Christner, J. E.; Boguslaski, R. C.; Yeung, K. K. *Analytical Biochemistry* **1976**, *72*, 271-282.

(17) Litman, D. J.; Hanlon, T. M.; Ullman, E. F. *Analytical Biochemistry* **1980**, *106*, 223-229.

(18) Manz, A.; Graber, N.; Widmer, H. M. *Sensors and Actuators B-Chemical* **1990**, *1*, 244-248.

(19) Kakehi, K.; Oda, Y.; Kinoshita, M. *Analytical Biochemistry* **2001**, *297*, 111-116.

(20) Stabler, T. V.; Siegel, A. L. *Clinical Chemistry* **1991**, *37*, 1987-1989.

(21) Aoyagi, S.; Iwata, T.; Miyasaka, T.; Sakai, K. *Analytica Chimica Acta* **2001**, *436*, 103-108.

(22) Bouve, J.; Deboever, J.; Leyseele, D.; Vandekerchkhove, D. *Analytica Chimica Acta* **1991**, *255*, 417-422.

(23) Erhard, M. H.; Jungling, A.; Brendgen, S.; Kellner, J.; Losch, U. *Journal of Immunoassay* **1992**, *13*, 273-287.

(24) Papsidero, L. D.; Dittmer, R. P.; Vaickus, L.; Poiesz, B. J. *Journal of Clinical Microbiology* **1992**, *30*, 351-358.

(25) Harada, M.; Iwamoto, K.; Kitamori, T.; Sawada, T. *Analytical Chemistry* **1993**, *65*, 2938-2940.

(26) Gordon, J. P.; Leite, R. C. C.; Moore, R. S.; Porto, S. P. S.; Whinnery, J. R. *Journal of Applied Physics* **1965**, *36*, 3-8.

(27) Sato, K.; Tokeshi, M.; Odake, T.; Kimura, H.; Ooi, T.; Nakao, M.; Kitamori, T. *Analytical Chemistry* **2000**, *72*, 1144-1147.

(28) Sato, K.; Tokeshi, M.; Kimura, H.; Kitamori, T. *Analytical Chemistry* **2001**, *73*, 1213-1218.

(29) Sato, K.; Yamanaka, M.; Hagino, T.; Tokeshi, M.; Kimura, H.; Kitamori, T. *Lab on a Chip* **2004**, *4*, 570-575.

(30) Ewing, A. G.; Dayton, M. A.; Wightman, R. M. *Analytical Chemistry* **1981**, *53*, 1842-1847.

(31) Wightman, R. M. *Analytical Chemistry* **1981**, *53*, 1125-&.

(32) Bard A. J., F. L. R. *Electrochemical methods : fundamentals and applications*; Wiley: New York, 2001.

(33) Rossier, J. S.; Girault, H. H. *Lab on a Chip* **2001**, *1*, 153-157.

(34) Horbett T. A., e., Brash J. L., ed. *Proteins at interfaces II : fundamentals and applications*; American Chemical Society: Washington, DC, 1995.

(35) Leininger, R. I.; Peters, A.; Hawks, W. A.; Mirkovitch, V. *Transactions American Society for Artificial Internal Organs* **1964**, *10*, 320-&.

(36) Gott, V. L. *Science* **1963**, *142*, 1297-&.

(37) Gott, V. L.; Whiffen, J. D.; Dutton, R. C. *Science* **1963**, *142*, 1297-&.

(38) Butler, J. E.; Ni, L.; Nessler, R.; Joshi, K. S.; Suter, M.; Rosenberg, B.; Chang, J.; Brown, W. R.; Cantarero, L. A. *Journal of Immunological Methods* **1992**, *150*, 77-90.

(39) Linder, V.; Verpoorte, E.; Thormann, W.; de Rooij, N. F.; Sigrist, M. *Analytical Chemistry* **2001**, *73*, 4181-4189.

(40) Yakovleva, J.; Davidsson, R.; Lobanova, A.; Bengtsson, M.; Eremin, S.; Laurell, T.; Emneus, J. *Analytical Chemistry* **2002**, *74*, 2994-3004.

(41) Farrell, S.; Ronkainen-Matsuno, N. J.; Halsall, H. B.; Heineman, W. R. *Analytical and Bioanalytical Chemistry* **2004**, *379*, 358-367.

(42) Wijayawardhana, C. A.; Wittstock, G.; Halsall, H. B.; Heineman, W. R. *Electroanalysis* **2000**, *12*, 640-644.

(43) Steingroewer, J.; Knaus, H.; Bley, T.; Boschke, E. *Engineering in Life Sciences* **2005**, *5*, 267-272.

(44) Palecek, E.; Kizek, R.; Havran, L.; Billova, S.; Fojta, M. *Analytica Chimica Acta* **2002**, *469*, 73-83.

(45) Fan, A. P.; Lau, C. W.; Lu, J. Z. *Analytical Chemistry* **2005**, *77*, 3238-3242.

(46) DeCory, T. R.; Durst, R. A.; Zimmerman, S. J.; Garringer, L. A.; Paluca, G.; DeCory, H. H.; Montagna, R. A. *Applied and Environmental Microbiology* **2005**, *71*, 1856-1864.

(47) Perelson, A. S.; Bell, G. I. *Nature* **1977**, *265*, 304-310.

(48) Merrill, S. J. *Journal of Immunological Methods* **1998**, *216*, 69-92.

(49) Eisen, H. N. *Abstracts of Papers of the American Chemical Society* **1986**, *191*, B1-ACSC.

(50) Hoylaerts, M. F.; Bollen, A.; Debroe, M. E. *Journal of Immunological Methods* **1990**, *126*, 253-261.

(51) Cumme, G. A.; Bublitz, R.; Ehle, H.; Horn, A. *Journal of Immunological Methods* **1990**, *128*, 241-248.

(52) Knox, J. H. *Journal of Chromatography A* **1999**, *831*, 3-15.

(53) Defrutos, M.; Paliwal, S. K.; Regnier, F. E. *Analytical Chemistry* **1993**, *65*, 2159-2163.

(54) Wang, Q. G.; Wang, Y. M.; Luo, G.; Yeung, W. S. B. *Journal of Liquid Chromatography & Related Technologies* **2001**, *24*, 1953-1963.

(55) Strong, R. A.; Cho, B. Y.; Fisher, D. H.; Nappier, J.; Krull, I. S. *Biomedical Chromatography* **1996**, *10*, 337-345.

(56) Striegel, A. M. *Journal of Chromatography A* **2001**, *932*, 21-31.

Confocal Microscopy to Observe Proteins Adsorption in Microchannels

2.1 Introduction

"Too little signal compared to the noise: the problem kept frustrating me."

Marvin Minsky

The confocal microscope is one of the principal tools for bioanalysis. Thanks to it we can have impressive 3D images of biological samples such as neurons, muscular tissues, cells. It was invented by Marvin Minsky in 1955 during his postdoc at Harvard, "to understand brains, at least at the microscopic level". Minsky was obsessed by the problem of mapping the brain cells in a three dimensional way.[1]

A critical obstacle was represented by the tissue of the central nervous system being solidly packed with interwoven parts of cells. Consequently, even staining all of them, it was still hard to see anything at all. As Marvin Minsky says: "This is not merely a problem of opacity, because if you put enough light in, some will come out. The serious problem is scattering. Unless you can confine each view to a thin enough plane, nothing comes out but a meaningless blur. Too little signal compared to the noise: the problem kept frustrating me."

Finally, one day, he thought that "the way to avoid all that scattered light was to never allow any unnecessary light to enter in the first place." The core idea of a confocal microscope was thus set, that is, eliminating with a pinhole all the light not initially aimed at the focal point.

A confocal microscope selects the light illuminating the sample with a pinhole, eliminating most of the scattered light. In Appendix 1 an excerpt from Minsky's memoir about the invention of the microscope is reported, describing its structure (one of the clearest

descriptions I have read). The light is then condensed on one point of the sample and the fluorescence is again selected by another pinhole. The simplest scheme for a confocal microscope is reported in Fig. 2.1. If we use the condenser to collect the fluoresced light and a dichroic mirror to discriminate the incoming from the outgoing light as done in Fig. 2.2, we have the configuration of the microscope that is normally adopted today. Then, as the specimen is illuminated one point at a time, it must be scanned. Today this is done by moving the beam with a series of mirrors. The specimen itself, however, can be scanned as well. The point-by-point information is then put together in a final image by numerical devices. Minsky did not patent his invention, nor published it, but he set the bases for one of the most useful scientific tools.

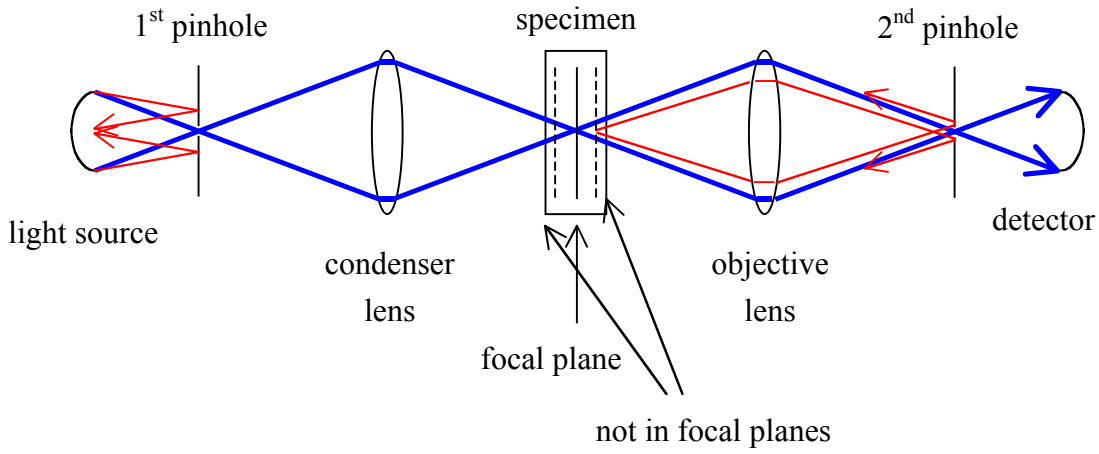

Figure 2.1. Scheme for a confocal microscope. The light is focused into the first pinhole that selects all the beams not conjugated with the focal plane. After having analysed the specimen, the fluoresced light is focused into a second pinhole, which is conjugated with the first and the focal plane. This pinhole rejects again all the light coming from not-in-focal planes. The detector is normally a PMT (photomultiplier tube).

Though confocal microscopy is essentially used in biology,[2] it has also applications in chemistry. Thanks to its restricted field of view, concentrations in the picomolar range of amino acids were detected after separation by capillary zone electrophoresis.[3] Fluorescein

derivatives at 5×10^{-12} M were detected in microtiter plates.[4] Detection in gels and capillary arrays was achieved by Mathies and co-workers.[5, 6] The analysis of matrixes for chromatography, the visualisation of protein adsorbed on different supports, the study of diffusant in polymer films are other possibilities offered by this technique.

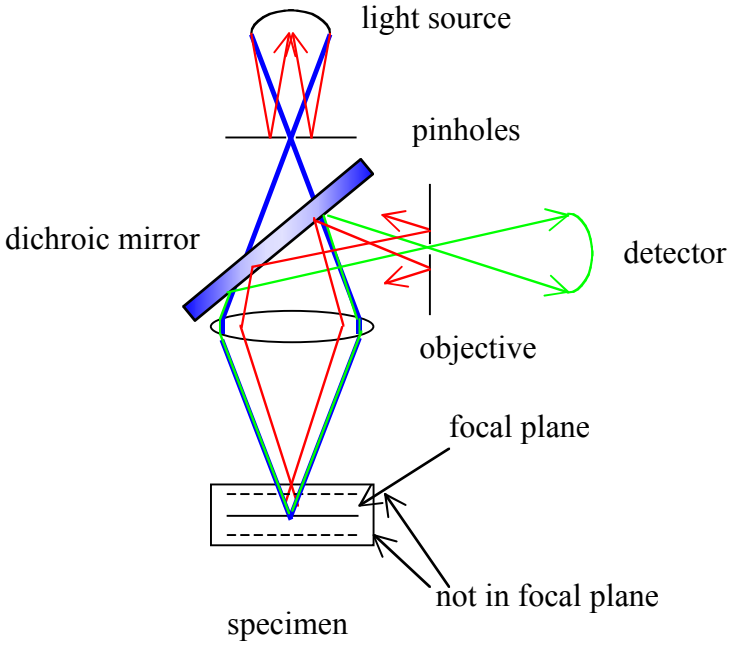

Figure 2.2. Scheme of an epifluorescence confocal microscope (like the one mounted in this work). The light to and from the specimen passes by an objective. A dichroic mirror passes the incident light and reflects the fluorescence.

Over the last few years, our laboratory has investigated the mass transport properties of proteins in microsystem. In particular, microimmunoassays in disposable polymer chips integrating electrodes for electrochemical detection have been developed.[7, 8]

For the present work, there was the need to study the behaviour of proteins in polymer supports used in microimmunoassays (behaviour that often means adsorption, as I lately understood). Furthermore, fluorescence is the method of excellence for detecting concentration in microdevices. The amounts of protein used in microsystems are often very

small: normal concentrations are in the nanomolar range, so that a sensitive technique must be used. When the pinhole used is small, confocal microscopy allows to enhance the signal-to-background and signal-to-noise ratios (thanks to rejection of light coming from the planes out of focus with the analysed sample plane), improving the limit of detection.

A previous PhD student of the lab (François Bianchi) had began to put in place a confocal microscope:[9] it was easy to realise its potential usefulness in the field I wanted my dissertation to develop. It was not rigorously a confocal microscope, for the pinhole system was not present and the scan of the specimen was not possible. Following the guidelines of Ocvirk,[10] a confocal microscope has been built and optimised so that imaging (not in an immediate way) and, above all, measuring and obtaining profiles of fluorescent molecules on transparent supports can now be carried out with it.

The scope of this work is also to establish a method of investigation. The microscope was used to study the adsorption of IgG antibodies on different surfaces and under different conditions. The method can be improved, but the results that can be obtained are already satisfactory.

The goal here is to give an insight of IgG adsorption in these systems and possibly improve it. The higher adsorption concentration (called Γ_{max}) is obtainable when a compact monolayer of proteins is formed. In order to know the Γ_{max} value for IgG in our systems, we silanised the microchannels and then we activated this coating with glutaraldehyde. This method is proved to give a monolayer on smooth surfaces studied by atomic force microscopy (AFM). The value found in this way matches well the theoretical value calculated with the molecular area of an antibody.

As the adsorption on non-silanised microchannels is always lower than this value, new surface modifications are explored, which can be able both to enhance the surface

concentration of antibodies and to keep their natural activity even after adsorption. The confocal microscope was also tested as a detector for capillary electrophoresis experiments performed in microchannels. Some non-optimised but promising results are reported, witnessing the usefulness of the microscope for these applications.

2.2 Experimental Part

2.2.1 Microchannel fabrication

The technique to fabricate the polymer microchannels has been fully described.[7-9] Briefly, the ethanol and water rinsed polymer films ((poly(ethylene terephthalate), PET, 100 μm thick, Melinex; polystyrene, PS, 125 μm thick, Goodfellow) are exposed to a mask patterned 193 nm beam from an ArF excimer laser. The speed of the displacement of the substrate, the fluence and the repetition rate of the laser define a 50 μm deep cavity. The channels for adsorption studies are 210 μm wide at the top and 170 μm wide at the bottom, 50 μm high and 1.5 cm long. The channels for capillary electrophoresis had the classical double T shape, with three 1 cm long arms and one 5 cm long separation channel. Beside the separation channel, near the detection point, a simple 0.4 cm long "check channel" was made. This was filled with a fluorescent solution in order to find the *z* position of the objective to be used in the capillary electrophoresis experiment, performed just after translating the laser spot from the "check channel" to the separation channel. The segment defining the sample plug volume was 0.4 mm long. To allow apertures in the channel, laser drilling was performed at the channel extremities without moving the substrate. After ablation, the debris are removed by gentle rubbing with a methanol wetted tissue. The channel structure, with microholes at each end, is then sealed with PET/polyethylene (PET/PE) lamination at 130 °C and 2 bar pressure with an industrial lamination apparatus (Morane, U.K.). The photoablated PET presents the

favourable characteristics already described[7] and also the following: a) pronounced transparency to the light used to excite the labelled antibody; b) the debris produced by the laser ablation are easily removable and, however, do not generate important noise. Polystyrene has also been tested but it is slightly less transparent, and the debris are noisier and more difficult to remove. Normally, accommodating glass chips and bulky holders under the objective of the microscope is not a negligible problem; the polymer chips fabricated in that way presented the obvious, nonetheless important advantage of needing a submillimeter working space.

2.2.2 Reagents and Procedure

A 1mg/ml ($6.67 \cdot 10^{-6}$ M) solution of labelled antibody (Fluorolink Cy5 labelled antirabbit IgG, Amersham Pharmacia Biotech) was prepared in deionised water, and by serial dilution of it with 0.01M PBS (SIGMA) at pH 7.4, further solutions were obtained. The washing buffer is a 0.1% Tween-20 (SIGMA) solution in PBS. The adsorption of the fluorolabelled antibody was performed by filling a channel with a drop of 8 μl of a given solution concentration, placed at the inlet and pushed in with a pipette. After a certain incubation time *t*, the channel was emptied by flushing air, and then washed three times with 10 μl of washing buffer. As it has been already pointed out,[7] the volume of washing solution is about 100 times that of the channel, which ensures a very efficient washing step. The quantity of antibody adsorbed in the channel was then measured by the confocal microscope. Each channel was used just once. This procedure has been followed for different concentrations.

To enhance the quantity and favour the adhesion of the antibody onto the channel, the surface was silanised.[11, 12] Open channels were cleaned in a series of solvents (chloroform, isopropyl alcohol, methanol, and then water) and then transferred to a 1.5% v/v solution of (3-amino-propyl)triethoxysilane in toluene for 2 h. During that time the chips were silanised due to the hydrolysis of the silane and condensation with reaction groups on the surface. The silanised

substrates were sonicated in the series of solvents to remove any unbound silane. The amino-functionalised substrates were then activated by incubating the silanised channels in a 10% v/v solution of glutaraldehyde (Grade II, 25% in aqueous solution) in PBS for 1h at room temperature. After the channels were rinsed thoroughly with deionised water to remove any unreacted glutaraldehyde, the antibody solution was let to adsorb as previously described. A scheme of the entire process is presented in Fig. 2.3.

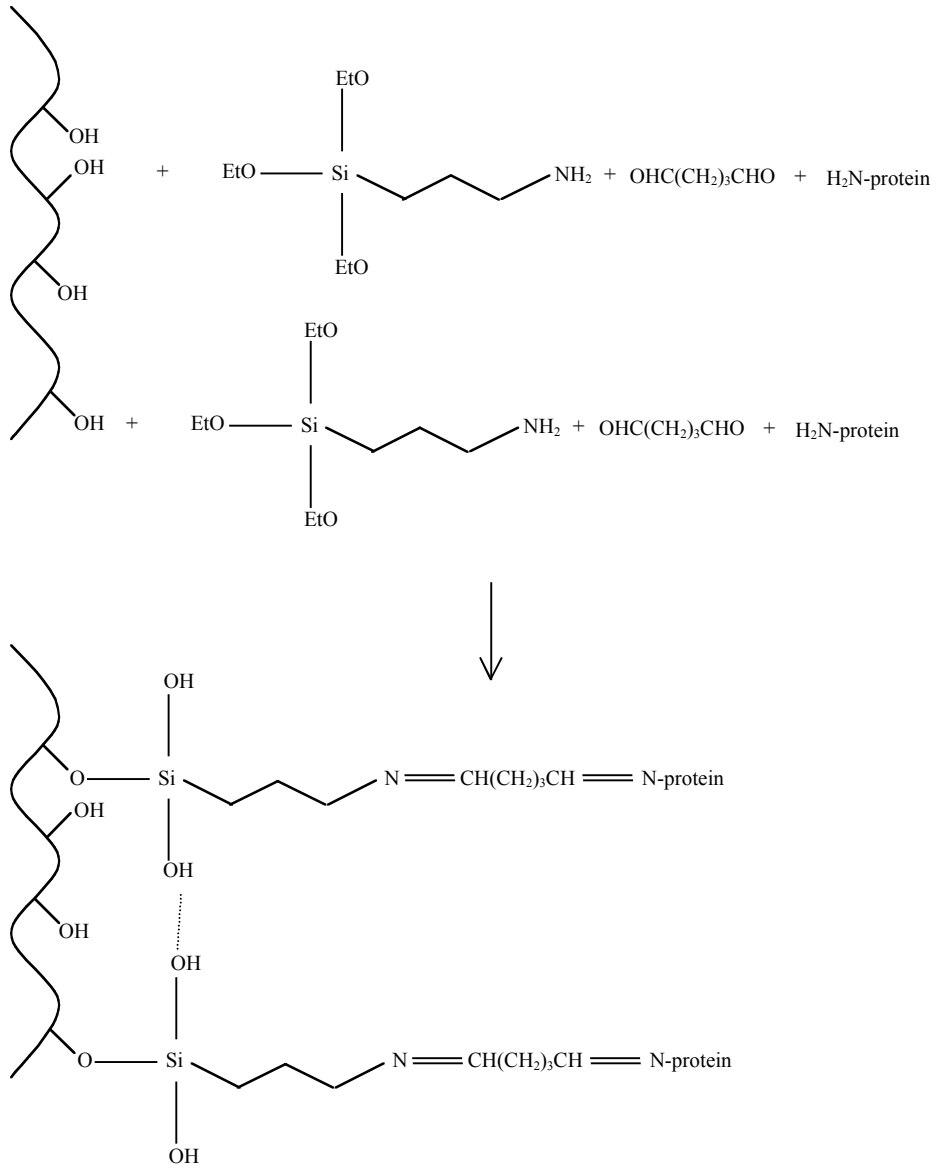

Figure 2.3. Overall scheme of the protein immobilisation method via silanisation and successive activation by glutaraldehyde.

Another method to improve the adsorption activity of the ablated PET is by enhancing the amount of carboxyl groups on PET.[13, 14] First, hydrolysis of the PET ester was performed in a 1:1 mixture of 0.25 M NaOH (Fluka) and acetonitrile (Fluka) at 65°C overnight to expose COOH groups. Then, the channels were washed with water and then oxidised with 0.32 M $KMnO_4$ (Fluka) in 0.6 M H_2SO_4 for 1.5 hours at 70°C. Two washing steps with 6 M HCl and two others with water follow to remove the brown manganese oxide.

Some microchannels were also coated with gold nanoparticles, with an average size of 19 nm, prepared by reducing a tetrachloraurate salt with trisodium citrate.[15] The nanoparticles solution was let to dry in the channels overnight and the unattached nanoparticles were finally removed, rinsing with water.

2.2.3 Microscope Instrumentation

The chips were placed on the *xy* moving plane. This is constituted by a micropositioner stage (Newport, 2 cm range, 10 μm step) for the *Y* direction, and a DC-Motor Controlled translational stage for the *X* direction (M.415 DG, GMP, controlled by a C842.20 DC-Motor Controller, with 16cm range, 0.1 μm step) run by a Windows operating software (C-842 WinMove). The same stage was used for the *z* direction. The stages measure their movement in counts, with a ratio 118.57 counts/μm (company information: manual). For imaging the proteins adsorbed onto the channel surface, it is important to know exactly this ratio. To do that, once the microscope was finally built as described below, 4 channels were drilled 1.5 cm distant one from another the same chip. The channels were filled with a Cy5 solution and the chip was scanned at a velocity V = 20000 counts/sec. The average time to run 15000 μm is 89.28 ± 0.11 sec (as it can be seen in Fig. 2.4) from which a ratio 119.04 counts/μm is obtained, only 0.4% different from the one given by the company. Finally, this last value is used to transform the time scale into a space scale in imaging applications.

Excitation light from a diode laser (630 nm, Melles Griot) was focused on a 200 μm pinhole,

reflected by a steering mirror (02MFG015/003, Melles Griot) then passed through a 575-625 nm bandpass filter, reflected by a dichroic mirror, focused onto the chip to a ≈ 20 μm spot.

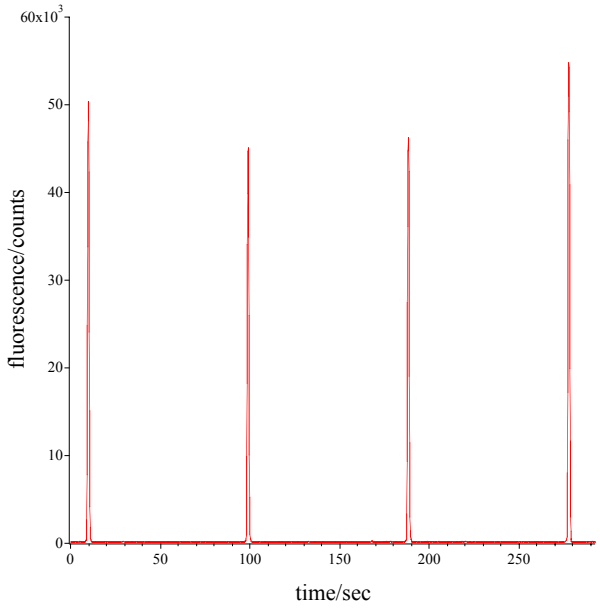

Figure 2.4. To know the ratio counts/μm of the translational stages, 4 channels 1.5 cm distant one from another one, filled with a Cy5 solution, were scanned at a velocity V = 20000 counts/sec. The average time to run 15000 μm was 89.28 ± 0.11 sec from which a ratio 119.04 counts/μm is obtained.

A 0.6 N.A., 40× infinite conjugate, microscope objective (LD Achroplan, Zeiss) was used. The fluorescence emission was collected by the same objective, passed through the dichroic mirror, a 660-710 nm band pass filter, and focused onto an 800 μm pinhole. The band pass filters and the dichroic mirror constitute the filter set n° 26 by Zeiss. A photomultiplier tube (PMT Hamamatsu H6240-01) was mounted on top of the microscope tube with a 670/10 nm interference filter (03FIL054 Melles Griot). Signals from the PMT were recorded with a program written in LabView. The collected separation data were smoothed using a seven-point box smooth algorithm, included in Igor Pro (Wavemetrics, Lake Oswego, OR, USA).

2.2.3.1 Building microscope procedure

The optical pieces were mounted on a 60 × 60 cm Newport optical table (see Fig. 2.5). After being focused on the first pinhole with a 10 cm focal point lens, the laser beam was again adjusted in order to make the diameter equal to the objective diameter. To accomplish this operation, another 10 cm focal point lens was moved by a micropositioner, by steps of 10 μm, until the right diameter was found. At this point, to align the detection set-up, the

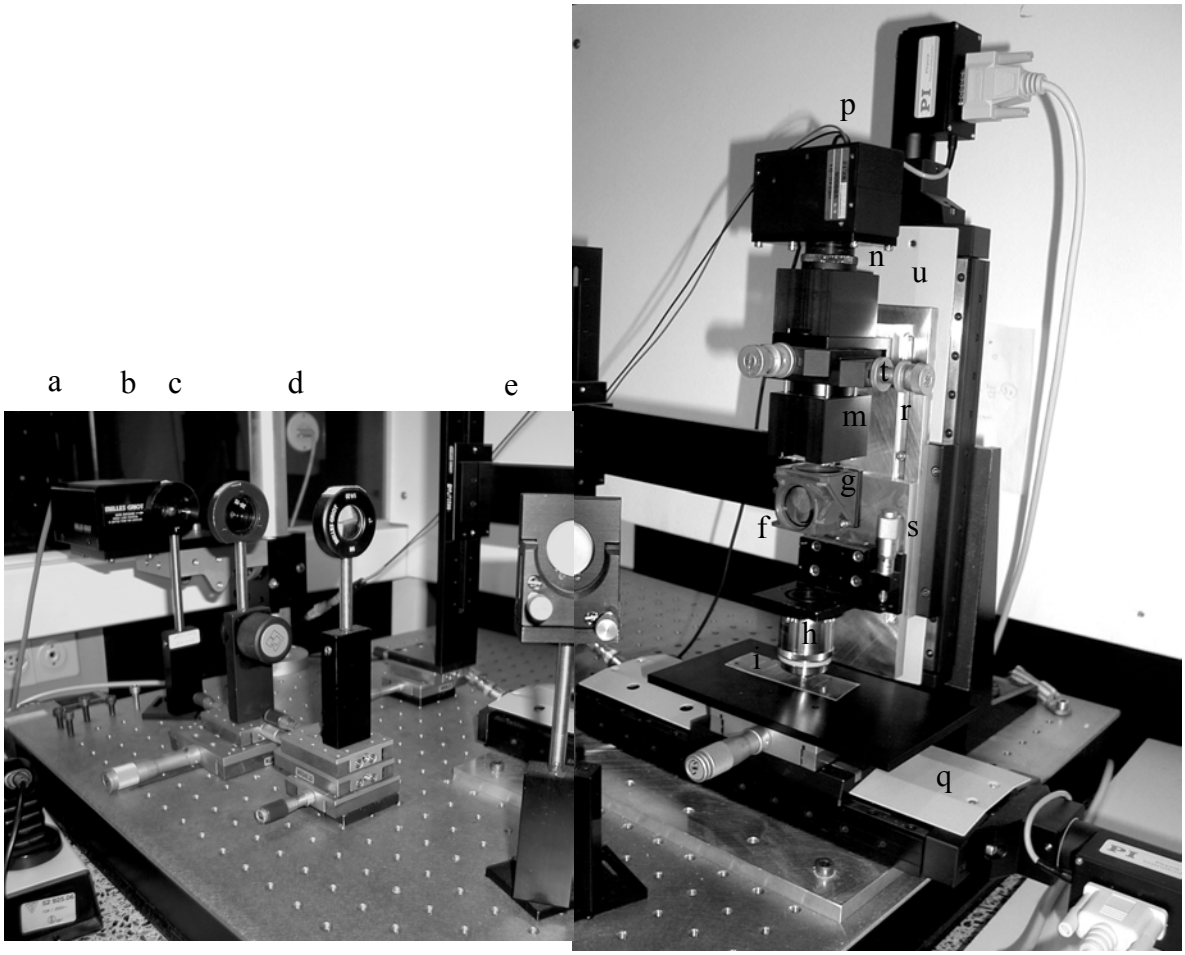

Figure 2.5. Picture of the microscope (2 pictures were edited together to have the whole view of the microscope: the mirror in the centre reflects the light coming from the laser at 45° towards the microscope. The optical path can be followed from the left to the right: the light from the laser (a) is focused by the lens (b) into the first pinhole (c). The second lens (d) focuses the laser beam to the infinite. The mirror (e) is also used to convey the beam to the objective. The light is selected by a first filter (f), then reflected by the dichroic mirror (g) to the objective (h) and reaches the sample, the microchannel (i). The fluorescence passes the objective, and is focused into the second pinhole (m). Then, after being filtered (n), reaches the PMT (p). In the column of the microscope to the right they can be noticed, from the bottom: the horizontal translational stage (q); the moving support on which the column is mounted, by which it is possible to place the dichroic mirror at the right height with respect to the beam (r); a fine adjust (s) for the position of the objective relatively to the second pinhole; the positioner for the pinhole (t); the vertical translational stage (u).

microscope objective was removed and the chip was replaced with a mirror. The reflected beam was superimposed on the incoming beam by adjustment of the beam steering mirror. The objective was then mounted, the beam was focused on the second pinhole by displacing

the objective with respect to this. The pinhole was aligned with the beam and then the objective was re-positioned again, in a feedback process, until no change was observed in the signal. The position of the lens was then also re-adjusted: to do that a channel was filled with a 10^{-8} M IgG labelled solution and different shapes of the channel were registered by changing the lens position at each measurement. The final position was chosen when the measured shape of the channel was sharper and more similar to the trapezoidal shape of the experimental channel, as shown in Fig. 2.6. Data were obtained by moving the *y* translational stage at a velocity of 42.17 μm/sec, which was fast enough not to produce photobleaching and slow enough to obtain an accurate measure, respecting the sampling time of the LabView program.

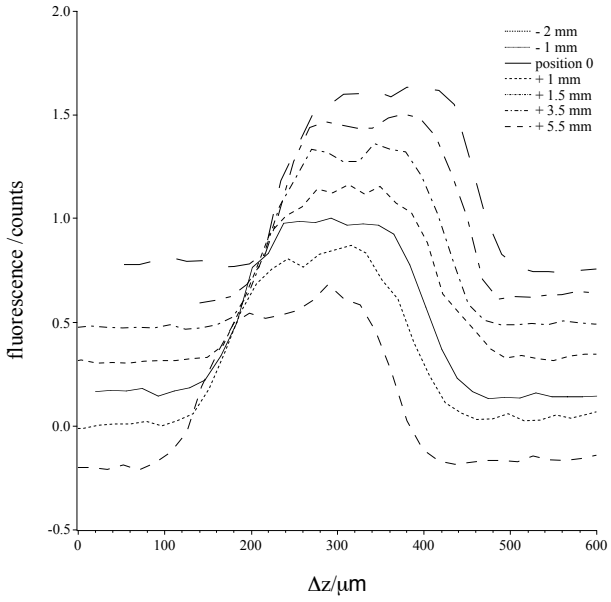

Figure 2.6. Images of a channel stained with Cy5. The different scans were made with different positions of the lens (b) in Fig. 2.5 to find the position of the lens at which the image was more precise (called position 0 and corresponding to the full line scan).

The spot diameter was measured. A channel was filled with 10^{-8} M IgG labelled solution, and the *z* position at which the signal was maximum was found, i.e. at which the pinhole was in a conjugate focal plane with the sample. Then, a filter paper was wetted with a drop of the Cy5

solution and the circle stain obtained was half covered with black tape. The zone between the paper and the tape was scanned at a velocity of 8.43 μm/sec. The passage from dark (10% of the signal corresponding to the background) to fluorescence (90% of the signal found in the centre of the stain) is done in about 27 μm, as shown in Fig. 2.7, i.e. the spot diameter.

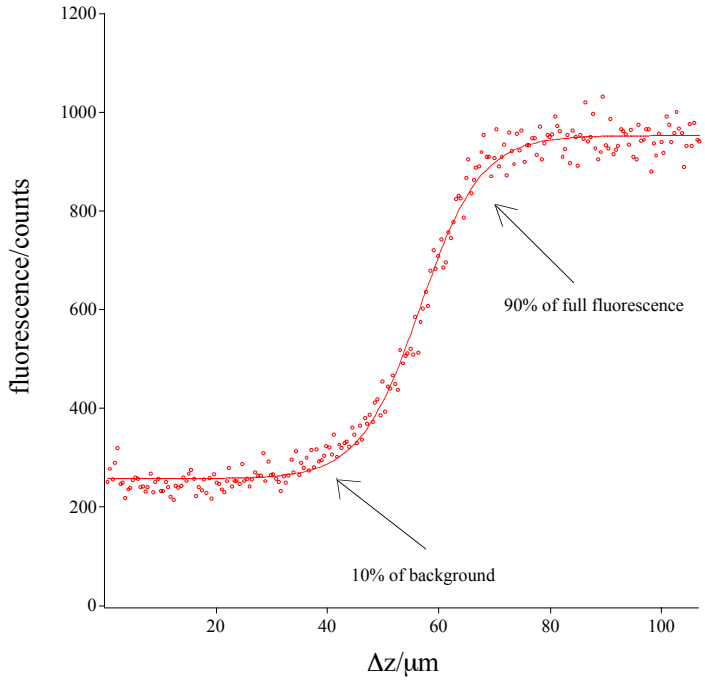

Figure 2.7. Scan through a dark/fluorescent edge to know the diameter of the beam onto the specimen.

2.2.4 Capillary electrophoresis

The high-voltage control system for the chips has been described previously.[16] High-voltage (HV) supplies used in the system were from Spellman (CZE 1000 R). After optimisation of the procedure for this geometry, the values chosen for the injection and the separation were ΔV = 300 V for 30 sec and 3000 V for 150 sec respectively. The detection point was fixed 1 cm upstream from the separation channel outlet. Pt electrodes were put in the polyethylene PE reservoirs (as previously described).[16] The injection-separation switch was achieved through a homemade switch box commanded by a LabView program. The velocity flow of our system is 0.67 mm·sec^{-1} by measuring the time for the dye front to travel from the

injector to the detector. This velocity value has been optimised in order to avoid bleaching in the Cy5 dye. Faster velocities caused also an excessive broadening of the peaks. Ocvirk, whom guidelines for the construction of the confocal microscope I followed,[10, 17] used higher values for the separation voltage, resulting in velocities of 3.5 mm·sec^{-1}: the dye he used was fluorescein, which photobleaches much faster than Cy5.

2.3 Results and discussion

2.3.1 Optical characteristics of the confocal microscope

The aim of building this microscope is to obtain a precise device able to give a strong signal in comparison to the background. The precision of a confocal microscope is measured by the strength of the optical sectioning. This quantity is the rate at which the fluorescence intensity decreases with the vertical distance between objective and object, and is known as the axial response of a confocal microscope. Analogous to Wilson[18] and Ocvirk, [10] a measure of the sectioning power is defined by the vertical displacement given by full-width-at-half maximum (FWHM) of the axial response. To evaluate our design, a channel filled with an IgG solution $1.1 \cdot 10^{-7}$ M was scanned vertically (velocity was 168.7 μm/sec). In Fig. 2.8 the corrected fluorescence signals were ratioed by the noise. The background was estimated scanning horizontally a chip full of PBS. For the 400, 800 and 1000 μm sized pinholes, the FWHM displacements were 47.5, 71.5 and 71.4 μm, respectively. The 800 μm pinhole was clearly the optimal choice. Fig. 2.8 shows that increasing the pinhole diameter from 400 to 800 μm results in an improvement of the (S-B)/N (where S is the signal, B the signal of the background and N the noise) by a factor of more than 4. This improvement is consistent with the increased probe volume occurring (with a larger pinhole a greater amount of light is collected). A further increase of the pinhole to 1000 μm does not lead to an increase of the (S-B)/N. This is due to the fact that the depth of field exceeds the channel depth and that the

observed spot size is larger than the excitation diameter, so that significant background is collected causing a decreased S/N. Finally, the 800 μm pinhole was used for the experiments.

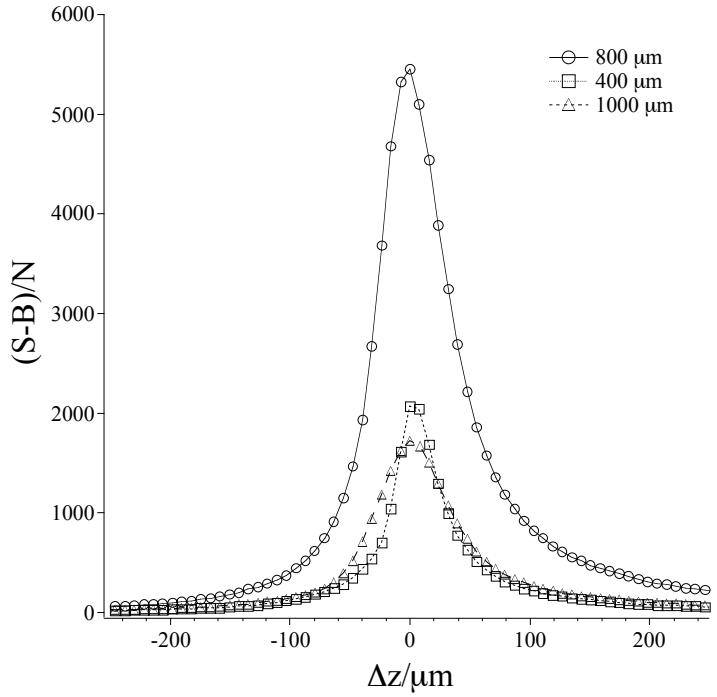

Figure 2.8. Signal-to-noise ratio (signal corrected for background fluorescence, (S-B)/N) *versus* vertical displacement of chip (Δ*z*) for various pinhole diameters, 800, 400, 1000 μm from top to bottom, respectively.

A smaller pinhole would allow for a more precise axial resolution (however lowering the signal to noise ratio). Another way to increase the resolution is by underfilling the diameter of the laser beam entering the objective. This can be done displacing the lens (lens b in Fig. 2.5) before the optimal position.

2.3.2 Measurement of protein adsorption on microchips

To know the amount of the adsorbed proteins, a calibration curve was made. The fluorescence from channels filled with different concentrated solutions of IgG antibodies was collected; the plot is reported in Fig. 2.9 (dashed line). A weighted linear fit of all data points gives a slope of 0.87 and a linear correlation coefficient of 0.998. The standard deviation was calculated over 5 different measurements. The signal corresponding to $C°$ = 3 nM is well over the signal corresponding to 3 times the background. To obtain the surface concentration

of the adsorbed protein, the molar concentration extrapolated from the calibration curve was multiplied by the volume-to-surface ratio of the microchannel.

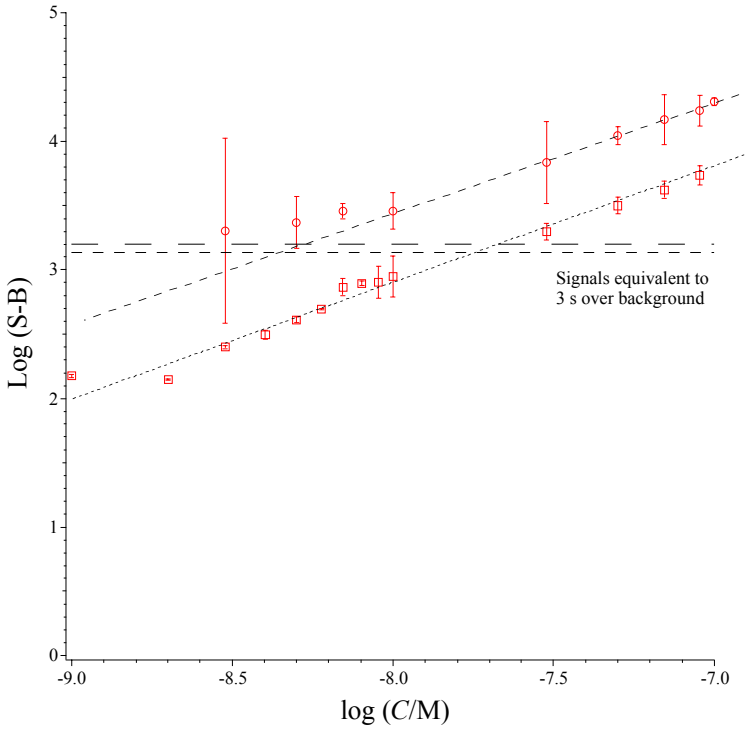

Figure 2.9. Log–log plot of fluorescence intensity, S, from IgG solutions, corrected for background fluorescence, B, as a function of IgG concentration. Error bars are calculated from 5 measurements as indicated under Experimental. A line 3*s* above the background signal (estimated from the *s* value for 3 nM) is shown to illustrate the signal detection limit floor. The dashed lines represent the 3*s* signal and the calibration line obtained with a 800 μm pinhole (open circles); the dotted lines are obtained from experiments with a 400 μm pinhole (open squares).

In the same figure, the calibration curve obtained with the 400 μm pinhole is also reported (dotted lines). A weighted linear fit of all data points gives a slope of 0.90 and a linear correlation coefficient of 0.992. It can be noticed that, due to the low signal/noise ratio, the limit of detection is about one order of magnitude higher than with the 800 μm pinhole. A similar plot for polystyrene chips gives a slope of 0.72 and a linear correlation coefficient of 0.996.

After the adsorption and the rinsing steps, the amount of proteins on the walls was read from the horizontal scans of the microchannels after a certain time *t* of adsorption. The time *t* varied from 10 sec to hours when recording the kinetics of adsorption and was generally set to 30 min for static isotherms. Typical scans over 30 minutes of IgG adsorption on PET is represented in Fig. 2.10. From the values taken at the centre of the channel, a kinetic isotherm can be registered. The peaks at the two sides of the channel are due to the collection of the fluorescence from the proteins adsorbed onto the lateral walls. An extensive discussion of the proteins adsorption on the microchannel surface is given in the following chapters.

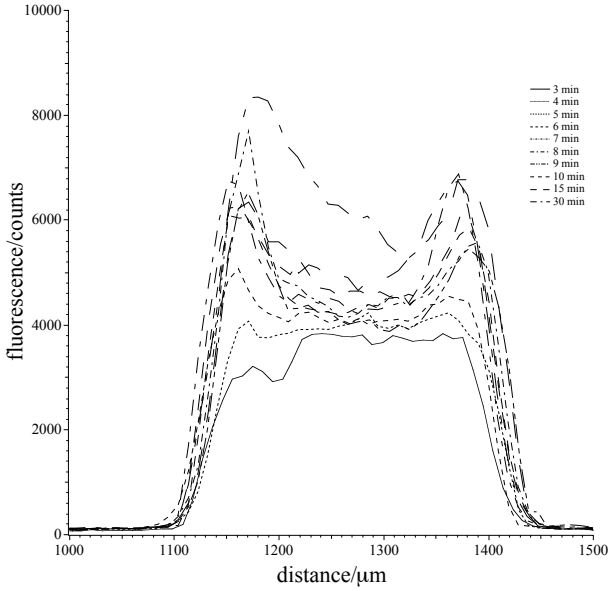

Figure 2.10. Scans of the microchannels in which adsorption occurred from 6.67×10^{-7} M IgG solution. The scans are made at different times, and a kinetic of adsorption can be obtained from the value of fluorescence taken at the middle of the channel.

2.3.3 Surface modifications

To enhance the adsorption in the microchannel and improve the performance of an eventual microimmunoassay, some surface modifications were tested. The channel was silanised and oxidised by permanganate. Gold nanoparticles were also adsorbed onto the surface.

The silanisation is a technique widely used to obtain protein monolayer on different surfaces.[11] It is used when antibodies must be strongly attached to a surface, for instance when antibody-antigen interactions are studied by atomic force microscopy. In this case, an antibody covered surface is scanned with the microscope cantilever that is antigen-functionalised. As the antibody-surface binding must be stronger than the antibody-antigen one, this immobilisation technique is successfully used. In fact the protein is linked by covalent bonds to the aldehyde substrate through its external amino groups. It is worth to give emphasis to the fact that the amino groups engaged in the covalent bonds are not the terminal ones, which, in IgG molecules, are in the antigen-binding fragment of the molecule (see Fig. 1.3). When adsorbing, in fact, antibodies preferably orient with the heavy chain constant region (the Fc fragment) towards the surface.[19] The amino groups of the lateral chains of the amino acids of this part of the molecule are used to bind to the aldehyde. The treatment with glutaraldehyde does not denaturate the antibodies, and they can be thus used for immunological studies.

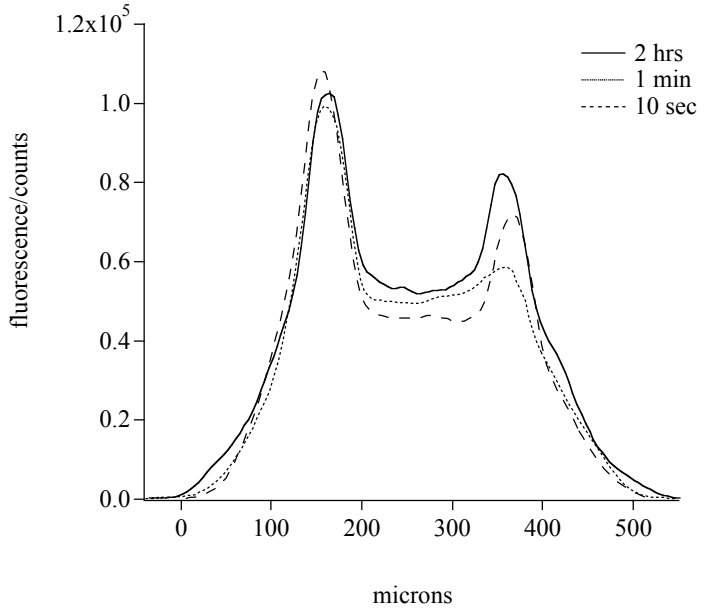

Figure 2.11. Scans as in Fig. 2.10 in a silanised microchannel.

In Fig. 2.11 we report the kinetic of adsorption of IgG onto a silanised surface. As the adsorption does not change too intensely from 10 sec to 2 hours, and since at 10 sec the signal is already very strong, a fast kinetic of adsorption can be deduced. The signal at equilibrium (2 hours) is more or less 10-fold the one obtained on non-modified PET (the adsorption on a silanised microchannel is the maximum that can be obtained assuming an IgG monolayer). We will see that the IgG adsorption on PET occurs leaving 9/10 of the surface free.

After the permanganate treatment the surface should be richer in carboxy-groups resulting from the oxidation of hydroxyl, aldehyde or ketone groups. This change could lead to an enhanced protein adsorption. However, the noise after the treatment (maybe due to manganese oxide that remains onto the oxidised surface even after thorough rinsing) is too strong for this procedure to be useful.

The gold nanoparticles used to coat the channel surface produce non-negligible scattering and, therefore, they were not used in adsorption experiments.

In the following chapters we will relate some fruitful surface modification made with TiO_2 materials on PET microchannels that were oxidised with NaOH.

Polystyrene is slightly less transparent, resulting in a higher limit of detection compared to PET; the debris are noisier and more difficult to remove so that reading the values of adsorbed proteins was more difficult. A scan of IgG adsorbed onto PS is shown in Fig. 2.12: the two peaks besides the channel are due to scattered light by the debris redeposited on the

two sides of the channel during the ablation. For these reasons PET was chosen as substrate for the experiments in the following chapters.

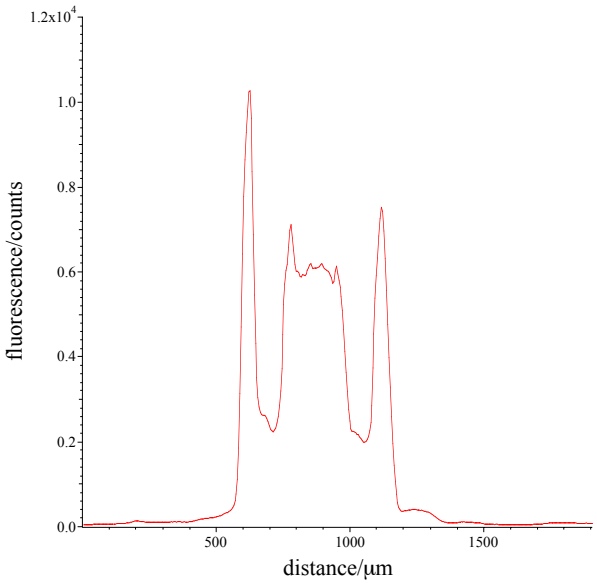

Figure 2.12. Scan as in Fig. 2.10 after a 30 min adsorption in a PS microchannel.

2.3.4 The confocal microscope as a detector for capillary electrophoresis

The experiments for capillary electrophoresis in microchannels with confocal microscope laser induced fluorescence detection were carried out to test a potential use of the microscope in this field. Even though the results could be optimised, the usefulness of the device in this field is assessed.

The electropherogram of a mixture of cytochrome C (10^{-8} M) and IgG (6.67×10^{-8} M) antibody both labelled with Cy5 is shown in Fig. 2.13. The two proteins were run separately in order to find out their retention time, which corresponds to 61 sec for the cytochrome C and 81 sec for the IgG. Some products come after the IgG peak, probably some aggregates. The number of theoretical plates (calculated from $N = 5.55\ (t_R/w_R)^2$, where t_R is the retention time and w_R the full width at half maximum of the peak) for cytochrome C is 2158 and for IgG is 1859, which is an average value for CE in microchannels.[20]

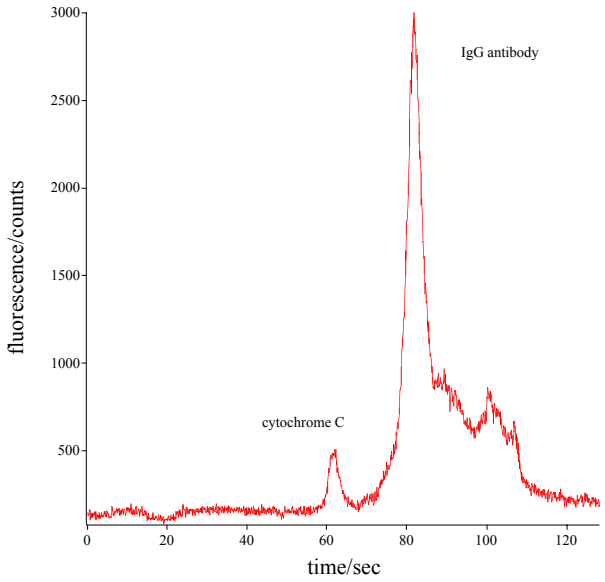

Figure 2.13. Electropherogram of a mixture of cytochrome C (10^{-8} M) and IgG (6.67×10^{-8} M). ΔV for the injection was 300 V for 30 sec; ΔV for the separation was 3000 V for 150 sec.

The greatest disadvantage of this set up is the need of labelling the analytes. The possibility of performing an inverse detection was tested, filling the channel with Cy5 dye and injecting a non-labelled analyte. In Fig. 2.14 the electropherogram of the injection of non-labelled imidazole (34 nM) is shown.

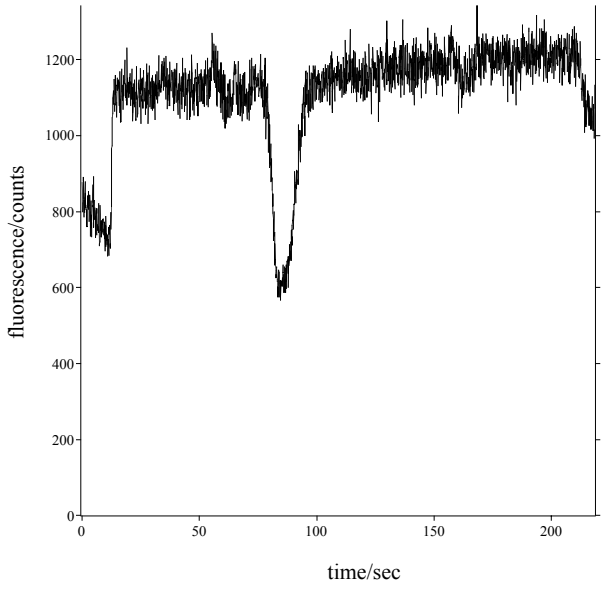

Figure 2.14. Electropherogram of the injection of a 34.5 nM solution of non-labelled imidazole. The buffer was a solution of Cy5 dye in PBS.

Several runs were made with high reproducibility, for concentrations spanning through 8 orders of magnitude (34.5 mM, 0.345 mM, 3.4 μM and 34 nM). Though the 34.5 nM injection was well defined, a great problem was defining a good ratio between the concentrations of mobile phase dye and of the analytes. More concentrated solutions in low concentrated dye buffer gave peaks very broad and "out of scale", meaning that the dye signal was not high enough to let the peak develop in its depth (it always touched the background signal); on the other hand, increasing the concentration of dye led to the disappearing of the peak. A quantitative analysis made in this way is impossible.

2.4 Conclusions

A confocal microscope was built in order to analyse protein adsorption in polymer microchannels. It has a spatial resolution of about 20 μm and a depth resolution comparable to the depth of the microchannels. With these characteristics we have an instrument that has a good signal-to-noise and signal-to-background ratios, useful to detect the small amounts of proteins normally used in microchannels. The limit of detection of the instrument is 3 nM, when used with PET microchannels. The microscope can also image proteins adsorbed onto the walls of the microchannels, but it will mainly be used as a tool to quantitate the adsorption, as it will be illustrated in the next chapters.

As one of the aims of this dissertation will be improving immunoassays in microsystems, the polymeric surface was modified in different ways. This will lead to enhance the surface concentration of the capture antibody, which in turn will result in a higher signal from the labelled antigens.

The most effective modification is by silanisation followed by activation with glutaraldehyde (normally used to treat the samples in view of atomic force microscopy). In this way the antibodies are covalently linked to the surface and form a monolayer: this is the highest

surface concentration obtainable (which is 10-fold higher than when non-modified PET is used). The microscope was also proved useful as a detector in capillary electrophoresis experiments carried out in PET microchannels.

Excerpt from Marvin Minsky, “Memoir on Inventing the Confocal Scanning Microscope,” Published in Scanning, vol.10 pp128-138, 1988.

An ideal microscope would examine each point of the specimen and measure the amount of light scattered or absorbed by that point. But if we try to make many such measurements at the same time then every focal image point will be clouded by aberrant rays of scattered light deflected points of the specimen that are not the point you’re looking at. Most of those extra rays would be gone if we could illuminate only one specimen point at a time. There is no way to eliminate every possible such ray, because of multiple scattering, but it is easy to remove all rays not initially aimed at the focal point; just use a second microscope (instead of a condenser lens) to image a pinhole aperture on a single point of the specimen. This reduces the amount of light in the specimen by orders of magnitude without reducing the focal brightness at all. Still, some of the initially focused light will be scattered by out- of-focus specimen points onto other points in the image plane. But we can reject those rays, as well, by placing a second pinhole aperture in the image plane that lies beyond the exit side of the objective lens. We end up with an elegant, symmetrical geometry: a pinhole and an objective lens on each side of the specimen. (We could also employ a reflected light scheme by placing a single lens and pinhole on only one side of the specimen - and using a half-silvered mirror to separate the entering and exiting rays). This brings an extra premium because the diffraction patterns of both pinhole apertures are multiplied coherently: the central peak is sharpened and the resolution is increased. (One can think of the lenses on both sides of the microscope combining, in effect, to form a single, larger lens, thus increasing the difference in light path lengths for point-pairs in the object plane.)

The price of single-point illumination is being able to measure only one point at a time. This is why a confocal microscope must scan the specimen, point by point and that can take a long time because we must add all the time intervals it takes to collect enough light to measure each image point.

The most serious design problem was choosing between moving the specimen or moving the beam. So far as I know, all modern confocal microscopes use moving mirrors or scanning disks. At first it seemed more elegant to deflect a weightless beam of light than to move a massive specimen. But daunted by the problem of maintaining the three-dimensional alignment of two tiny moving apertures, I decided that it would be easier to keep the optics fixed and move the stage.

References:

(1) Minsky, M. *Scanning* **1988**, *10*, 128-138.

(2) Masters B. R., e. T. B. J. *Selected papers on confocal microscopy*, 1996.

(3) Cheng, Y. F.; Dovichi, N. J. *Science* **1988**, *242*, 562-564.

(4) Mathies, R. A.; Scherer, J. R.; Quesada, M. A.; Rye, H. S.; Glazer, A. N. *Review of Scientific Instruments* **1994**, *65*, 807-812.

(5) Woolley, A. T.; Mathies, R. A. *Analytical Chemistry* **1995**, *67*, 3676-3680.

(6) Huang, X. H. C.; Quesada, M. A.; Mathies, R. A. *Analytical Chemistry* **1992**, *64*, 2149-2154.

(7) Rossier, J. S.; Gokulrangan, G.; Girault, H. H.; Svojanovsky, S.; Wilson, G. S. *Langmuir* **2000**, *16*, 8489-8494.

(8) Rossier, J. S.; Girault, H. H. *Lab on a Chip* **2001**, *1*, 153-157.

(9) Bianchi, F. PhD Thesis, Lausanne, 2001.

(10) Ocvirk, G.; Tang, T.; Harrison, D. J. *Analyst* **1998**, *123*, 1429-1434.

(11) Allen, S.; Chen, X. Y.; Davies, J.; Davies, M. C.; Dawkes, A. C.; Edwards, J. C.; Roberts, C. J.; Sefton, J.; Tendler, S. J. B.; Williams, P. M. *Biochemistry* **1997**, *36*, 7457-7463.

(12) Vinckier, A.; Heyvaert, I.; Dhoore, A.; McKittrick, T.; Vanhaesendonck, C.; Engelborghs, Y.; Hellemans, L. *Ultramicroscopy* **1995**, *57*, 337-343.

(13) Ros, A., 2000.

(14) Palit, S. R.; Ghosh, P. *Journal of Polymer Science* **1962**, *58*, 1225-&.

(15) Turkevich, J.; Stevenson, P. C.; Hillier, J. *Discussions of the Faraday Society* **1951**, 55-&.

(16) Bai, X. X.; Roussel, C.; Jensen, H.; Girault, H. H. *Electrophoresis* **2004**, *25*, 931-935.

(17) Jiang, G. F.; Attiya, S.; Ocvirk, G.; Lee, W. E.; Harrison, D. J. *Biosensors & Bioelectronics* **2000**, *14*, 861-869.

(18) Wilson, T. *Journal of Microscopy-Oxford* **1989**, *154*, 143-156.

(19) Vikholm, I.; Teleman, O. *Journal of Colloid and Interface Science* **1994**, *168*, 125-129.

(20) Chiem, N.; Harrison, D. J. *Analytical Chemistry* **1997**, *69*, 373-378.

Protein Adsorption in Static Microsystems: Effect of the Surface to Volume Ratio

(based on Lionello, A.; Josserand, J.; Jensen, H.; Girault, H. H. *Lab on a Chip* **2005**, *3*, 254-260)

3.1 Introduction

Immunoassays, tests that identify a substance (for instance a protein) by its capacity to act as an antigen, are standard tools for the diagnosis of different physiological conditions, from pregnancy to diseases like AIDS or hepatitis. Sometimes these tests are supplied in easy-to-use formats and can provide a response in a few minutes at best. In fact, in the microtiter well of a standard ELISA, one of the most used immunoassay format, the distances that molecules need to diffuse in order to interact (to adsorb, in the case of the primary antibody) with the solid support are in the order of millimeters. As already illustrated,[2] a large protein like an immunoglobulin G (IgG antibody, 150 kDa) diffuses 1 mm in more than 3 hours; diffusion time thus often limits the speed of the analysis. To improve the throughput of immunoassays, the implementation of microfluidics in immunoassays has been proposed.[3] Compared to the classical ones, a microimmunoassay presents the following advantages: limited reagent consumption and faster analysis time due to a larger surface-to-volume ratio and the improved mass transport efficiency.

Adsorption of macromolecules has proved to be a challenging subject both theoretically and experimentally. Adsorption and transport processes under the Langmuir isotherm assumptions have been modelled mathematically[4] to better understand the phenomena involved in capillary electrochromatography.[5, 6] Several models exist for protein mass transfer,[7] for their adsorption on ion exchange particles[8-11] and on sorbent matrices.[12, 13] Mathematical models have also been used to describe the adsorption kinetics of proteins[14]

and polyelectrolytes[15] on planar surfaces. Computer methods have been employed for decades to study adsorption processes in electrochemical systems characterised by semi-infinite linear diffusion[1,16] in order to get a better understanding of the phenomena involved. A simulation of protein adsorption in cylindrical geometry from a non-flowing, dilute solution has also been reported.[17] The studies dealing with transport and adsorption of proteins on a substrate define different regimes, depending on the adsorbate-sorbent couple. A diffusional limitation of the processes is observed when the adsorption kinetics is much faster than the diffusion:[18] each protein molecule that reaches the surface is immediately adsorbed and the concentration of analyte near the wall tends to zero. On the other hand, when adsorption is much slower than diffusion controlled mass transport, kinetics plays an important role.[19-21]

In this work, a numerical model using the finite element method has been developed to study adsorption in polymer microchannels (in order to describe an allergy test based on an immunoassay). It takes into account the diffusion of one species in the channel, coupled with the adsorption kinetics at the sorbent wall, following the Langmuir isotherm assumptions. It allows the investigation of the mutual influence of the adsorption rates, the bulk and the surface concentrations and the solute diffusion coefficient. It provides the time evolution of the concentration in solution and at the surface, revealing how the former can affect the latter in a microsystem. A new non-dimensional parameter characteristic of any microchannel was defined, by which it is possible to calculate the final value of the coverage in that microsystem.

The study of adsorption of macromolecules has been reported using a variety of measurement techniques, with different protocols and calibrations.[18,22-25] Adsorption kinetics of immunoglobulins in a photoablated polymer microchannel, similar to the ones used in this work, was studied using radiometric detection[18] and by electrochemical detection.[24] The

experimental results presented here are obtained by laser-induced-fluorescence confocal microscopy. A confocal microscope was set up as explained in chapter 2 and optimised following Ocvirk et al.[26] to investigate the adsorption of a fluorescently labelled IgG on PET microchannels. This technique has already been used to study concentration profiles of a "diffusant" in polymer films,[27] adsorption of proteins to chromatographic matrices[28] and to porous adsorbents.[29, 30] The detection is made by optical sectioning of the sample. The sample preparation is therefore easier and quicker than for methods requiring mechanical sectioning. It is also a very sensitive method, the high signal-to-background ratio of the set up allowing the detection of very low concentrations.

The finite element simulations are fitted to the experimental results, in order to determine the rates of adsorption. It is questionable[17] whether the adsorption of molecules as heterogeneous as proteins can be described adequately with a few parameters and a general model form. However, if a model can be in accordance with the experimental data in some given conditions, the fitted parameters help to understand the influence of these conditions in order to further optimise them.

3.2 Theory

3.2.1 Adsorption

The present model is intended for a general case in which a molecule A is adsorbed on a sorbent surface where the active sites B are present. It is based on the Langmuir isotherm model, which uses the active sites concept in the adsorption expression in order to address the reduction of its rate with the coverage of the wall. The model has found wide applications for the adsorption of proteins on substrates or ligands immobilised on a support material.[8, 9, 12] The Langmuir isotherm model represents a simplified case of protein adsorption, since it assumes (a) reversible adsorption, (b) constant properties of the molecules (proteins) even

after the adsorption, (c) no lateral interactions between adsorbed molecules, (d) each active sites B adsorbing only one molecule A and (e) all the adsorption sites having the same affinity for the adsorbate molecules. Although these assumptions are not strictly valid in theory for macromolecular adsorption, the Langmuir model has proven to be useful in practice.[31]

Under such assumptions we can represent the adsorption equation by:

$$A + B \underset{k_{on}}{\overset{k_{off}}{\rightleftharpoons}} AB \qquad (3\text{-}1)$$

where A is the solute molecule in solution (of bulk concentration C), B is the site active for adsorption on the surface, AB is the adsorbate immobilised (of concentration Γ) onto the active site. The initial surface concentration of the active sites is Γ_{max} (*i.e.* the maximum attainable surface concentration of immobilised adsorbate) and the surface concentration at time t is $\Gamma_{max} - \Gamma(t)$. The constants k_{on} and k_{off} represent the rates of adsorption and desorption of the adsorbate onto the active sites. As a consequence, the kinetics of the process is described by:

$$\frac{d\Gamma(t)}{dt} = k_{on}C(t)(\Gamma_{max} - \Gamma(t)) - k_{off}\Gamma(t) \qquad (3\text{-}2)$$

The ratio of the constants k_{on} / k_{off} determines the equilibrium constant K (eq. (3-3)). Since a monolayer is supposed to be formed, the quantity $\Gamma_{max} - \Gamma(t)$ decreases while $\Gamma(t)$ increases until the equilibrium is reached. At equilibrium $d\Gamma(t)/dt = 0$ in eq. (3-2) and $C_{eq} = C°$ (*i.e.* the initial concentration of A, in cases where the bulk depletion is negligible), leading to eq. (3-3). This assumption is consistent with semi-infinite linear diffusion,[1, 16] and its validity in the case of a microsystem will be discussed later.

$$K = \frac{k_{on}}{k_{off}} = \frac{\Gamma_{eq}}{C°(\Gamma_{max} - \Gamma_{eq})} \qquad (3\text{-}3)$$

Eq. (3-3) can be written as follows:[1]

$$\frac{\Gamma_{eq}}{\Gamma_{max}} = \frac{KC^{\circ}}{1+KC^{\circ}} = \frac{\psi}{1+\psi} \qquad (3\text{-}4)$$

where $\psi = K \cdot C^{\circ}$. The parameter ψ can be seen as an indicator of the capacity of the system to reach the maximum coverage of the wall.

3.2.2 Diffusion adsorption for a small coverage (analytical expression)

In the range of small coverage of the adsorbent (i.e. $\Gamma_{eq} << \Gamma_{max}$), Γ_{eq} can be neglected in the denominator of eq. (3-3) and the adsorption isotherm can be linearised as follows:

$$\Gamma_{eq} = KC^{\circ}\Gamma_{max} \qquad (3\text{-}5)$$

Fick's law can then be solved analytically,[15] leading to:

$$\frac{\Gamma}{\Gamma_{eq}} = 1 - exp\left(\frac{Dt}{K^2\Gamma_{max}{}^2}\right) erfc\left(\frac{D^{1/2}t^{1/2}}{K\Gamma_{max}}\right) \qquad (3\text{-}6)$$

where *erfc* represents the complement of the error function. The passages to get to eq. 3-6 are described in Appendix A.

3.2.3 Diffusion adsorption (present model)

When the channel is submitted to transient diffusion conditions, the typical flux conservation of the bulk concentration C is given by eq. (3-7). The boundary condition at the active wall is expressed by eq. (3-8), linking the analyte consumption flux at the active wall to the time evolution of its adsorbed form:

$$\frac{\partial C}{\partial t} + \nabla \cdot (-D\nabla C) = 0 \qquad (3\text{-}7)$$

$$\frac{\partial \Gamma}{\partial t} = D\left(\frac{\partial C}{\partial y}\right)_{y=0} = k_{on}C(\Gamma_{max} - \Gamma) - k_{off}\Gamma \qquad (3\text{-}8)$$

where D is the analyte diffusion coefficient.

3.2.4 Numerical model

The evolution of C and Γ in the present FEM model is calculated by the following set of equations, which are applied to the 2-D geometry described in Fig. 3.1. Note that the

boundary condition (3-8) is introduced in (3-7) as a consumption term assigned to the active wall, leading to eq. (3-10). The second term of eq. (3-10) equals zero in the bulk.

$$\frac{\partial C}{\partial t} + \nabla \cdot \left(-D \nabla C\right) = -k_{on}\, C\left(\Gamma'_{max} - \Gamma'\right) + k_{off}\, \Gamma' \qquad (3\text{-}9)$$

$$\frac{\partial \Gamma'}{\partial t} + \nabla \cdot \left(-D_{wall} \nabla \Gamma'\right) = k_{on}\, C\left(\Gamma'_{max} - \Gamma'\right) - k_{off}\, \Gamma' \qquad (3\text{-}10)$$

The notation $\Gamma' = \Gamma/\delta$ is here introduced to homogenise the dimensions of the two sides of eq. (3-9) and (3-10), δ representing the thickness of the active wall (see Fig. 3.1). Because of the introduction of δ, Γ' is given in mol·m^{-3} instead of mol·m^{-2}. The integral form of the model is derived in the Appendix of chapter 4 using the Galerkin's formulation

The following conditions are assumed: (i) – The solutions are sufficiently diluted to assume that the variations of the concentration do not modify the viscosity and the density of the fluid, which is also assumed to be uniform. (ii) – The channel walls are assumed to be smooth.

3.3.5 Numerical technique

The finite element software Flux-Expert™ (Astek Rhône-Alpes, Grenoble, France) is performed on a Silicon Graphics Octane 2 Unix workstation. The model is formulated in a 2-D Cartesian form and calculations are performed in 1-D and 2-D geometries as shown in Fig. 3.1a and b. The model presents 2 regions: the channel containing the bulk solution and the adsorption wall. In the channel, the analyte is characterised by its diffusion coefficient D. Γ_{max}, k_{on} and k_{off} are assigned to the active wall.

It must be stressed that the adsorption wall has a dimension δ, elongated to homogenise the mesh size and to reduce the computational time: in this wall, the diffusion coefficient D' is adapted to insure a uniform surface concentration Γ' at any time during the calculation. In what follows, Γ will be used to respect the physical meaning, even if Γ' was used for all the calculations. The active layer is always 1 mesh thick.

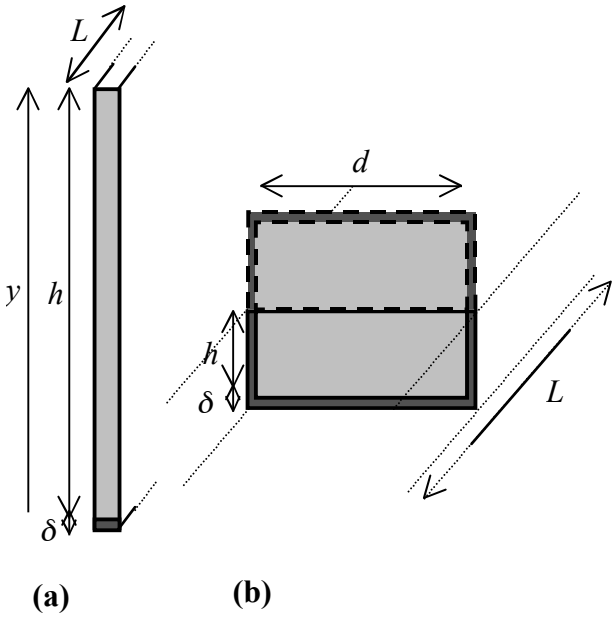

Figure 3.1. Schemes of the model, where the diffusion coefficient of the analyte D is defined in the light gray bulk region (of height h), while the initial number of active sites Γ_{max}, the diffusion coefficient to insure a uniform coverage D', the forward and reverse rates of adsorption k_{on} and k_{off} are assigned to the dark gray wall (of thickness δ). **(a)** 1-D geometry used for the model validation with h = 200 μm and δ = 0.1 μm. **(b)** 2-D geometry used for comparison with experiments. For symmetry reasons, the adsorbing surface is present on the bottom, the left and the right part of the channel (h = 50 μm; δ = 5 μm; d = 200 μm).

For all the simulations, a non-linear algorithm based on the gaussian inversion method has been used. The iterative scheme is performed with a precision criterion of 1% for convergence of the calculation at each time step. The typical time step value is 10^{-2} sec. but it was decreased to 10^{-4} seconds, for high solute concentration. The mesh sizes have been verified to be sufficiently small not to influence the results. The typical mesh size ranges from 0.1 μm (active layer) to 5 μm (top of the channel) for the validation (Fig. 3.1a) and from 5 to 20 μm for the comparison with experimental results (Fig. 3.1b). The initial conditions for transient calculations are: $C = C°$ in the channel and $\Gamma = 0$ in the wall. The physical boundary condition (3-8) being introduced as a consumption term, the only numerical boundary

conditions of the model are the Neumann homogeneous ones (no flux) at the non-active walls. For the 1-D calibration (Fig. 3.1a) the height is sufficient (200 μm) to insure semi-infinite diffusion conditions at the beginning of the adsorption (first 6 sec).

3.3 Experimental Section

3.3.1 Reagents and procedure

A 1mg/ml (6.67×10^{-6} M) solution of labelled antibody (Fluorolink Cy5 labelled antirabbit IgG, Amersham Pharmacia Biotech) was prepared in deionised water. From this, further solutions were obtained by serial dilutions with 0.01M PBS (SIGMA). The washing buffer is made of a 0.1% Tween-20 (SIGMA) solution in PBS. The adsorption of the fluorolabelled antibody was performed by filling a channel with a drop of 8 μL, placed at the inlet and pushed in with a pipette. After a certain incubation time *t*, during which adsorption occurs, the channel was emptied by air flushing, and then washed three times with 10 μL of washing buffer. If adsorption times were higher than 3 minutes, incubation was carried out in a Petri box with a wet tissue inside to avoid evaporation of the drops. As it has been already pointed out,[18] the volume of washing solution is about 100 times that of the channel, which ensures a very efficient washing step. Adsorbed proteins don't desorb or desorb very slowly (hours):[32] consequently we assume that they are not removed during the washing step. The quantity of adsorbed antibody was then measured by the confocal microscope, scanning the channel along the *Z*-axis: the strongest signal from the channel bottom wall was then collected, representing the adsorbed antibodies. Each channel was used just once. Each average value and its standard deviation were taken from 5 measurements. For PET, a surface capacity for antibody adsorption 4-fold higher than for PE used for lamination has been measured:[18] consequently, in the geometry of Fig. 3.1b, adsorption on PE has been neglected. The PET adsorbing wall is on the bottom, the right and the left parts of the channel.

3.3.2 Calibration

To convert the counts from the PMT into concentrations, a calibration curve was drawn with concentration solutions ranging from 3×10^{-9} to 6.67×10^{-6} M. Channels were filled at different concentrations and photons were counted (see paragraph *2.3.2*). At low concentrations, counts and concentrations are proportional (the linear fit was obtained with a regression coefficient of 0.998). The limit of detection of the system is 2×10^{-9} M. At this point, the bulk concentration is multiplied by the volume-to-surface ratio (V/S) of the channel, to have a surface concentration. It is worth to emphasise that all the unbound proteins are eliminated from the channel, after three washing steps with an important quantity of buffer.[18] All the proteins measured are adsorbed. It must be stressed that the values found for the kinetic constant of desorption are very low: the proteins cannot desorb in the washing timeframe that is much shorter than the time required for desorption. Experimental results can now be compared with Γ values from simulations.

3.4 Results and Discussion

To validate the model, the simulation results are compared both with the analytical solution given by Delahay and Trachtenberg[15] and with the numerical results given by Reinmuth.[16]

3.4.1 Linear Adsorption Isotherm ($\Gamma << \Gamma_{max}$)

In the range of small wall coverage (for small values of $C°$ and at low elapsed times) the variation of the surface concentration Γ is given by the analytical solution (3-6). This solution is presented in Fig. 3.2a (where Γ is normalized by the theoretical value Γ_{eq}) and compared with the simulations (1-D geometry of Fig. 3.1a and parameters listed in Tab. 3.1).

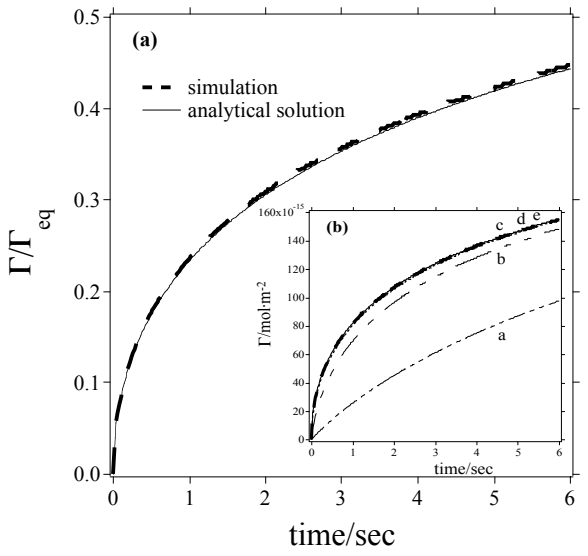

Figure 3.2. (a) The plots represent the time evolution of the wall concentration given as Γ/Γ_{eq}. The analytical solution for a linear isotherm (eq. (6),[15]) is compared with the simulation results. The values for both plots are $D = 5 \times 10^{-10}$ m^2·sec^{-1}, $\Gamma_{max} = 3.5 \times 10^{-11}$ mol·m^{-2}, $K = 2.5 \times 10^6$ m^3·mol^{-1} ($k_{on} = 2.5 \times 10^8$ m^3·mol^{-1}·sec^{-1}, $k_{off} = 100$ sec^{-1}). The simulation is run with a concentration value $C° = 4 \times 10^{-9}$ mol·m^{-3} (the independence on $C°$ was verified obtaining the same plots with a lower concentration). **(b)** Plots for calibration of k_{off}. The values for k_{off} in (a, b, c, d, e) are 0.1, 1, 10, 100, 1000 sec^{-1} respectively. At $t = 6$ sec, Γ show a difference of 6% between (c) and (d), while Γ is equal for (d) and (e) (k_{on} is varied in order to maintain a constant K). The other parameters are the same as in Fig. 3.2a.

The numerical results show a good agreement with the analytical expression as long as we are in semi-infinite conditions, i.e. until 6 seconds. After this time, the solution concentration, not renewed, starts to deplete because of the microdimensions of the geometry (here 200 μm). It is worth noting that the ratio Γ/Γ_{eq} given by eq. (3-6) is independent of the bulk concentration because at low coverages and under diffusion control, both Γ and Γ_{eq} are proportional to $C°$.[15]

The values of k_{off} that insure a diffusion limited regime are estimated in the inserted graph (Fig. 3.2b) for $D = 5 \times 10^{-10}$ m^2·sec^{-1} and for K maintained constant at the value 2.5×10^6 m^3·mol^{-1}. The value 100 sec^{-1} is chosen for further diffusion limited calculations, as its plot shows a difference of 0.6% compared with the case $k_{off} = 10$ sec^{-1} for Γ at 6 seconds.

parameters	calibration	experimental
D / $m^2 \cdot sec^{-1}$	5×10^{-10}	4×10^{-11}
Γ_{max} / $mol \cdot m^{-2}$	3.5×10^{-11}	9.26×10^{-10}
$C°$/ $mol \cdot m^{-3}$	$4 \times 10^{-8} – 4 \times 10^{-6}$	$6.67 \times 10^{-6} – 10^{-3}$
K / $m^3 \cdot mol^{-1}$	2.5×10^{6}	1.15×10^{4}
k_{on} / $m^3 \cdot mol^{-1} \cdot sec^{-1}$	$2.5 \times 10^{5} – 2.5 \times 10^{9}$	11.5
k_{off} / sec^{-1}	$0.1 – 1000$	10^{-3}
t_{max} (elapsed in simul.)/ sec	6	1800
Γ_{max}'/ $mol \cdot m^{-3}$ (δ /μm)	3.5×10^{-4} (10^{-7})	1.86×10^{-4} (5×10^{-6})

parameters ratios	calibration	experimental
$\psi = KC°$	$10^{-1} – 10$	$7.7 \times 10^{-2} – 11.5$
$\vartheta = \frac{4\pi Dt}{K^2 \Gamma_{max}^{\ 2}}$	4.9 at t_{max}	8×10^{3} at t_{max}
$t_{diff} = l^2 (2D)^{-1}$ / sec	40	130
$t_{reac} = k_{on}^{-1} C°^{-1}$ / sec	$1 – 10^{-3}$	$1.3 \times 10^{4} – 87$
Γ_{eq}/Γ_{max}	$6.7 \times 10^{-2} – 9 \times 10^{-1}$	$5.6 \times 10^{-2} – 0.89$

Table 3.1. Parameters for the calibration and the experimental comparison. The time of reaction t_{reac} in the calibration case has been calculated for $k_{on} = 2.5 \times 10^{8}$ $m^3 \cdot mol^{-1} \cdot sec^{-1}$.

3.4.2 Calibration in semi-infinite diffusion system (short times)

To validate the model, the simulations are compared with the analytical results for the adsorption kinetics given by Reinmuth for a semi-infinite diffusion system under the Langmuir conditions,[1] and a good agreement was found. (Calibration was done also with the analytical solution for the linear adsorption isotherm[16] with less than 0.6% error). The simulations are performed with the geometry of Fig. 3.1a and the values of Tab. 3.1.

In order to make the comparison, the dimensionless time ϑ is introduced:

$$\vartheta = \frac{4\pi Dt}{K^2 \Gamma_{max}^{\ 2}} \qquad (3\text{-}11)$$

As shown in Fig. 3.3, the time evolution of the dimensionless surface concentration Γ/Γ_{eq} versus $\vartheta^{1/2}$ is in a good agreement with the analytical model[1] for ψ ranging from 0.1 to 10. It

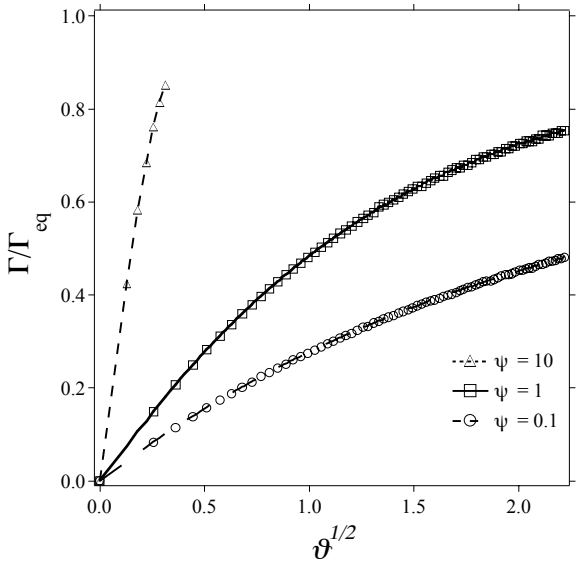

Figure 3.3. Time evolution of the wall concentration given as Γ/Γ_{eq}: plots of the simulation (markers) compared with the results of Reinmuth (lines)[1] for a semi-infinite linear diffusion controlled system. The parameters are $D = 5 \times 10^{-10}$ m^2·sec^{-1}, $\Gamma_{max} = 3.5 \times 10^{-11}$ mol·m^{-2}, $K = 2.5 \times 10^6$ m^3·mol^{-1} ($k_{on} = 2.5 \times 10^8$ m^3·mol^{-1}·sec^{-1}, $k_{off} = 100$ sec^{-1}). $C° = 4 \times 10^{-8}$, 4×10^{-7}, 4×10^{-6} mol·m^{-3} for $\psi = 0.1$, 1, 10 respectively.

also illustrates that the time to reach equilibrium coverage decreases with the initial concentration $C°$ (*i.e.* with ψ, which has been called "the motivating force to adsorption"[1]). The values of k_{off} that insure a diffusion limited regime of adsorption have been estimated. The PET microchannel surface is not smooth as modelled, so that the microscopic area, with all of its undulations, crevices and asperities is larger than the geometric, or projected area. An analogy with the treatment for diffusion to microelectrodes made by Bard[33] can be made. The diffusion layer generated during the adsorption is much larger than the scale of roughness: therefore, on the scale of the diffusion layer, the channel surface appears flat; the surfaces connecting equal concentrations in the diffusion layer are planes parallel to the surface; and the area of the diffusion field is the geometric area of the electrode. Molecules

diffusing to the surface come, on the average, from so far away that the added distance (and time) required to reach an active place on the surface becomes negligible.

3.4.3 Finite height 1-D diffusion adsorption process: depletion effect (long times)

After 6 seconds, the solute starts to be depleted because of the microdimensions of the geometry (the present model is 200 μm high). This phenomenon is illustrated in Fig. 3.4a, showing the variation of $C/C°$ with the distance from the wall (y) for different times after the beginning of the adsorption and for the same parameters as Fig. 3.3 (diffusion control).

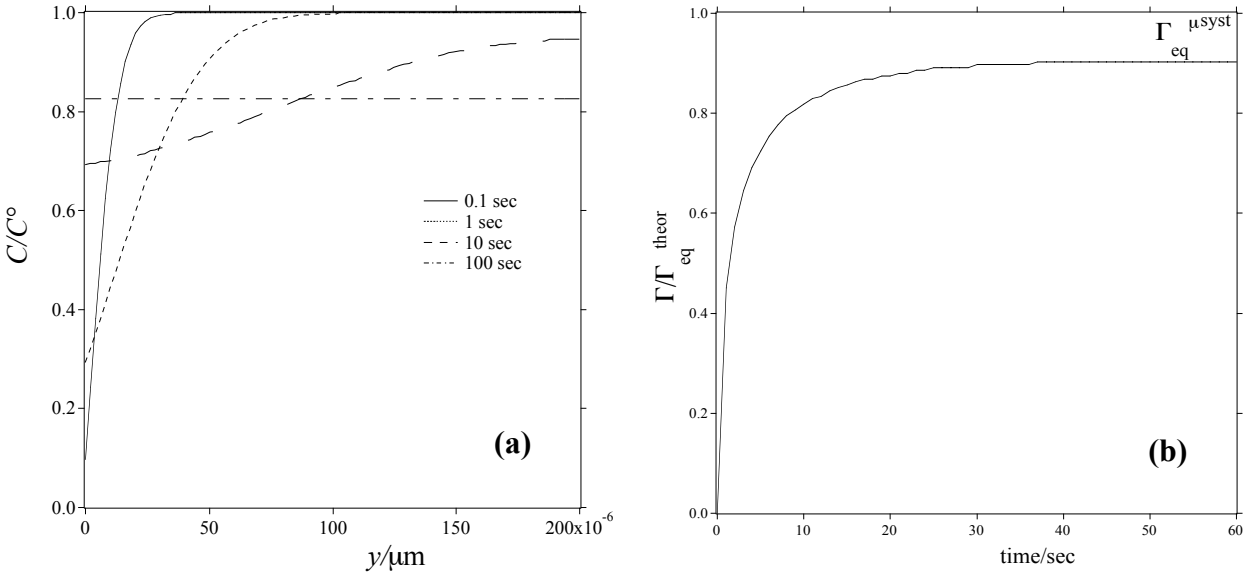

Figure 3.4. (a) Variations of $C/C°$ with distance from the active wall (y) for different times (in seconds) after the beginning of adsorption. $C°$ and the other parameters are the same than in Fig. 3.3. **(b)** Time evolution of Γ in a microsystem showing that Γ_{eq}^{theor} is not reached.

Concentration depletion extends to the whole height after 10 seconds. At 100 seconds the equilibrium is reached: C_{eq} is about 82% of $C°$ (instead of $C_{eq} = C°$ as in a semi-infinite system). Consequently the concentration at equilibrium in eq. (3-4), C_{eq}, is not equal to $C°$ any longer, and this equation should be rewritten as:

$$\frac{\Gamma_{eq}^{\mu syst}}{\Gamma_{max}} = \frac{KC_{eq}}{1+KC_{eq}} \qquad (3\text{-}12)$$

The final value of $\Gamma_{eq}^{\mu syst}$ is therefore lower than the theoretical one attainable in a bigger system or in a system where the solution is renewed (e.g. with a flow).

The time evolution of Γ/Γ_{eq} is shown in Fig. 3.4b: it is illustrated that $\Gamma_{eq}^{\mu syst}$ (whose value can be calculated from eq. 12) is reached instead of Γ_{eq}^{theor} (corresponding to Γ_{eq} of eq. (3-4)). In Tab. 3.2 the ratios $\Gamma_{eq}^{\mu syst}/\Gamma_{max}$ obtained in this system are compared with theoretical ones, Γ_{eq}^{theor}. We can observe that $\Gamma_{eq}^{\mu syst}$ is nearer the theoretical one at high ψ (high $C°$) due to the lower bulk depletion.

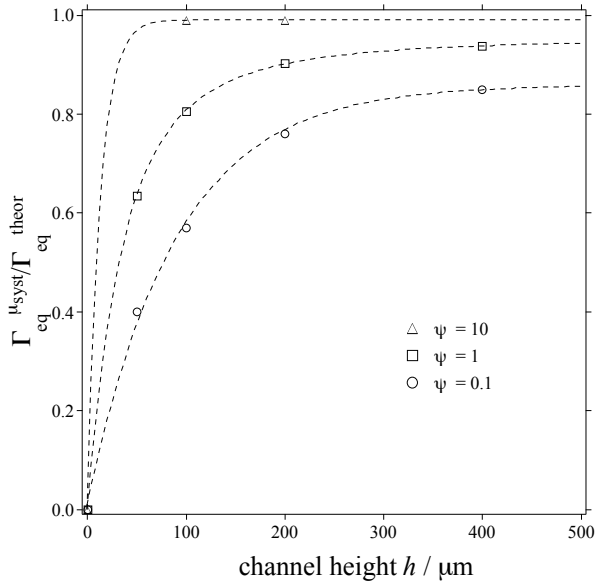

Figure 3.5. Calculated coverage normalised by the theoretical value versus the channel height for different concentrations (expressed as ψ). All the parameters are those of Fig. 3.3.

To illustrate how the channel dimensions influence the adsorption, the ratio between the experimental and the theoretical coverage was plotted versus the height of the channel as shown in Fig. 3.5. Fitting the results obtained by simulations with different channel heights (*i.e.* for different *h* in Fig. 3.1a) leads to:

$$\frac{\Gamma_{eq}^{\mu syst}}{\Gamma_{eq}^{theor}} = a_1(1 - e^{-a_2 h}) \qquad (3\text{-}13)$$

The parameters a_1 and a_2 are dependent on $C°$ and the values are shown in Tab. 3.2.

ψ	theoretical $\frac{\Gamma_{eq}}{\Gamma_{max}}$	experimental $\frac{\Gamma_{eq}}{\Gamma_{max}}$	difference	a_1	$a_2/\mu m^{-1}$
10	9.09×10^{-1}	9.02×10^{-1}	-0.77 %	1	$3.4 \cdot 10^{-2}$
1	5×10^{-1}	4.51×10^{-1}	-9.8 %	0.93	$2.2 \cdot 10^{-2}$
0.1	9.09×10^{-2}	6.66×10^{-2}	-26.7 %	0.85	$1.1 \cdot 10^{-2}$

Table 3.2. Comparison between the theoretical and the experimental Γ_{eq}/Γ_{max} reached in the microchannel of Fig. 3.1a. The theoretical Γ_{eq}/Γ_{max} values are calculated from eq. (3-4). The experimental Γ_{eq}/Γ_{max} is obtained from simulations run with the geometry of Fig. 3.1a and the values for the calibration of Tab. 3.1 (simulations of Fig. 3.3, at longer times). a_1 and b_2 are constants for eq. (3-13).

3.4.4 φ: a parameter to define the non-ideality of microsystems for adsorption

Since an effective coverage is suitable in many applications (for instance, a microchannel for ELISA should be uniformly and effectively covered with the primary antibody in order to increase to sensitivity of the immunoassay), the general conditions to fulfill in order to avoid depletion have been explored. To do that, the values of coverage at equilibrium in microsystems ($\Gamma_{eq}^{\mu syst}$) obtained from simulations were normalised with the equilibrium coverage value obtained under semi-infinite diffusion (Γ_{eq}^{theor}, from eq. (3-4)). This normalised adsorption $\Gamma_{eq}^{\mu syst}/\Gamma_{eq}^{theor}$ was correlated with the initial number of solute moles present in that microsystem ($N° = C°·V = C°·A·h$, where V, A, h are the volume, the active surface area and the height of the microsystem). To enable a consistent comparison with ideal conditions this quantity was also normalised by the number of moles the wall can theoretically adsorb under semi-infinite diffusion ($N_{wall}^{\infty} = \Gamma_{eq}^{theor} \cdot A$). Keeping into account eq. (3-4) the ratio $N°/N_{wall}^{\infty}$ can be written as follows:

$$\frac{\mathcal{N}^{\circ}}{\mathcal{N}_{\text{wall}}^{\infty}} = \frac{C^{\circ}h}{\Gamma_{\text{eq}}^{\text{theor}}} = \frac{h}{K\Gamma_{\max}}(1+\psi) = \varphi(1+\psi) \qquad (3\text{-}14)$$

where φ (= $h/K\Gamma_{max}$) represents the asymptotic limit of eq. (3-14) for ψ <<1 (*i.e.* very low initial concentration or low K values). The parameter φ is independent of the initial solution concentration and is, consequently, an intrinsic characteristic of any microsystem where adsorption takes place. It corresponds to the lowest possible coverage that can occur in a microsystem in relation to the corresponding ideal system.

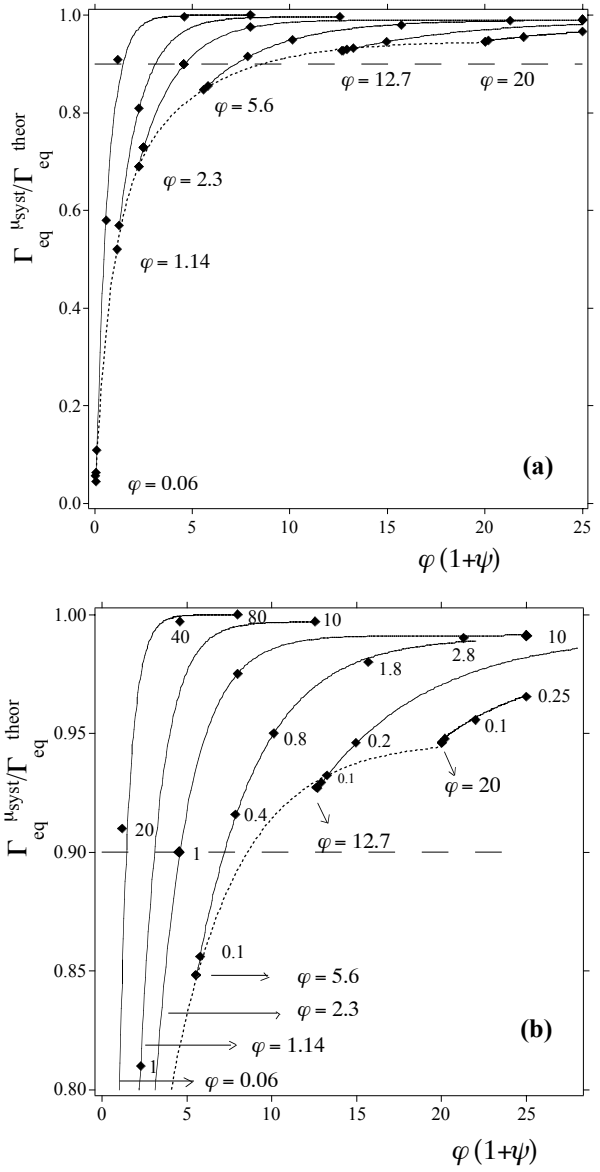

Figure 3.6. Working curves to estimate the coverage in a microsystem; the plots show the evolution of the coverage in a microsystem compared to the coverage in the corresponding ideal semi-infinite system in function of ψ and for different values of $\varphi = h/K\Gamma_{max}$. Each full line curve is obtained for growing values of ψ. The lowest abscissa value of each full line curve corresponds to φ (from left to right φ = 0.06, 1.14, 2.3, 5.6, 12.7, 20) and the corresponding $\Gamma_{eq}^{\mu syst}/\Gamma_{eq}^{theor}$ is the lowest attainable in that microsystem (simulations run with $\psi = 10^{-3}$). The points have been verified for different h (different h values in Fig. 3.1a), K and Γ_{max} values, changing C° in order to keep ψ constant. The dotted line, connecting all the points with abscissa equal to φ, represents the limit under which the coverage cannot fall in a microsystem characterised by the corresponding φ. Fig. 3.6**(b)** is an enlargement of Fig. 3.6**(a)** to show the ψ values. The ψ values are written near the corresponding point.

The ratio $\Gamma_{eq}^{\mu syst}/\Gamma_{eq}^{theor}$ is represented in Fig. 3.6 as a function of $N°/N_{wall}^{\infty}$ (3-14). Each full line curve represents the normalised adsorption (micro/ideal system) as a function of ψ for a different φ value (*i.e.* a different microsystem).

As just said, the lowest possible abscissa value for each curve is φ. In this way, the dotted line connecting all the φ values represents the lowest equilibrium coverages that can occur in different microsystems (compared to the theoretical ideal systems).

In Fig. 3.6b it can be observed that for the same ψ values, $\Gamma_{eq}^{\mu syst}/\Gamma_{eq}^{theor}$ increases with φ. In fact when the volume-to-surface ratio, *i.e.* h is small compared to $K\Gamma_{max}$, the depletion of the solution is very high, and the analyte amount adsorbed at equilibrium is small compared to an ideal system (it can be 0.05% of the corresponding semi-infinite system for $\psi = 0.01$ and $\varphi = 0.06$).

When the h value is high compared to $K\Gamma_{max}$, the microsystem behaviour tends to that of an ideal system: for instance for $\varphi \geq 9$ (*i.e.* h is 9 times the product $K\Gamma_{max}$) we can consider of being above the microsystem limitation which is due to the solution depletion, as $\Gamma_{eq}^{\mu syst}/\Gamma_{eq}^{theor}$ is never less than 90% (reachable for $\psi = 0.01$ and less; see horizontal dashed line in Fig. 3.6).

After having estimated the φ value of a microsystem of interest, the plots in Fig. 3.6 can be used as working curves to predict the final coverage in that microsystem.

3.4.5 Isotherm of IgG adsorption on PET

The experimental isotherm of IgG adsorption on photoablated PET microchannels is shown in Fig. 3.7a, where the Γ_{eq} values are measured at 30 min (corresponding to the final values of the time evolutions of Fig. 3.7c). The initial solution concentration $C°$ is assumed not to deplete during the adsorption phenomenon, since relatively high $C°$ values are used as shown in Tab. 3.1. This assumption is verified with the simulations below (see: Appendix B: validity

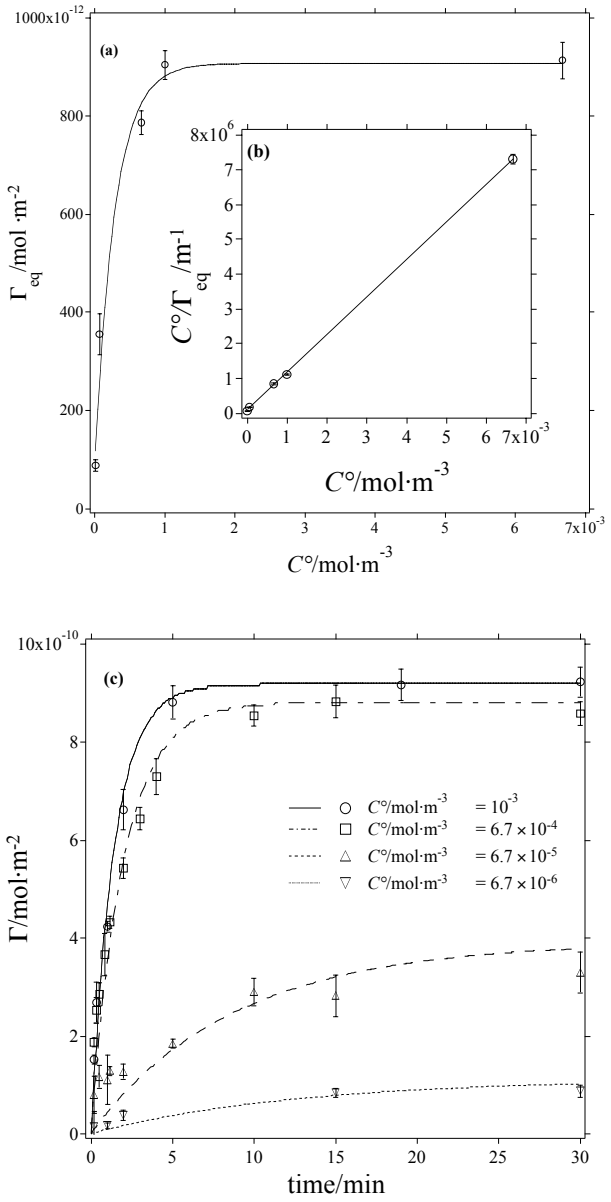

Figure 3.7. **(a)** Isotherm of adsorption of anti-rabbit IgG on laser-ablated PET obtained from the experimental results at 30 min of Fig. 3.7c. The fit has the only purpose of illustrating the trend of the isotherm. **(b) (inside)** Linearisation of the adsorption isotherm, following eq. (15): regression coefficient = 0.999, slope = 1.08×10^9 $m^2 \cdot mol^{-1}$, intercept = 9.40×10^4 m^{-1}, from which $\Gamma_{max} = 9.26 \times 10^{-10}$ $mol \cdot m^{-2}$ and $K = 1.15 \times 10^4$ $m^3 \cdot mol^{-1}$. **(c)** Simulations (lines) compared with experimental results (markers). Calculations are run with $D = 4 \times 10^{-11}$ $m^2 \cdot sec^{-1}$, $\Gamma_{max} = 9.26 \times 10^{-10}$ $mol \cdot m^{-2}$, $K = 1.15 \times 10^4$ $m^3 \cdot mol^{-1}$ ($k_{on} = 11.5$ $m^3 \cdot mol^{-1} \cdot sec^{-1}$ and $k_{off} = 10^{-3}$ sec^{-1}). The initial concentrations for experiments and simulations are $C° = 10^{-3}$, 6.67×10^{-4}, 6.67×10^{-5}, and 6.67×10^{-6} $mol \cdot m^{-3}$.

remark), since a moderate depletion of the bulk concentration cannot be detected with the confocal microscope. To obtain Γ_{max} and K (necessary for the simulations fitting the experimental kinetics of adsorption shown in Fig. 3.7c and carried out with the geometry of Fig. 3.1b), the adsorption isotherm equation (eq. (3-3)) is linearised as follows:[34]

$$\frac{C°}{\Gamma_{eq}} = \frac{1}{K\Gamma_{max}} + \frac{C°}{\Gamma_{max}} \qquad (3\text{-}15)$$

3.4.5.1 Γ_{max} and K fitting

The linearised isotherm is reported in Fig. 3.7b (inside Fig. 3.7a). Reporting $C°/\Gamma_{eq}$ versus $C°$, Γ_{max} and K are provided as the respective reciprocals of the slope and the intercept, giving the fitted values $\Gamma_{max} = 9.26 \times 10^{-10}$ mol·m^{-2} and $K = 1.15 \times 10^{4}$ m^{3}·mol^{-1}. Γ_{max} can also be calculated by taking into account the area of the antibody molecule (14×14 nm^2 [35]), resulting in $\Gamma_{max} = 1.064 \times 10^{-8}$ mol·m^{-2}. This estimation implies a compact monolayer of IgG molecules. The deviation from the fitted value can be explained by the fact that PET surface is not so active in physisorption,[36] leading to a decrease of the active sites concentration (in the ratio of 1/10 mol·m^{-2}).

3.4.5.2 Kinetic rates fitting: a reaction-limited case

The IgG adsorption on PET versus the incubation or adsorption time t is given in Fig. 3.7c (markers) for different antibody concentrations. The corresponding simulations, represented by lines, are performed with the geometry of Fig. 3.1b. The parameters for simulations are reported in Tab. 3.1. The kinetics rates obtained from the experimental fitting are far below the diffusion limitation ones ($k_{off} = 10^{-3}$ sec^{-1} instead of the [1 – 100] sec^{-1} range for near diffusion control).

An evaluation of the conditions corresponding to limitations by diffusion or kinetics can be done.[37] In Tab. 3.1 we compare the characteristic reaction time $t_{reac} = 1/k_{on}C°$ with the typical time of diffusion $t_{diff} = h^2/2D$, where h is the diffusion length (the values used are those of Fig. 3.7c). The time t_{diff} equals 130 sec while t_{reac} varies from 87 sec (higher $C°$ in Fig. 3.7c) to about 3.6 hrs (lower $C°$): in the first case (high $C°$), the reaction occurs in the same time order as diffusion, resulting in a mixed regime. At lower concentrations, the reaction is so slow that only a small amount of antibodies is adsorbed, leading to a near-wall C value just below $C°$. Simulations of the concentration show a weak gradient profile across the channel, which is established in some minutes because the kinetics slows the process down (for

comparison, the gradient shown in Fig. 3.4 for pure diffusional control is established in 0.1 sec).

Protein adsorption controlled by kinetics was reported several times. Van Dulm and Norde[19] explained slow adsorption of albumin on negatively charged polystyrene with the fact that albumin molecules have to cross an energy barrier caused by overlapping electric fields from the negative charges on the sorbent and the protein. Wojciechowski et al.[20] found a similar behaviour for adsorption of fibrinogen on various surfaces. In an extensive study of adsorption of different proteins on different substrates, Young, Pitt and Cooper[21] found a kinetic limited process for IgG adsorption on polyvinyl chloride, polyethylene and polyether polyurethaneurea. Again, the existence of an energy barrier is given to explain this kind of limitation, also encountered in our system.

Antibody adsorption on bare substrates is the most simple and one of the most popular immobilization methods, even if it leads to low surface coverage and low activity of the physisorbed antibodies.[36] To overcome this limitations adsorption in gels,[38, 39] porous media[30, 40] or bead-beds[41] are often used to enhance the coverage.

3.5 Conclusions

The time evolution of the wall adsorption of one species in 1D and 2D microsystems has been studied under static conditions. The employed finite element model considers the diffusion of the species in solution, coupled to the adsorption kinetics on the sorbent surface. The analyte diffusion coefficient, the density of the active sites present on the surface and the kinetic rates of adsorption and desorption are taken into account. The model has been validated under diffusion control by comparison with analytical models of the Langmuir isotherm.

It is observed that the adsorption can be limited by the depletion of the bulk solution, due to the microdimensions of the system. Accordingly, for low initial solution concentrations, the coverage values at equilibrium can be markedly lower than the theoretical ones. A working curve and a new non-dimensional parameter ($\varphi = h/K\Gamma_{max}$) are provided in order to predict the depletion effect on the coverage values in any static situation. To overcome the limitations induced by the microdimensions, the channel height h (*i.e.* the volume-to-surface ratio) must be higher than 10 $K\Gamma_{max}$, insuring 90% of the coverage obtainable in a semi-infinite diffusion system. The next chapter will consider different ways of renewing the solution in order to reach the full coverage in a microsystem.

Adsorption of fluorescently labelled IgG antibodies on the walls of a laser ablated PET microchannel was measured by the confocal microscope described in details in chapter 2. Fitting the simulations to the experimental time evolution reveals a kinetic controlled adsorption. For symmetry reasons, the study carried out with this model can be extended to microchannels adsorbing on all the four walls.

Appendix A.

In the following the passages to get eq. (3-6) are described.

Fick's law is written as:

$$\frac{\partial C(x,t)}{\partial t} = D\frac{\partial^2 C(x,t)}{\partial x^2} \qquad (3A-1)$$

After Laplace transform we get:

$$C(x,s) = \frac{C(x,0)}{s} + A(s)e^{-\sqrt{\frac{s}{D}}x} \qquad (3A-2)$$

where A is an integration constant and s the parameter of the transform.

The constant A is determined from the transform of eq. (3-5) and there results:

$$C(x,s) - \frac{C(x,0)}{s} = \frac{C(0,0)e^{-\sqrt{\frac{s}{D}}x}}{\sqrt{s}\left(\frac{\sqrt{D}}{K} + \sqrt{s}\right)} \qquad (3A-3)$$

The inverse transform is:

$$\frac{C}{C^\circ} = 1 - e^{\left(\frac{x}{\Gamma_{max}K} + \frac{Dt}{\Gamma_{max}{}^2K^2}\right)} erfc\left(\frac{x}{2\sqrt{Dt}} + \frac{\sqrt{Dt}}{\Gamma_{max}K}\right) \qquad (3A-4)$$

The surface concentration Γ is readily obtained by eq (3A – 4) keeping into account eq. (3-5), and it results in eq. (3-6). The ratio Γ/Γ_{eq} given by eq. (3-6) is independent off the bulk concentration of adsorbable substance because the adsorption is linearised in this treatment (as described in eq. (3-5)).

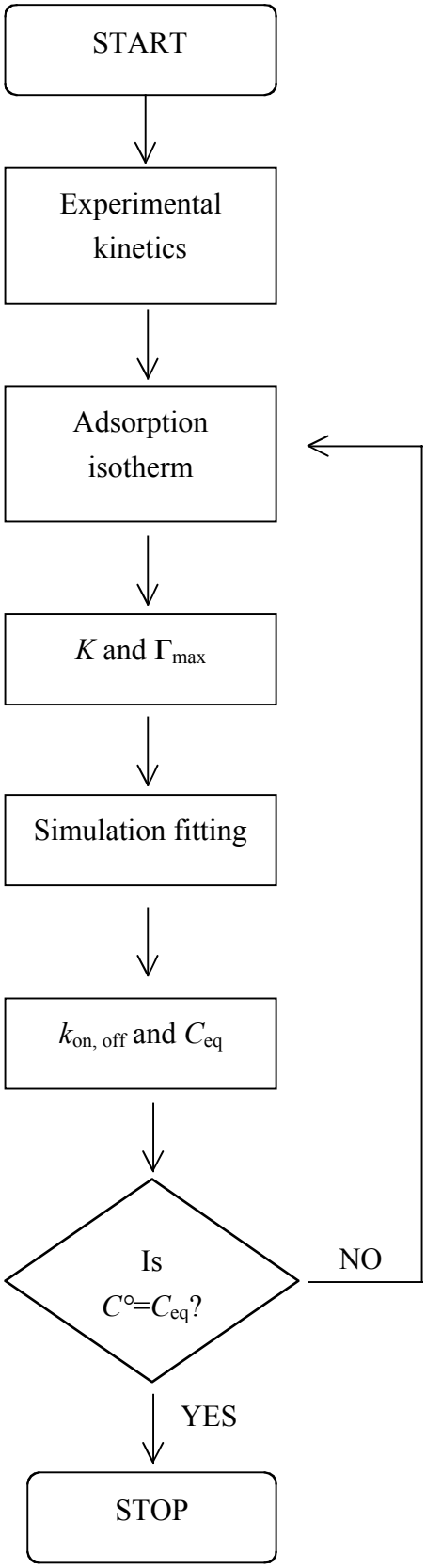

Scheme 3.A

Appendix B: Depletion effect: validity remark

In Tab. 3.A the ratios Γ_{eq}/Γ_{max} obtained from simulations are compared with the theoretical ones, calculated from eq. (3-4). The values are similar only for the higher $C°$ values, due to the depletion occurring in this microsystem (h = 50 μm). Indeed, at low $C°$, the initial assumption ($C_{eq} = C°$) is not valid: therefore, the true values of C_{eq} from simulations at 30 minutes are employed to determine a new isotherm of adsorption in function of C_{eq} (not shown). For this, eq. (3-15) is rewritten by replacing $C°$ with C_{eq}. This isotherm provides 0.2% and 4% deviation for Γ_{max} and K respectively, confirming the validity of previous fitted values used for Fig. 3.7c. This iterative process is illustrated in the scheme 3.A.

$C°$/ mol·m^{-3}	theoretical $\frac{\Gamma_{eq}}{\Gamma_{max}}$	experimental $\frac{\Gamma_{eq}}{\Gamma_{max}}$	difference %	$C_{eq}/C°$
10^{-3}	0.92	0.89	3.3	98 %
6.67×10^{-4}	0.88	0.86	2.3	97 %
6.67×10^{-5}	0.43	0.38	11.6	86 %
6.67×10^{-6}	0.071	0.056	21.1	81 %

Table 3.A. Comparison between the theoretical and the experimental Γ_{eq}/Γ_{max} attainable in the microchannel used for comparison with experiments (Fig. 3.1b). The experimental Γ_{eq}/Γ_{max} deviates more from the theoretical one as $C°$ is lowered. C_{eq} follows the same behaviour, deviating from $C°$.

References:

(1) Reinmuth, W. H. *Journal of Physical Chemistry* **1961**, *65*, 473-&.

(2) Dodge, A.; Fluri, K.; Verpoorte, E.; de Rooij, N. F. *Analytical Chemistry* **2001**, *73*, 3400-3409.

(3) Koutny, L. B.; Schmalzing, D.; Taylor, T. A.; Fuchs, M. *Analytical Chemistry* **1996**, *68*, 18-22.

(4) Mondal, K.; Lalvani, S. B. *Separation Science and Technology* **2000**, *35*, 2583-2599.

(5) Paces, M.; Kosek, J.; Marek, M.; Tallarek, U.; Seidel-Morgenstern, A. *Electrophoresis* **2003**, *24*, 380-389.

(6) Golshanshirazi, S.; Guiochon, G. *Analytical Chemistry* **1988**, *60*, 2364-2374.

(7) Glaser, R. W. *Analytical Biochemistry* **1993**, *213*, 152-161.

(8) Skidmore, G. L.; Horstmann, B. J.; Chase, H. A. *Journal of Chromatography* **1990**, *498*, 113-128.

(9) Lan, Q. D.; Bassi, A. S.; Zhu, J. X.; Margaritis, A. *Chemical Engineering Journal* **2001**, *81*, 179-186.

(10) Mao, Q. M.; Stockmann, R.; Prince, I. G.; Hearn, M. T. W. *Journal of Chromatography* **1993**, *646*, 67-80.

(11) Rowe, G. E.; Margaritis, A.; Lan, Q.; Bassi, A. S.; Zhu, J. X. *Biotechnology and Bioengineering* **1999**, *65*, 613-621.

(12) Horstmann, B. J.; Chase, H. A. *Chemical Engineering Research & Design* **1989**, *67*, 243-254.

(13) Horstmann, B. J.; Chase, H. A. *Bioseparation* **1998**, *7*, 145-157.

(14) McCoy, M. A.; Liapis, A. I. *Journal of Chromatography* **1991**, *548*, 25-60.

(15) Filippov, L. K.; Filippova, N. L. *Journal of Colloid and Interface Science* **1997**, *189*, 1-16.

(16) Delahay, P.; Trachtenberg, I. *Journal of the American Chemical Society* **1957**, *79*, 2355-2362.

(17) Wojciechowski, P. W.; Brash, J. L. *Journal of Colloid and Interface Science* **1990**, *140*, 239-252.

(18) Rossier, J. S.; Gokulrangan, G.; Girault, H. H.; Svojanovsky, S.; Wilson, G. S. *Langmuir* **2000**, *16*, 8489-8494.

(19) Vandulm, P.; Norde, W. *Journal of Colloid and Interface Science* **1983**, *91*, 248-255.

(20) Wojciechowski, P.; Tenhove, P.; Brash, J. L. *Journal of Colloid and Interface Science* **1986**, *111*, 455-465.

(21) Young, B. R.; Pitt, W. G.; Cooper, S. L. *Journal of Colloid and Interface Science* **1988**, *125*, 246-260.

(22) Reichert, U.; Linden, T.; Belfort, G.; Kula, M. R.; Thommes, J. *Journal of Membrane Science* **2002**, *199*, 161-166.

(23) Davies, M. C.; Green, R.; Chen, X. Y.; Roberts, C. J.; Shakesheff, K. M.; Tendler, S. S. B.; Williams, P. M. *Abstracts of Papers of the American Chemical Society* **1995**, *209*, 6-POLY.

(24) Rossier, J. S.; Girault, H. H. *Lab on a Chip* **2001**, *1*, 153-157.

(25) Schaaf, P.; Dejardin, P. *Colloids and Surfaces* **1988**, *31*, 89-103.

(26) Ocvirk, G.; Tang, T.; Harrison, D. J. *Analyst* **1998**, *123*, 1429-1434.

(27) McFarland, E. G.; Michielsen, S.; Carr, W. W. *Applied Spectroscopy* **2001**, *55*, 481-489.

(28) Ljunglof, A.; Thommes, J. *Journal of Chromatography A* **1998**, *813*, 387-395.

(29) Ljunglof, A.; Hjorth, R. *Journal of Chromatography A* **1996**, *743*, 75-83.

(30) Linden, T.; Ljunglof, A.; Kula, M. R.; Thommes, J. *Biotechnology and Bioengineering* **1999**, *65*, 622-630.

(31) Moreno, E. C.; Kresak, M.; Kane, J. J.; Hay, D. I. *Langmuir* **1987**, *3*, 511-519.

(32) Giacomelli, C. E.; Avena, M. J.; DePauli, C. P. *Journal of Colloid and Interface Science* **1997**, *188*, 387-395.

(33) Bard A. J., F. L. R. *Electrochemical methods : fundamentals and applications*; Wiley: New York, 2001.

(34) Mazzone, D.; Università degli studi di Genova, 1998.

(35) Green, R. J.; Davies, J.; Davies, M. C.; Roberts, C. J.; Tendler, S. J. B. *Biomaterials* **1997**, *18*, 405-413.

(36) Lin, J. N.; Chang, I. N.; Andrade, J. D.; Herron, J. N.; Christensen, D. A. *Journal of Chromatography* **1991**, *542*, 41-54.

(37) Mason, T.; Pineda, A. R.; Wofsy, C.; Goldstein, B. *Mathematical Biosciences* **1999**, *159*, 123-144.

(38) Vazquez-Lira, J. C.; Camacho-Frias, E.; Pena-Alvarez, A.; Vera-Avila, L. E. *Chemistry of Materials* **2003**, *15*, 154-161.

(39) Mansur, H.; Orefice, R.; Pereira, M.; Lobato, Z.; Vasconcelos, W.; Machado, L. *Spectroscopy-an International Journal* **2002**, *16*, 351-360.

(40) Finette, G. M. S.; Mao, Q. M.; Hearn, M. T. W. *Journal of Chromatography A* **1997**, *763*, 71-90.

(41) Sato, K.; Tokeshi, M.; Odake, T.; Kimura, H.; Ooi, T.; Nakao, M.; Kitamori, T. *Analytical Chemistry* **2000**, *72*, 1144-1147.

Dynamic Protein Adsorption in Microchannels by "Stop-Flow" and Continuous Flow

(based on Lionello, A.; Josserand, J.; Jensen, H.; Girault, H. H. *Lab on a Chip* **2005**, *10*, 1096-1103)

4.1 Introduction

In chapter 3 we showed that during a microimmunoassay the solution of adsorbing species might undergo a depletion due to the large surface-to-volume ratio intrinsic to microsystems. This depletion leads to a smaller surface concentration of adsorbed species, either the primary antibody or the antigen, that may result in a low signal during the detection. Renewing the solution by sequential fillings of the microsystem (multiple "stop-flow" incubations) or by continuously flowing the solution in the microchannel can alleviate this drawback.

The "stop-flow" method consists in stopping the flow to allow the analyte more time to diffuse to the active wall. This "stop-flow" methodology is here simulated in a multi-step way and the adsorption obtained is compared with that obtained with flowing conditions.

Many examples of continuous flowing heterogeneous microimmunoassays can be found where the analyte is flowed past the antibody bound to a polymer surface[1-4] or functionalised surfaces.[5] Sometimes, even the binding of the primary antibody is performed under flow conditions.[6]

The process of adsorption under flowing conditions is also encountered in some biosensors for the determination of the affinity and dissociation kinetic constants of biological systems. In the "Biacore" biosensors, based on surface plasmon resonance detection principle, kinetic constants are usually obtained with the software accompanying the sensor.[7] Some deviations from the experimental results were observed though, leading to the elaboration of models that take into account the different aspects affecting the binding. A model to interpret the

interaction between any number of soluble and immobilised species on a surface was proposed[8] in which special attention was brought to the rate constants of association and dissociation as the main parameters governing diffusion or reaction controlled processes. Another thorough study of the relations between the kinetic constants and the limitation processes was done by Yarmush.[9] Myszka and coworkers[10] introduced the two compartments model in which the analyte diffuses and binds to the ligand in an unstirred layer adjacent to the surface. This model was improved[11] and used several times[12, 13] to analyse biochemical binding processes. Another model has also been proposed for coupling transport phenomena in a flow channel with hindered diffusion transport and reaction in the hydrogel layer of a Biacore sensor.[14] Also, with this device, the antibody/antigens systems were studied using a Langmuir isotherm model.[15]

More generally, a mathematical approach to adsorption kinetic in a flow cell has been developed by Filippov[16] and mathematical models of adsorption and transport processes in capillary electrochromatography have been presented.[17]

In the present work, the finite element method (FEM) is used to study the coupling of adsorption kinetics to convection-diffusion phenomena in microchannels, providing the time evolution of the concentration of one species, both in solution and on the walls of the microchannel. It can be used to study the adsorption of the primary antibody onto a substrate or to study the reaction between a biomolecule and the attached antibody. An analytical study to provide the number of “stop-flow” steps necessary to obtain the full coverage is addressed and validated with simulation results.

The continuous flow is studied with the FEM model and the conditions to obtain a uniform coating along the channel are analysed. This leads to criteria for setting the flow velocities that allow a comparison with the “stop-flow” procedure in terms of sample consumption. The channel length used in the simulations is 1 mm long, and the flow velocity range is [10-100]

μm·sec^{-1}. The possibility to extend the present results to longer channels by using higher velocity values (scaling based on the residence time conservation) has been experimentally verified.

4.2 Theory

4.2.1 Adsorption in microchannels

We consider the adsorption process according to the Langmuir isotherm model. The expression relating the concentration of analyte adsorbed on the surface, Γ, to the one in solution *C*, at equilibrium, is:

$$\frac{\Gamma_{eq}^{theor}}{\Gamma_{max}} = \frac{KC^{\circ}}{1+KC^{\circ}} = \frac{\psi}{1+\psi} \qquad (4\text{-}1)$$

where Γ_{eq}^{theor} is the surface concentration at equilibrium, Γ_{max} is the initial concentration of the active sites, *K* is the thermodynamic constant of adsorption, and C° the initial concentration of the solution. The parameter ψ, "the motivating force to adsorption", is equal to KC°.[18] In a microsystem submitted to static adsorption without renewing the solution, the analyte concentration at equilibrium is no longer C° but C_{eq}. As a consequence, the maximum surface concentration value attainable is $\Gamma_{eq}^{\mu syst}$, lower than Γ_{eq}^{theor}, and eq. (4-1) should be written as:

$$\frac{\Gamma_{eq}^{\mu syst}}{\Gamma_{max}} = \frac{KC_{eq}}{1+KC_{eq}} \qquad (4\text{-}2)$$

4.2.2 The "stop-flow" procedure (far from full coverage)

This procedure consists in renewing the solute by a fast injection that is then stopped to allow an adsorption step under static conditions. As soon as the "intermediate" equilibrium $\Gamma_{eq}^{\mu syst}$

has been attained, the depleted solution is renewed again and again up to Γ_{eq}^{theor}. The number of loads needed to attain Γ_{eq}^{theor} can be estimated in the case $\Gamma_{eq}^{\mu syst} << \Gamma_{max}$, *i.e.* when KC_{eq} <<1. Under this assumption, KC_{eq} can be neglected in the denominator of eq. (4-2), which becomes:

$$\Gamma_{eq}^{\mu syst} = KC_{eq}\Gamma_{max} \qquad (4\text{-}3)$$

• **1 step adsorption** - The total number of the analyte moles n_{TOT} present in the channel is equal to the number of moles injected, which distributes between the adsorbing wall and the depleted bulk: $n_{TOT} = n_{inj} = n_{wall}^{eq} + n_{sol}^{eq}$, where n_{inj} ($=C°\cdot Vol$) indicates the number of moles injected in the system, n_{wall}^{eq} and n_{sol}^{eq} respectively the moles adsorbed on the active surface and those still in solution at equilibrium.

The mass balance can be rewritten as $n_{TOT} = \Gamma_{eq}^{\mu syst} A + C_{eq} Vol$, where A and Vol are the active surface area and the volume of the microchannel. Keeping into account eq. (4-3), the following equation is obtained:

$$\frac{n_{wall}^{eq}}{n_{TOT}} = \frac{K\Gamma_{max}AVol^{-1}}{1 + K\Gamma_{max}AVol^{-1}} = \frac{1}{1+\varphi} = \alpha \qquad (4\text{-}4)$$

where α indicates the relative adsorbing capacity of the system, giving the ratio between the number of moles of adsorbed analyte and the total number of analyte present in the system. The parameter φ is the dimensionless parameter introduced in chapter 3 that represents the intrinsic ideality for binding of the microchannel ($\varphi = Vol/AK\Gamma_{max}$). More precisely, with this parameter φ it is possible to describe the adsorption in a microsystem compared to an ideal system (in semi-infinite diffusion) with the same Γ_{max} and K. A low φ value means that Γ_{max} and K are high compared to the volume-to-surface ratio, leading to a consequent important bulk depletion effect.

• **Multi-step "stop-flow"** – Contrary to the first step, the initial surface concentration on the wall prior to another injection is not zero and at load *N*, a number $n_{wall,N-1}^{eq}$ of molecules has already been adsorbed, leading to:

$$n_{TOT,\,N} = n_{inj} + n_{wall,N-1}^{eq} \qquad (4\text{-}5)$$

The number of moles injected in the channel n_{inj} is considered to be the same at each step (*i.e.* $C°\cdot Vol$). Due to the fact that the equilibrium conditions are independent of the initial distribution of the species between the surface and the solution, eq. (4-4) can be extrapolated to the step *N* giving eq. (4-6a); replacing eq. (4-5) in eq. (4-6a) gets to eq. (4-6b); by analogy with eq. (4-6b), we can write $n_{wall,N-1}^{eq} = \alpha\,(n_{inj} + n_{wall,\,N-2}^{eq})$ that can be replaced in eq. (4-6b) giving eq. (4-6c).

$$\frac{n_{wall,N}^{eq}}{n_{TOT,\,N}} = \alpha \qquad (4\text{-}6a)$$

$$n_{wall,N}^{eq} = \alpha\,(n_{inj} + n_{wall,\,N-1}^{eq}) \qquad (4\text{-}6b)$$

$$n_{wall,N}^{eq} = \alpha\, n_{inj} + \alpha\,(\alpha\,(n_{inj} + n_{wall,\,N-2}^{eq})) \qquad (4\text{-}6c)$$

Iterating *N* times this passage we obtain $n_{wall,N}^{eq} = (\alpha + \alpha^2 + \alpha^3 + \ldots + \alpha^N)\, n_{inj}$. The geometric series $\sum_{i=0}^{n-1} ax^i = a\left(\frac{1-x^n}{1-x}\right)$ can be written in the present case, giving eq. (4-7):

$$\frac{n_{wall,N}^{eq}}{n_{inj}} = \sum_{i=0}^{N} \alpha^i - 1 = \left(\frac{1-\alpha^{N+1}}{1-\alpha} - 1\right) = \frac{\alpha - \alpha^{N+1}}{(1-\alpha)} \qquad (4\text{-}7)$$

4.2.3 Continuous flow

When the channel is submitted to transient convection-diffusion conditions, the local form of the flux conservation of the bulk concentration *C* is given by eq. (4-8). The boundary

condition at the active wall is expressed by eq. (4-9), linking the analyte consumption flux at the active wall[19] to the time evolution of its adsorbed form:

$$\frac{\partial C}{\partial t} + \nabla \cdot (-D\nabla C + \boldsymbol{V}C) = 0 \qquad (4\text{-}8)$$

$$\frac{\partial \Gamma}{\partial t} = D\left(\frac{\partial C}{\partial y}\right)_{y=0} = k_{on} C(\Gamma_{max} - \Gamma) - k_{off}\Gamma \qquad (4\text{-}9)$$

where D is the analyte diffusion coefficient, k_{on} and k_{off} are the forward and reverse rates of adsorption (the thermodynamic constant being $K = k_{on} / k_{off}$) and $\boldsymbol{V}$ is the fluid velocity vector for the pressure driven flow (PDF). It is worth noting that the same kind of equations (but without convection for eq. (4-8), *i.e.* the Fick's law) is used for the simulation of the "stop-flow" process.

The evolution of C and Γ in the present FEM model is calculated by the following set of equations, which are applied to the 2-D geometry described in Fig. 4.1. Note that the boundary condition (4-9) is introduced in (4-8) as a consumption term assigned to the active wall, leading to eq. (4-10). To ensure that the adsorption term is only applied on the wall region for both eq. (4-10) and (4-11) and eq. (4-A1-3, A1-4, in Appendix 1), the surface concentration Γ', and the kinetic rates k_{on} and k_{off} are defined only at the wall surface; C is defined both in the bulk and at the wall. The second terms of eq. (4-10) and (4-11) equal zero in the bulk. The present model has been calibrated with previous numerical results[18, 20] for the Langmuir adsorption isotherm.[19]

$$\frac{\partial C}{\partial t} + \nabla \cdot \left(-D\nabla C + \boldsymbol{V}C\right) = -k_{on}\, C\left(\Gamma'_{max} - \Gamma'\right) + k_{off}\,\Gamma' \qquad (4\text{-}10)$$

$$\frac{\partial \Gamma'}{\partial t} + \nabla \cdot \left(-D_{wall}\nabla\Gamma'\right) = k_{on}\, C\left(\Gamma'_{max} - \Gamma'\right) - k_{off}\,\Gamma' \qquad (4\text{-}11)$$

The notation $\Gamma' = \Gamma/\delta$ has the same meaning than in chapter 3 (see paragraph *3.2.4*). D_{wall} is fixed at 4×10^{-11} $m^2 \cdot sec^{-1}$. It is verified that the diffusion coefficient D_{wall} of the wall insures a uniform concentration Γ' in the direction normal to the surface at any time during the calculation in a range of values from 4×10^{-10} to 4×10^{-12} $m^2 \cdot sec^{-1}$, due to the small thickness of the active layer. Simulations were performed to check that, within this range, variations don't occur in the bulk and surface concentration profiles.

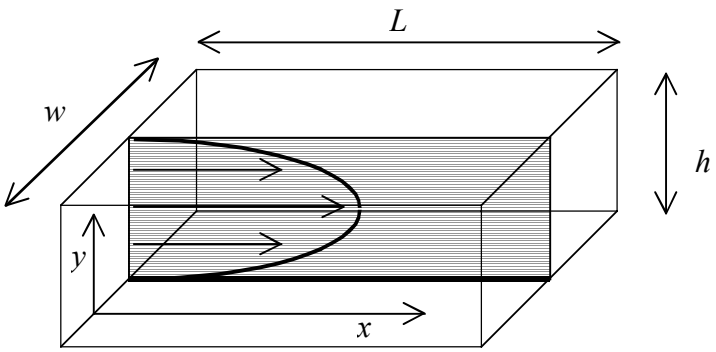

(a)

(b)

Figure 4.1. Scheme of the PET microchannel (not in scale): L = 4 cm (the detection point is fixed at 1.5 cm from the outlet), h = 50 μm and w = 200 μm. The channel is etched by laser ablation in a 100 μm high PET sheet. The shaded area inside the channel represents the 2D area used in the simulations (in this case L = 1mm), where the PDF flow velocity is used (further information can be found in SI). The adsorbing wall is on the bottom. **(b)** Mesh used for the simulations. The typical mesh size ranges from 2 μm for the active layer on the bottom to 10 μm on the top of the channel.

4.2.4 Numerical model and assumptions

In Appendix 1, eq. (4-8) and (4-9) are formulated using the Galerkin method. The finite element formulation is implemented in the software Flux-Expert™ (Astek Rhône-Alpes, France)[21], which is performed on a Silicon Graphics Octane 2 Unix workstation. The

calculations are performed in the 2-D geometry described on Fig. 4.1a. The typical mesh size ranges from 2 to 10 μm as shown in Fig. 4.1b. The active layer is 1 mesh thick. For the continuous flow, the initial conditions are $C = 0$ in the channel and $\Gamma = 0$ in the wall. For the zero-flow calculations (*i.e.* in the "stop-flow" process), the initial Γ value of each step n is equal to the value of Γ at equilibrium reached at the step n-1. The physical boundary condition (4-9) being introduced as a consumption term, the only numerical boundary conditions of the model are the Dirichlet conditions at the inlet ($C = C°$ for $x = 0$) and the Neumann homogeneous conditions at the external walls ($\partial C/\partial n = \partial \Gamma'/\partial n = 0$ for $y = -\delta$ or $y = h$ or $x = L$).

For the pressure driven (PDF) flow, a Poiseuille parabolic profile has been imposed, while for the electro-osmotic (EOF) flow, a uniform velocity profile has been imposed. For the "stop-flow" simulations, the velocity is set to zero in the entire domain. The typical Courant-Friederich-Levy (CFL) number $\boldsymbol{V}\cdot\Delta t/\Delta x$ is 0.5, as the velocity imposed is 100 μm·sec^{-1}, the characteristic time step Δt is 10^{-2} sec and the local cell Δx size is 2 μm. The following conditions are assumed: (i) – The solutions are sufficiently diluted so that the viscosity and the density of the fluid (assumed to be uniform) are not modified by concentration variations. (ii) – The channel walls are assumed to be smooth and the wall capillary forces are neglected in the eventual case of a liquid/air interface. (iii) – The width w of the channel is much larger than its height h so that the velocity gradient in the third dimension can be neglected (2D Cartesian assumption). (iv) – For the multiple "stop-flow" process, the flowing load of the solution is assumed to be instantaneous. (v) – Dead volume effects are neglected.

4.3 Experimental Section

The channel fabrication method by laser ablation and the characteristics of the confocal microscope are described in ref. [22] and chapter 2 respectively. The chip is inserted in a

Plexiglass holder allowing the infusion of the analyte solution through the inlet of the microchannel at a constant flow rate. The device is coupled to 2 syringe pumps (Kd Scientific; accuracy of the flow rate: ±1%) via PET microtubes (incubated 2 hours in a 5% BSA (SIGMA) in 0.01 M phosphate buffer solution (PBS) to avoid IgG adsorption) connected to the Plexiglass holder with a T junction. A 10^{-8} M solution of labelled antibody (Fluorolink Cy5 labelled antirabbit IgG, Amersham Pharmacia Biotech) in 0.01 M PBS was pumped in a 4 cm long microchannel (50 × 200 μm in cross section, as shown in Fig. 4.1a at a rate of 90 μL/h, corresponding to $\overline{V} = 2.5$ mm·sec^{-1} leading to the same residence time of 10 sec. as the experimental channel length is 25 mm (see Fig. 4.9). The protein solution was pumped for a time t_0 during which adsorption occurs. After this, the washing buffer (0.1% Tween-20 (SIGMA) in PBS) was pumped at the same inlet at a rate of 270 μL/h for 1 minute to insure an efficient washing of the unadsorbed proteins.[22] At this point, the fluorescence of adsorbed antibody on the channel wall was measured with the confocal microscope, giving the t_0 value of Fig. 4.8. The protein solution was then pumped in the same channel for an additional time t_1, followed by washing and measurement, giving the $t_0 + t_1$ value of Fig. 4.8, and so forth. No appreciable delay in stopping the flow was observed while switching from the infusion of the proteins to the washing buffer. The detection spot was fixed at 2.5 cm from the channel inlet. The mean value and its standard deviation were taken from 5 measurements and the minimum and maximum values from the measurements are used to bound the average values in Fig. 4.8.

The quantity of adsorbed antibody can be calculated from the fluorescence measurements with a calibration curve as done in chapter 3. However, to compare experiments and simulations, the fluorescence was normalised by the maximum value obtained at equilibrium. The linearisation of the Langmuir isotherm of adsorption[19] of this system led to know the Γ_{max} value for the IgG adsorption on the poly(ethylene terephthalate) (PET) microchannel. As

this value is largely lower than the one theoretically obtainable, multi-layer adsorption is not accounted for.

4.4 Results and Discussion

4.4.1 Stop-flow process

The "stop-flow" procedure is basically a sequence of adsorption equilibria alternated with a stepwise renewing of the bulk solution. It is illustrated by numerical simulations in Fig. 4.2, showing how the duration and the number of the sequential loadings required to reach Γ_{eq}^{theor} decreases with increasing ψ. When ψ (*i.e.* $KC°$) is multiplied by two orders of magnitude, the number of loads N to reach 99% of Γ_{eq}^{theor} is divided by 3 (from 3 to 1) and the time is divided by a factor of 30.

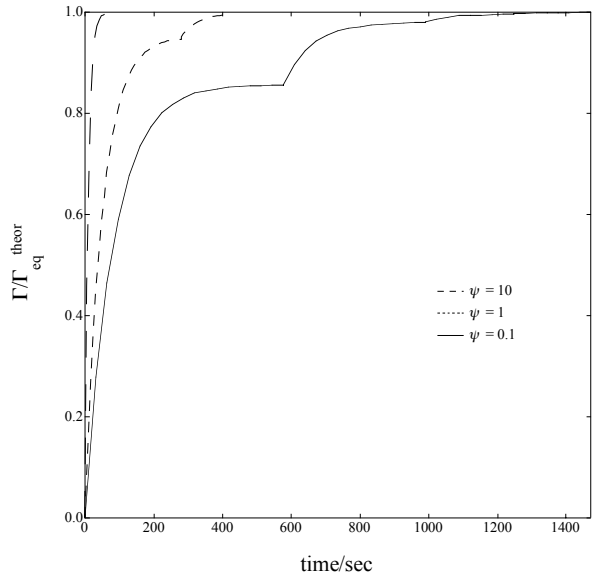

Figure 4.2. Time evolution of the coverage in a 50 μm high microchannel with sequential loadings of the analyte solution. The number of fillings and the time needed to attain Γ_{eq}^{theor} increases at lower concentrations. The parameters are $D = 4 \times 10^{-11}$ m^2·sec^{-1}, $\Gamma_{max} = 2 \times 10^{-8}$ mol·m^{-2}, $K = 10^4$ m^3·mol^{-1} ($k_{on} = 100$ m^3·mol^{-1}·sec^{-1}, $k_{off} = 0.01$ sec^{-1}; kinetics controlled adsorption). $C° = 10^{-5}$, 10^{-4}, 10^{-3} mol·m^{-3} for ψ = 0.1, 1, 10 respectively. $\Gamma_{eq}/\Gamma_{max}^{theor} = 9.1 \cdot 10^{-2}$, 0.5, and $9.9 \cdot 10^{-1}$ for ψ = 0.1, 1 and 10 respectively.

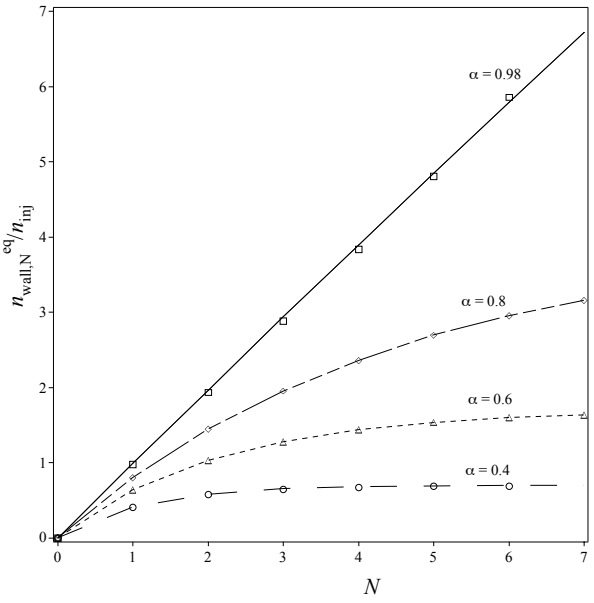

Figure 4.3. Representation of the number of moles adsorbed at equilibrium compared to the number of moles injected in the microchannel as a function of the number N of successive loads in a "stop-flow" procedure. The lines are calculated with eq. (7). The markers represent the results from simulations where at each step the ratio n_{wall}^{eq}/n_{inj} has been evaluated: the parameters are $D = 4 \times 10^{-11}$ $m^2 \cdot sec^{-1}$, $K = 2.5 \times 10^6$ $m^3 \cdot mol^{-1}$ ($k_{on} = 2.5 \times 10^8$ $m^3 \cdot mol^{-1} \cdot sec^{-1}$, $k_{off} = 100$ sec^{-1}: diffusion limited case), $C° = 4 \times 10^{-9}$ $mol \cdot m^{-3}$ ($\psi = 0.01$). α was varied changing Γ_{max}, which is equal to 5.6×10^{-11}, 1.4×10^{-10}, 3.2×10^{-10}, 3.9×10^{-9} $mol \cdot m^{-2}$ for $\alpha = 0.4$, 0.6, 0.8, 0.98 respectively.

For a low coverage situation ($\psi = 10^{-2}$), the analytical solution (4-7) is represented in Fig. 4.3 (lines) in function of N and compared to the simulation results (markers) at different α values. Any microsystem is characterised by an α value, which can be calculated by the second term of eq. (4-4), and which is inversely proportional to $1+\varphi$. The parameter α can be used to predict how many loads are necessary to reach Γ_{eq}^{theor} (*i.e.* to reach 93% of the plateaus of the plots in Fig. 4.3, for instance 3, 7, 20 loads are necessary respectively for $\alpha =$ 0.4, 0.6, 0.8 – this last not shown). The number of loads needed increases with α, (*i.e.* with Γ_{max}, K, and the surface-to-volume ratio $A \cdot Vol^{-1}$ of the microsystem). When $\alpha \rightarrow 1$ (*i.e.* the wall has a great adsorbing capacity), a great number of loads are needed: this is due to the high $\Gamma_{max}/C°$ ratio values resulting from the assumption of low coverages (*i.e.* low ψ).

Meanwhile, at high α values, the number of moles adsorbed at each load remains high for a wide range of steps, making the multiple "stop-flow" procedure effective.

4.4.2 Continuous flow

For the following simulations, the parameters used are shown in Tab. 4.1. The values of K and Γ_{max} are obtained from the study of the IgG antibodies adsorption on PET.[19] The diffusion coefficient D is that of IgG ($D = 4 \times 10^{-11}$ m^2·sec^{-1}) and the $C°$ value ($C° = 10^{-5}$ mol·m^{-3}, unless differently specified) corresponds to the one used in the experiments. A PDF flow is imposed, with a value of $\overline{V} = 100$ μm·sec^{-1}.[9]

parameters	flow simulations
D / m^2·sec^{-1}	4×10^{-11}
Γ_{max} / mol·m^{-2}	10^{-9}
$C°$/ mol·m^{-3}	10^{-5}
K / m^3·mol^{-1}	10^4
k_{on} / m^3·mol^{-1}·sec^{-1}	$10 – 10^6$
k_{off} / sec^{-1}	$10^{-3} – 100$

Table 4.1. Parameters for the flow simulations.

4.4.2.1 Diffusion limitation

The longitudinal distribution of the adsorbed species is represented in Fig. 4.4 (continuous lines) for different times of simulation. A diffusion limited adsorption (k_{off}=100 sec^{-1})[19] is illustrated, which can occur when an antigen reacts with the adsorbed antibody: this reaction also can be fitted by a Langmuir isotherm, the primary antibody representing the active site for the adsorbate.[23]

As the proteins advance in the channel, they are instantaneously adsorbed leading to a decreasing distribution of Γ along the wall. The entire wall is uniformly covered in 50 sec, corresponding to $5t_{res}$ ($t_{res}=L/\overline{V}$=10 sec.). Also the volume of sample solution used Vol_{sample} is

equal to 5 times the volume of the channel Vol_{channel}, as the following normalisation can be done:

$$\frac{t}{t_{\text{res}}} = \frac{Vol_{\text{sample}}}{Vol_{\text{channel}}} = N \qquad (4\text{-}12)$$

where t is the injection time and N corresponds to the number of channel volumes used.

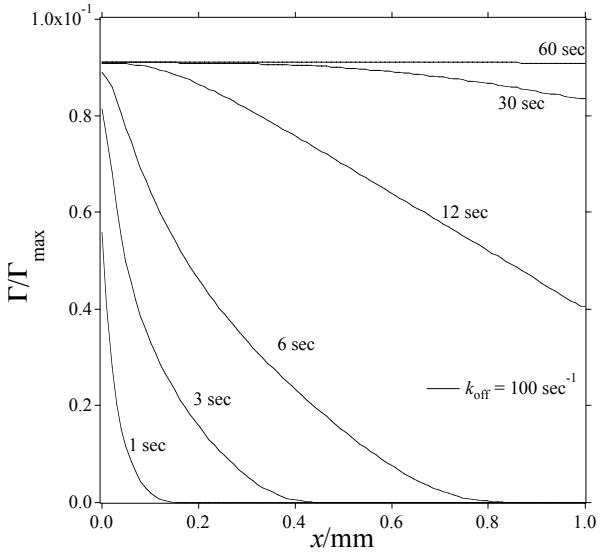

Figure 4.4. Simulation results of adsorption in a microchannel, under diffusion limitation (k_{off} = 100 sec^{-1}). The plots represent $\Gamma/\Gamma_{\text{max}}$ versus the distance from the beginning of the channel (x) at 1, 3, 6, 12, 30 and 60 sec. after the beginning of the injection. $D = 4 \times 10^{-11}$ $\text{m}^2\cdot\text{sec}^{-1}$, $\Gamma_{\text{max}} = 10^{-9}$ $\text{mol}\cdot\text{m}^{-2}$, $K = 10^4$ $\text{m}^3\cdot\text{mol}^{-1}$, $C° = 10^{-5}$ $\text{mol}\cdot\text{m}^{-3}$, $\overline{V} = 100$ $\mu\text{m}\cdot\text{sec}^{-1}$. As $\psi = 0.1$, $\Gamma_{\text{eq}}^{\text{theor}}/\Gamma_{\text{max}} = 9.1\times10^{-2}$.

To insure the uniformity of the coverage along the channel (as after 5 t_{res} in Fig. 4.5) the injection time must be long enough to allow the solute the time to reach the end of the channel and then to diffuse to the wall. This means that the condition $t \geq t_{\text{res}} + t_{\text{diff}}$ must be respected, t_{diff} representing the transversal diffusion time, whose order of magnitude is h^2/D. In this approach the longitudinal diffusion (along the channel) is neglected. Keeping into account the definitions of t_{res} and t_{diff} we finally obtain:

$$\frac{t}{t_{\text{res}}} \geq 1 + \left(\frac{h}{L}\right)^2 Pe_{\text{L}} \qquad (4\text{-}13)$$

where the Peclet number $Pe_L = \overline{V}\,L/D$. Eq. (4-13) yields the minimum experimental time necessary to achieve the uniformity of the coating, if the velocity of the flow is fixed by other experimental constraints.

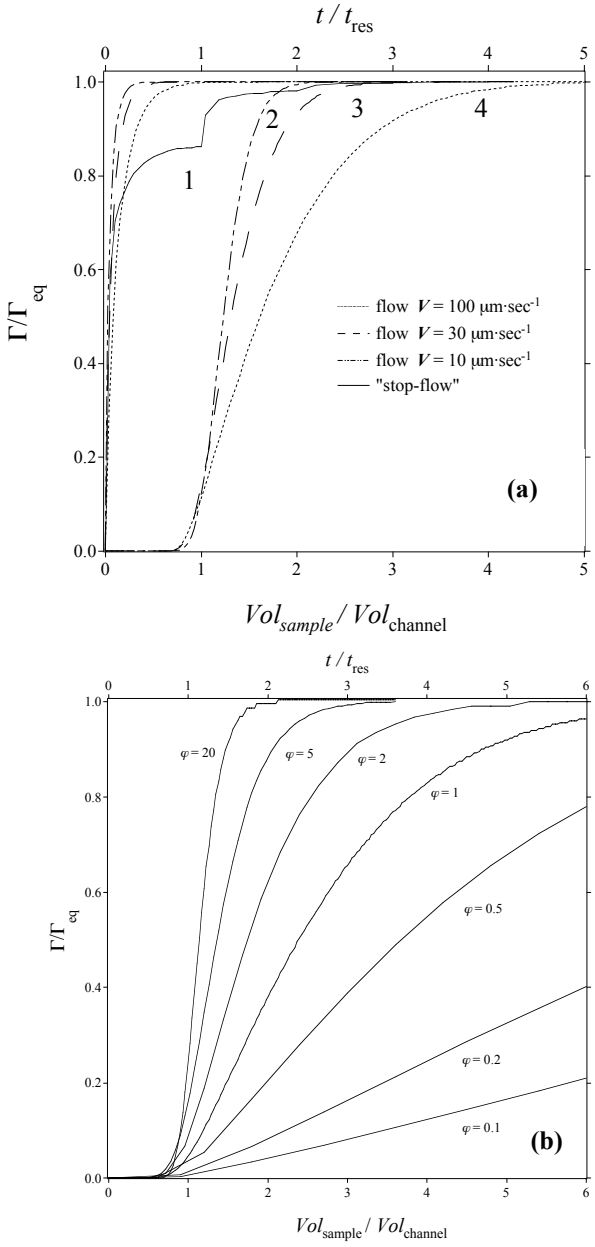

Figure 4.5. (a) Evolution of the coverage at the inlet (set of plot to the left) and at the outlet (set of plots to the right) of the microchannel wall in function of the volume of sample used, normalised by the volume of the channel ($Vol_{sample}/Vol_{channel}$). On top axis time is normalised by the residence time $L/\overline{V}$. The adsorption is diffusion controlled (k_{off} = 100 sec^{-1}). Flow velocities are $\overline{V}$ = 100 (dotted lines), 30 (dashed line), 10 μm·sec^{-1} (dashed and dotted line). The other parameters are those of Fig. 4.4. The numbers under the stop-flow plots represent the steps. **(b)** Evolution of the coverage at the end of the channel in function of the residence time for different φ values: Γ_{max} was changed, the other parameters are those of Fig. 4.5a. $\overline{V}$ = 30μm·sec^{-1} so that the case φ = 5 corresponds to the dashed lined plot in Fig. 4.5a.

To minimise the volume used (*i.e.* N in eq. (4-12)), we must increase t_{res}, reducing the fluid velocity. This is shown in Fig. 4.5a, where the impact of different fluid velocities on the coverage uniformity along the channel is illustrated. The growth of the coverage at the

beginning and at the end of the channel is reported versus the relative amount of sample used, and for the $\overline{V}$ values = 100, 30, 10 μm·sec^{-1}. It is illustrated how the difference between the coverages at the beginning and at the end of the channel (*i.e.* the non-uniformity of the coating) decreases when the velocity of the flow is reduced. As expected, the consumption of sample to reach the full coverage decreases when the velocity decreases: to obtain at the channel outlet 99% of the inlet coverage, 4.3, 2.5 and 1.9 $Vol_{channel}$ are respectively needed.

To choose the optimum velocity, one can fix a number N_{max} of Vol_{sample} that should not be exceeded. For example, if a waste not higher than that obtained with the "stop-flow" method is wanted, this number N_{max} can be fixed from Fig. 4.3, after calculating the coefficient α of the system. Introducing N_{max} in eq. (4-13) by the way of eq. (4-12), *i.e.* $t/t_{res} = N_{max}$, leads to:

$$\overline{V} \leq (N_{max} - 1)\frac{DL}{h^2} \qquad (4\text{-}14)$$

that grants for 99% of uniformity along the channel with the desired waste.[a] We can apply this methodology to the adsorption system represented in Fig. 4.5a, characterised by α = 0.167. From a plot like those in Fig. 4.3 or eq. (4-7), it is possible to calculate N_{max} = 3 (for 99% of the Γ_{eq}^{theor}) with the "stop-flow" procedure, which is also confirmed by the full line curve of Fig. 4.5a. From eq. (4-14), for N_{max} = 3, we obtain $\overline{V}$ = 32 μm·sec^{-1}: as just seen above, this flow velocity leads to employ 2.5 $Vol_{channel}$, respecting the desired sample consumption. More generally, choosing for instance N_{max} = 7 and 2 (the first not shown as it is out of scale) leads to impose $\overline{V}$ values ≤ 96 and 16 μm·sec^{-1} (in agreement with the velocity values used in Fig. 4.5a, for which 4.3, and 1.9 $Vol_{channel}$ are respectively used). The criterion (4-12) is then confirmed as a valid rule to have less or the same waste than with the "stop-flow" for a given degree of uniformity of the adsorbed analyte along the channel.

[a] The validity of eq. (4-14) has been verified for systems where $Pe_h = \overline{V}\,h/D \geq 10$ (to neglect the vertical diffusion).

It must be stated that the criterion (14) is valid when the microsystem is characterised by a φ value higher than 5 (as that of Fig. 4.5a). In Fig. 4.5b the coating evolution as a function of time at the end of the channel is shown in systems with different φ values and for a solution velocity $\overline{V}$ = 30 μm·sec^{-1}. At low φ values the adsorbing capacity of the system ($K\Gamma_{max}$) is very high and the residence time must be greater than the time to fill the adsorbing wall (which can be much longer than the t_{diff} to cross the channel). This leads to increasing the time to complete the adsorption by orders of magnitude (20 times the t_{res} for φ = 0.1, with t_{res} = 30 sec) and to reduce the velocity value given in eq. (4-14). However the φ values range in which eq. (4-14) holds covers the majority of the common experimental cases (adsorption on polymers without surface modifications).[24]

φ	α	N "stop-flow" analytic	N t_{res} simul; $\psi = 10^{-3}$	N t_{res} simul; $\psi = 0.1$
0.1	0.91	47	45	30
0.2	0.83	25	29	14
0.5	0.66	11	13	7
1	0.5	6	6	5
2	0.33	4	4	3
5	0.166	3	3	3

Table 4.2. Number of "stop-flow" steps needed to reach 99% of the plateau values in plots like those of Fig. 4.3 and number of t_{res} necessary to reach 99% of the full coverage with a continuous flow ($\overline{V}$ = 30 μm·sec^{-1}) in function of α and the corresponding φ (parameters of Fig. 4.5b). The values of t_{res} necessary with the flow mode are reported for $\psi = 10^{-3}$ (value at which the kinetics of adsorption is independent of concentration) and for ψ = 0.1: for this latter value, an agreement with the calculated values is found just for $\alpha < 0.5$.

A comparison between the number of "stop-flow" steps and the number of t_{res} to be used with the continuous flow to reach the full coverage (by simulations up to the equilibrium) is made in Tab. 4.2 for different φ values. The number of "stop-flow" steps is obtained with the analytical method that was compared with simulations results in Fig. 4.3. The two procedures are always comparable (at $\psi = 10^{-3}$ and $\overline{V}$ = 30 μm·sec^{-1}, which respects eq. (4-14)). The

difference with the simulations carried out with $\psi = 0.1$ is due to the fact that the analytical solution presumes the independence from $C°$ ($\psi << 1$).

In Appendix 2 the time to coat the surface is calculated in any φ condition. An analysis of the boundary layer developed during the adsorption in done.

4.4.2.2 Time comparison between continuous flow and "stop-flow" in a diffusion limited case

In order to see which procedure is faster, the continuous flow and the "stop-flow" are compared in Fig. 4.6 in function of the absolute time. With $\overline{V}$ = 100 μm·sec^{-1} the flow leads to the Γ_{eq}^{theor} value in about the same time as the "stop-flow" mode (60 sec. instead of 70 sec. for the 99% of Γ_{eq}^{theor}). With $\overline{V}$ = 30 μm·sec^{-1} the time to reach the full coverage is doubled (120 sec. for the 99% of Γ_{eq}^{theor}). As a consequence, for the same amount of analyte solution used, the "stop-flow" is faster than the continuous flow.

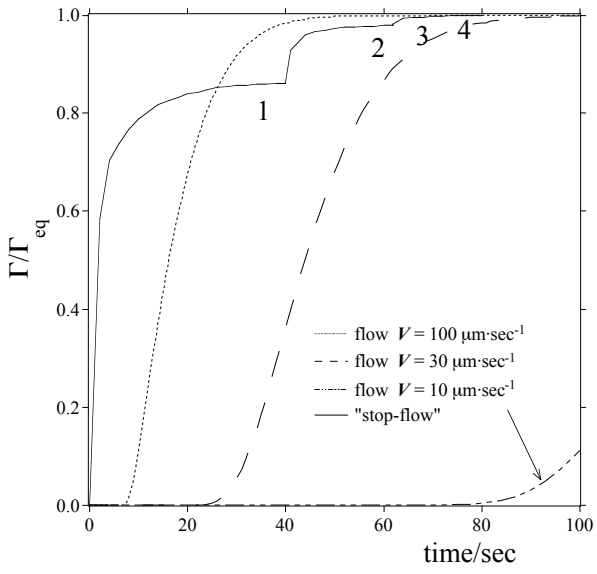

Figure 4.6. The results of Fig. 4.5a are here presented versus the absolute time. $D = 4 \times 10^{-11}$ m^2·sec^{-1}, $\Gamma_{max} = 10^{-9}$ mol·m^{-2}, $K = 10^4$ m^3·mol^{-1}, $C° = 10^{-5}$ mol·m^{-3}.

4.4.2.3 Kinetic limitation

In Fig. 4.7, the kinetic rates of adsorption are very low as during the antibody adsorption on the walls of a microtiter well (k_{off} values are 10^{-2} and 10^{-3} sec^{-1}, the last one corresponding to the kinetics of IgG adsorption on laser-ablated PET obtained in chapter 3). The theoretical coverage Γ_{eq}^{theor} (*i.e.* 9.1×10^{-2} Γ_{max}) is attained after a long time (100 minutes, not shown) through quasi-uniform concentration profiles (as under incubation). In fact, the time required for the adsorption ($t_{reac} = 1/k_{on} \cdot C° = 1000$ sec)[12] is much greater than the difference of exposition time of the wall to the analyte between the inlet and the outlet of the channel ($x/\overline{V}$=10 sec at the channel outlet for $\overline{V}$=100 μm·sec^{-1}).

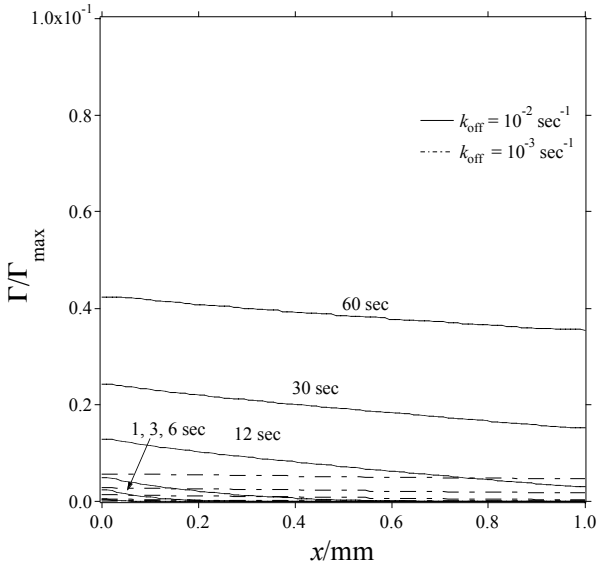

Figure 4.7. Simulation results of adsorption in a microchannel, under kinetic limitation (k_{off} = 10^{-2}, 10^{-3} sec^{-1}). The other parameters are those of Fig. 4.4a

Introducing a flowing continuous process doesn't bring any improvement to this adsorption step or would require a very low fluid velocity to let the residence time being greater than the reaction time. By analogy to the case of diffusion limitation, we can derive the following criterion for the velocity:

$$\overline{V} < (N_{max}\text{-}1)\, k_{on} C° L \qquad (4\text{-}15)$$

From this criterion, we can predict if a flow can be experimentally used or not, especially with low concentrations or slow kinetics.

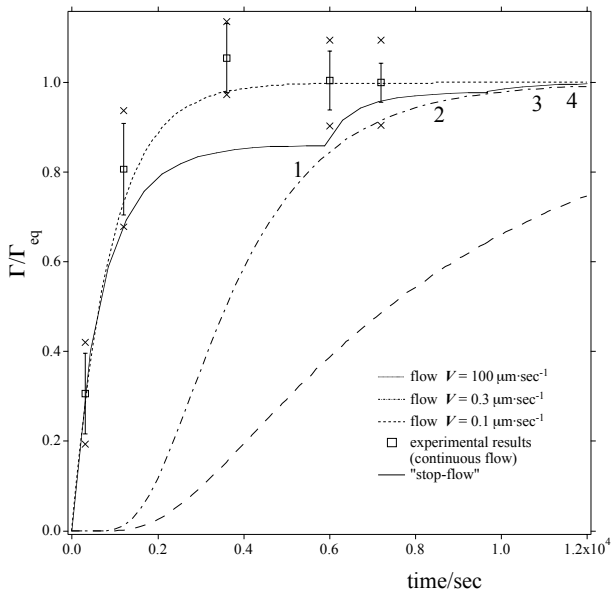

Figure 4.8. Time evolution of the adsorption at the end of the channel under continuous flow and stop-flow conditions for a kinetic controlled process (k_{off} = 10^{-3} sec^{-1}), $\overline{V}$ = 100 μm·sec^{-1}, 0.3 μm·sec^{-1} and 0.1 μm·sec^{-1}. The other parameters are those of Fig. 4.5. The markers (open squares) show the experimental results for IgG adsorption on PET microchannels. The minimum and the maximum values of the experiments (crosses) are used to bound the average values. A 10^{-8} M IgG solution in PBS was pumped in the PET channel with a pressure driven flow with a velocity of 90 μL·h^{-1} (corresponding to $\overline{V}$ = 2.5 mm·sec^{-1} leading to the same residence time of 10 sec. as the experimental channel length is 25 mm, as described in Fig. 4.8).

In Fig. 4.8, a comparison between the "stop-flow" and the continuous flow under kinetic limitation is shown in function of the absolute time, which is an important factor when the kinetic strongly limits the adsorption. Under "stop-flow" conditions, 4 sequential static loads are required to reach 99% of the theoretical Γ_{eq}^{theor} value, and a volume of 4 × 10^{-2} μL of protein solution is needed (*i.e.* 4 times the channel volume). For N_{max} = 4, a continuous flow velocity $\overline{V}$ = 0.3 μm·sec^{-1} is calculated from eq. (4-15), and then imposed in the simulations. A time t = 1.2 × 10^4 sec is needed to reach 99% of the theoretical coverage with this velocity

value. This leads to use of 3.6×10^{-2} μL, which is comparable with the one used in the "stop-flow". The criterion (4-15) is then confirmed as valid to minimise the sample.

The case presented here is an extreme one, as the kinetics of adsorption is very slow and requires flow velocity values that are difficult to achieve experimentally. On the other hand, for intermediate cases of kinetics, the criterion (4-15) can be helpful to determine if the continuous flow can be used or not.[b]

From an experimental point of view, controlling the flow in a microchannel is not always an easy task. The "stop-flow" approach alleviates the difficulty as the sample renewal can be done rapidly without controlling the flow rate, even if it implies a control of the sample volume to avoid exaggerated waste.

The experimental results of the IgG adsorption on PET under flow conditions are also shown (markers) in Fig. 4.8 to check the accordance with the simulations. High flow rates are important to minimize transport limitations and to allow an accurate estimation of the kinetic constants.[14] Therefore a pressure driven flow rate of 90 μL·h^{-1} was imposed (corresponding to the same residence time as for the simulation at $\overline{V}$ = 100 μm·sec^{-1}, with the couple (L, $\overline{V}$) = (25 mm, 2500 μm·sec^{-1}) instead of (1 mm, 100 μm·sec^{-1}). (See the validation in Fig. 4.9).

A good agreement is found between the simulation and the experimental results. The adsorption of IgG on PET is confirmed to be under kinetic control.[19] The experimental coverage values are slightly greater compared to the simulated ones. This can be due to the fact that immunosorption kinetics may be enhanced by the forced convection during the filling of the channel.[22]

4.4.2.4 Changing length of the channel

In order to check the valid range for extrapolating the results to longer channels, the effect of the channel length L has been studied for a constant residence time (by adapting the flow velocity proportionally to L). Fig. 4.9 shows the longitudinal distribution of Γ versus the dimensionless length of the channel x/L, for different velocities $\overline{V}$ and channel lengths L.

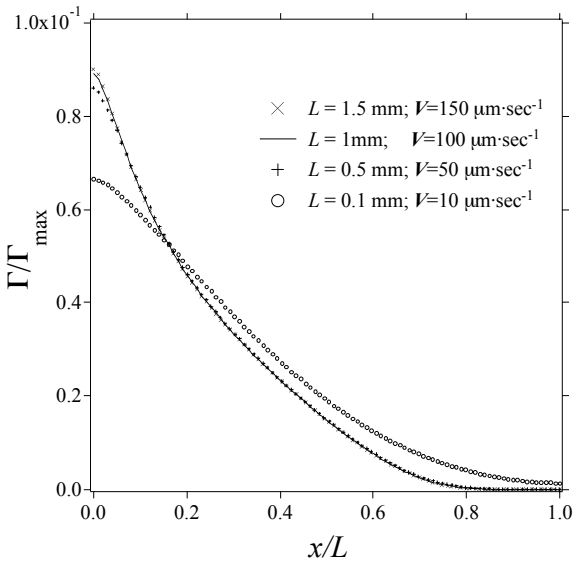

Figure 4.9. Comparison of results for different couples ($\overline{V}$, L) (*i.e.* flow velocity and channel length). Plots represent Γ/Γ_{max} in function of the normalised distance x/L. $\overline{V}$ = 150, 100, 50 and 10 μm·sec^{-1} for L = 1.5, 1, 0.5, 0.1 mm respectively. $D = 4 \times 10^{-11}$ m^2·sec^{-1}. The other parameters are those of Fig. 4.5.

For velocity values below 10 μm·sec^{-1}, the Γ distribution is different, due to the competitive contribution of the longitudinal diffusion ($D/\delta_{diff} \sim 10$ μm·sec^{-1} corresponds to $\delta_{diff} \sim 4.2$ μm, where δ_{diff} is the typical 1-D diffusion length). For $\overline{V}$ values higher than 50 μm·sec^{-1}, the plots are similar, whatever the couple (L, $\overline{V}$). Consequently, the results of the previous

[b] The validity of eq. (4-15) depends on the Pe_L (here Pe_L = 7.5) as the typical length for the longitudinal diffusion $\delta \cong L$ (the solute diffusion length here is $\delta = (\pi Dt)^{1/2} \cong 1$ mm). Consequently, for δ = 1mm, $V_{diff} = D/\delta$ = 0.04 μm·sec^{-1}, confirming that it can be neglected.

figures can be applied, for example, to 1 cm channels (instead of 1mm) with ten times higher flow rates (*i.e.* 1 mm·sec^{-1}), *i.e.* conditions that are generally used experimentally.

The results of this work can then be extrapolated to longer channels, provided that the residence time is respected (*e.g.* the results previously obtained for the couple (L, $\overline{V}$) = (1 mm, 100 μm·sec^{-1}) also apply to results obtained in a system where (L, $\overline{V}$) = (1 cm, 1 mm·sec^{-1})).

4.5 Conclusions

Due to the solution depletion occurring during static adsorption in microsystems, two methods to renew the solution are studied in order to obtain the best possible coverage of the active adsorbing wall: the "stop-flow" and the continuous flow processes. To do this, a finite element model has been developed considering the transient convection diffusion of one species in solution coupled to the adsorption kinetics on the active surface.

As the multiple "stop-flow" procedure is done with sequential static loads, an analytical expression is provided by which the number of necessary loads can be predicted (in a situation far from full coverage, *i.e.* low concentrated solutions). Finally, a good agreement is found with the simulations.

For the continuous flow process, the effects on the coating of different adsorption kinetic rates have been studied. In diffusion limited cases, uniform adsorption coverages are obtained for flow velocity values $\overline{V} < (N_{max}-1)DL/h^2$, where N_{max} corresponds to the number of volumes of sample that we want to use. N_{max} can be fixed equal to the number of steps for the "stop-flow" mode, giving the velocity range for which the continuous flow is competitive with the "stop-flow" in terms of sample waste (for 99% of coating uniformity along the channel). Similarly, under kinetic control, the value $\overline{V} = (N_{max}-1)k_{on}C°L$ ensures the theoretical coverage using the same amount of sample as the "stop-flow". These comparisons

underline the interest of the “stop-flow”, especially with slow kinetics, low concentrations or short channels implying too slow velocity values for the continuous flow.

Measurement of IgG adsorption in a PET microchannel under flow conditions has been performed, showing a good agreement with the simulation results and confirming confocal microscopy as a useful and simple tool to investigate adsorption in microsystems. The results obtained with this model can be extended to longer channels, after scaling the velocity flow.

Appendix 4.1

The global forms of the local equations (4-10) and (4-11) (and also of (3-9) and (3-10)) are here described using the Galerkin formulation (multiplication by a projective function α_p and integration on the domain of study, Ω), where $C_i = C$, Γ' for $i = 1, 2$ respectively. By setting $\boldsymbol{V} = 0$ we obtain the set of equations used in static conditions. The term A_i corresponds to the 2nd terms of eq. (4-10) and (4-11) defined only in the wall region.

$$\iint_{\Omega} \alpha_p \left[\frac{\partial C_i}{\partial t} + \nabla \cdot \left(-D_i \nabla C_i + \boldsymbol{V} C_i \right) - A_i \right] d\Omega = 0 \qquad (4\text{-A1-1})$$

The convection term is derived by taking into account the continuity equation $\nabla \cdot \boldsymbol{V} = 0$. By decomposing the product between α_p and the divergence, the second order derivative of (4-A1-1) (divergence of the gradient) becomes:

$$\alpha_p \nabla \cdot (-D_i \nabla C_i) = \nabla \cdot (-\alpha_p D_i \nabla C_i) + D_i \nabla \alpha_p \cdot \nabla C_i \qquad (4\text{-A1-2})$$

Applying (4-A1-2) in (4-A1-1) and using the Ostrogradsky theorem, the divergence term is rejected at the external boundaries of the domain where it expresses the diffusion boundary condition of each species (here equal to zero, *i.e.* no diffusion flux at the external boundaries of the domain).

$$\iint_{\Omega} \left[\alpha_p \frac{\partial C}{\partial t} + D \nabla \alpha_p \cdot \nabla C + \alpha_p \boldsymbol{V} \cdot \nabla C + \alpha_p k_{on} \Gamma'_{max} C - \alpha_p k_{on} \Gamma' C - k_{off} \Gamma' \right] d\Omega = 0 \qquad (4\text{-A1-3})$$

$$\iint_{\Omega} \left[\alpha_p \frac{\partial \Gamma'}{\partial t} + D_{wall} \nabla \alpha_p \cdot \nabla \Gamma' - \alpha_p k_{on} \Gamma'_{max} C + \alpha_p k_{on} \Gamma' C + k_{off} \Gamma' \right] d\Omega = 0 \qquad (4\text{-A1-4})$$

Appendix 4.2

The time to coat the surface can be calculated saying that the flux of solute to the wall must be equal to the coverage value, once the equilibrium is reached, that is:

$$D\frac{\partial C}{\partial n}(L\cdot w) = n_{\text{wall,eq}} = \frac{\partial \Gamma}{\partial t}(L\cdot w) \qquad \text{(4-A2-1)}$$

where L and w are the length and the width of the surface area, and $n_{\text{wall,eq}}$ is the number of moles adsorbed at equilibrium. Keeping into account the definitions of $\Gamma_{eq}^{\ theor}$, and approximating $\frac{\partial C}{\partial n}$ with $\frac{C^\circ}{\delta_d(h)}$ we obtain:

$$t_{\text{coat}} = \frac{\Gamma_{\max}}{DC^\circ}\frac{\psi}{1+\psi}\delta_d(h) \qquad \text{(4-A2-2)}$$

and as $\varphi = h/K\Gamma_{\max}$ the following expression is obtained:

$$t_{\text{coat}} = \frac{1}{\varphi(1+\psi)}\frac{h}{D}\delta_d(h) \qquad \text{(4-A2-3)}$$

The choice of the boundary layer thickness $\delta_d(h)$ is of crucial importance. When the flow velocity is so slow that the depleted solute is not renewed fast enough from the incoming solution, the vertical gradient of C extends to the upper channel wall. This is shown in Fig. 4-A2-1, illustrating the concentration normalised by C° in function of the height h, at different x distances from the channel inlet, after t = 1 t_{res}. The velocity of the flow is set at $\overline{V}$ = 10 μm · sec^{-1}. After $t = 1t_{res}$ the solution is already depleted at 50 μm from the inlet, so that at the top of the channel the concentration $C < C^\circ$. In this case $\delta_d(h)$ can be chosen equal to the height of the channel h. Fig. 4.A2-2 illustrates the boundary layer thicknesses as in Fig. 4.A2-1 but for a velocity $\overline{V}$ = 30 μm·sec^{-1}. As the velocity flow is higher than in Fig. 4.A2-1 and the solution is more actively renovated, the C° value extends to the top of the channel up to x = 100 μm from the inlet. In this case, when the velocity is fast the equation for the boundary layer thickness can be written more classically as:[25]

$$\delta_d(h) = \frac{1}{0.339\left(\frac{\overline{V}}{\nu L}\right)^{\frac{1}{2}}\left(\frac{\nu}{D}\right)^{\frac{1}{3}}}$$

A comparison of the time to reach the equilibrium as calculated with eq. (4-A2-3) and the time from simulations is done in Tab. 4.A2-1, showing a quasi-direct proportionality up to $\varphi = 1$.

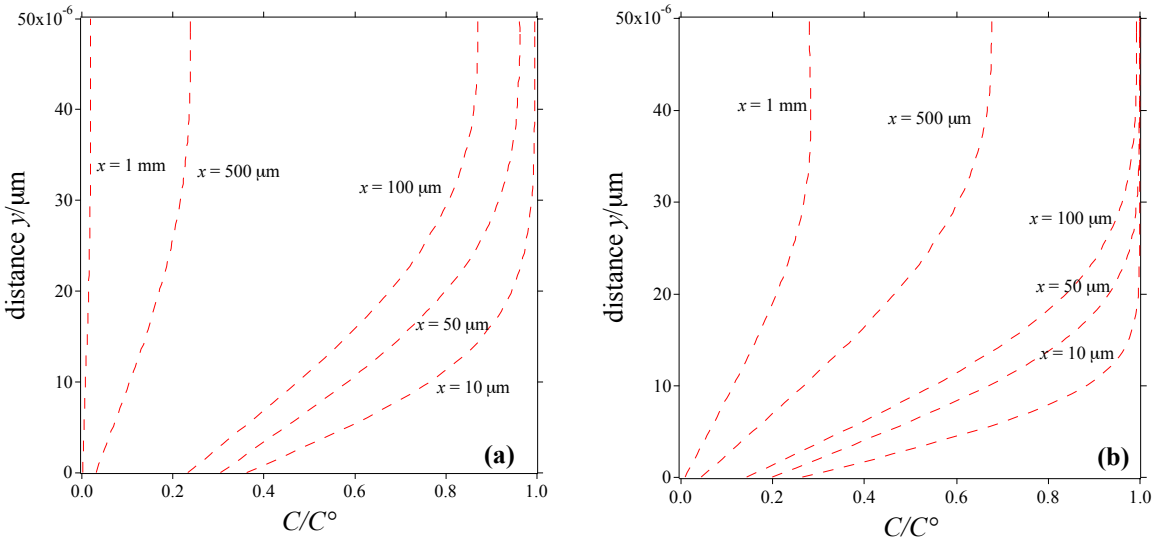

Figure 4.A2-1. Normalised concentration profiles in a channel of height y at different positions (x) from the inlet, at $t = 1t_{res}$. **(a)** $\overline{V} = 10$ µm · sec^{-1}: the solution is already depleted at 50 µm from the inlet, so that at the top of the channel the concentration $C < C°$. **(b)** $\overline{V} = 30$ µm · sec^{-1}: as the velocity allows for renewing the solution, the depletion begins occur after about 500 µm from the inlet.

Eq. (4-A2-3) has been tried on different cases of velocity, diffusion coefficients and concentrations, failing for diffusion coefficients greater than 10^{-10} m^2·sec^{-1}, for which the expression of $\delta_d(h)$ must change.

φ	$t_{coat\ calc}$/sec	$t_{coat\ simul}$/sec	t_{simul}/t_{calc}
0.1	6800	960	0.14
0.2	3401	470	0.14
0.5	1359	230	0.17
1	680	150	0.22
2	341	108	0.32
5	136	84	0.62

Table 4.A2-1. Times to reach the equilibrium as calculated with eq. (4-A2-3) and times from simulations. The ratio of the two is shown in the fourth column.

References:

(1) Eteshola, E.; Balberg, M. *Biomedical Microdevices* **2004**, *6*, 7-9.

(2) Malmstadt, N.; Hoffman, A. S.; Stayton, P. S. *Lab on a Chip* **2004**, *4*, 412-415.

(3) Sato, K.; Tokeshi, M.; Odake, T.; Kimura, H.; Ooi, T.; Nakao, M.; Kitamori, T. *Analytical Chemistry* **2000**, *72*, 1144-1147.

(4) Yakovleva, J.; Davidsson, R.; Lobanova, A.; Bengtsson, M.; Eremin, S.; Laurell, T.; Emneus, J. *Analytical Chemistry* **2002**, *74*, 2994-3004.

(5) Galanina, O. E.; Mecklenburg, M.; Nifantiev, N. E.; Pazynina, G. V.; Bovin, N. V. *Lab on a Chip* **2003**, *3*, 260-265.

(6) Dodge, A.; Fluri, K.; Verpoorte, E.; de Rooij, N. F. *Analytical Chemistry* **2001**, *73*, 3400-3409.

(7) Karlsson, R.; Michaelsson, A.; Mattsson, L. *Journal of Immunological Methods* **1991**, *145*, 229-240.

(8) Glaser, R. W. *Journal of Immunological Methods* **1993**, *160*, 141-142.

(9) Yarmush, M. L.; Patankar, D. B.; Yarmush, D. M. *Molecular Immunology* **1996**, *33*, 1203-1214.

(10) Myszka, D. G.; Morton, T. A.; Doyle, M. L.; Chaiken, I. M. *Biophysical Chemistry* **1997**, *64*, 127-137.

(11) Myszka, D. G.; He, X.; Dembo, M.; Morton, T. A.; Goldstein, B. *Biophysical Journal* **1998**, *75*, 583-594.

(12) Mason, T.; Pineda, A. R.; Wofsy, C.; Goldstein, B. *Mathematical Biosciences* **1999**, *159*, 123-144.

(13) Wofsy, C.; Goldstein, B. *Biophysical Journal* **2002**, *82*, 1743-1755.

(14) Sikavitsas, V.; Nitsche, J. M.; Mountziaris, T. J. *Biotechnology Progress* **2002**, *18*, 885-897.

(15) Pham, P., Institut National Polytechnique de Grenoble, Grenoble, 2001.

(16) Filippov, L. K.; Filippova, N. L. *Journal of Colloid and Interface Science* **1997**, *189*, 1-16.

(17) Paces, M.; Kosek, J.; Marek, M.; Tallarek, U.; Seidel-Morgenstern, A. *Electrophoresis* **2003**, *24*, 380-389.

(18) Reinmuth, W. H. *Journal of Physical Chemistry* **1961**, *65*, 473-&.

(19) Lionello, A.; Josserand, J.; Jensen, H.; Girault, H. H. *Lab on a Chip* **2005**, *5*, 254-260.

(20) Delahay, P.; Trachtenberg, I. *Journal of the American Chemical Society* **1957**, *79*, 2355-2362.

(21) Rhône-Alpes, A.: 1 place du Verseau, 38130 Echirolles, France.

(22) Rossier, J. S.; Gokulrangan, G.; Girault, H. H.; Svojanovsky, S.; Wilson, G. S. *Langmuir* **2000**, *16*, 8489-8494.

(23) Horstmann, B. J.; Chase, H. A. *Chemical Engineering Research & Design* **1989**, *67*, 243-254.

(24) Rossier, J. S.; Girault, H. H. *Lab on a Chip* **2001**, *1*, 153-157.

(25) Coeuret, F., Storck, A. *Eléments de génie électrochimique*; Lavoisier: Paris, 1984.

Antibodies Adsorption on TiO_2 Modified Microchannels

5.1 Introduction

Microimmunoassays have been developed[1, 2] in order to overcome the slow response obtained with normally formatted assays. Actually, the microdimensions shorten the path of the primary antibody to the system walls, diffusion being the limiting factor of a classical heterogeneous immunoassay.[3]

Due to the nL volumes, detection in such systems represents a challenge; normally it is done exploiting fluorescent molecules generated by enzymes linked to the secondary antibodies[4,5] or attaching a chromophore to one of the molecules of the immunotest. Enhancing the surface concentration of primary antibodies results in an increase of the antigen concentration revealed by the test. Many efforts have been made to reach this aim, as well as to strengthen the interaction between the polymer surface and the primary antibody, in order to decrease losses of primary antibodies during the frequent washing steps which occur while performing an immunoassay. In the case of biosensors, high levels of protein loading are important in order to increase the sensitivity and the signal-to-noise ratio of the analysis. This goal can be achieved by modifying the adsorptive surface by silanisation[6] and by coatings of biomolecules [7] or inorganic materials such as TiO_2.[8]

Proteins adsorption on TiO_2 is a subject of much interest in particular with regard to biocompatibility. Titanium spontaneously generates a layer of oxides (primarily TiO_2)[9] when exposed to air or aqueous media. When a titanium medical device comes in contact with blood, proteins interact with the TiO_2 layer whose properties are more similar to those of a ceramic than to those of a metal. Several studies have been performed on the interaction between albumin, one of the most abundant protein in human body, and TiO_2.[10,11] Some studies have also been conducted with fibrinogen, and prothrombin.[9] Surprisingly, however,

in a survey of the literature, only few studies have been found on the interaction between TiO_2 and IgG antibodies.[9,12]

Adsorption of proteins is a challenging process to study, since it involves different factors,[13] such as protein-protein and protein-surface interactions, and also structural changes within the proteins. It is widely recognised, though, that the strongest driving factor is the interaction between the surface and the protein. Due to the fact that during the adsorption a large number of water molecules are released from the protein and the surface, proteins bind preferentially to hydrophobic surfaces. After the adsorption, the binding can be reinforced by conformational changes in the protein.

In this work, the adsorption of antibodies in TiO_2 coated PET microchannels is studied. Titania is used under the form of nanomaterials in order to increase the active surface of the microsystem. The adsorption is studied as a function of the pH and the ionic strength in order to characterise the interaction of IgGs and TiO_2. The detection is done with the confocal microscope described in chapter 2.

5.2 Experimental Section

5.2.1 Reagents and Solutions

TiO_2 nanowhiskers and nanorods were purchased from Catalysts and Chemicals (Japan). TiO_2 nanowhiskers are in anatase crystalline form, with a point of zero charge around 6. The active surface area of this material is 400 $m^2 \cdot g^{-1}$. TiO_2 nanorods are amorphous: this material exhibits the interesting feature of a negative surface charge from pH 3 to pH 9.5 obtained by doping (supplier information). Nanorods with 320 and 400 $m^2 \cdot g^{-1}$ active surfaces area have been used. All other chemicals (NaCl, HCl, NaOH) were of analytical grade and water was purified with the Millipore Milli-Q system. A 1mg·mL^{-1} (6.67×10^{-6} M) solution of labelled antibody (Fluorolink Cy5 labelled antirabbit IgG, Amersham Pharmacia Biotech) was

prepared in water. From this, further solutions were obtained by serial dilutions with PBS (SIGMA). PBS solution has the following composition: 0.01 M phosphate, 0.0027 M KCl and 0.15 M NaCl. The washing buffer is made of a 0.1% Tween-20 (SIGMA) solution in PBS. IgG solutions at different pH values were prepared by adjusting the initial pH to the desired value by small amounts of 0.1 M NaOH and 0.1 M HCl. IgG solutions 0.001 M NaCl and at different pH were also prepared. IgG are supplied as a lyophilised solid in PBS (0.01 M Potassium Phosphate, 0.15 M NaCl), pH 7.4, to be reconstituted with 1.0 mL of deionised water. After reconstitution the 6.67 M ($1 mg \cdot mL^{-1}$) IgG solution was diluted 100 times with 0.1 M and 0.001 M NaCl solutions at different pH. The final pH was measured with a Tacussel pH-meter.

5.2.2 Microchannel Fabrication

The microchannel fabrication[14, 15] has already been described in the previous chapters. To enhance the binding between the TiO_2 particles and the PET by exposing COOH groups, the microchannels were oxidized before lamination.[16] First, they were washed with distilled water, methanol and hexane, and then dried. PET-CO_2 surfaces were prepared by introducing the clean, non-laminated microchannels into 1 M NaOH for 16 min at 60 °C. They were subsequently rinsed with 0.1 M HCl, distilled water and hexane, dried at reduced pressure and then laminated.

The coating of the microchannels with the titania particles was performed by filling the channels with a solution of 1% of particles in methanol, and letting the adsorption take place all night in a Petri box saturated in methanol to avoid evaporation. Before the adsorption of IgG antibodies, the channels were rinsed three times with water.

IgG adsorption on TiO_2 coated microchips was observed as previously described.

5.2.3 Kinetic Isotherms and Steady-State Isotherms

The kinetics of adsorption was measured as described in chapter 3. The isotherms of

adsorption were recorded measuring the Γ_{eq} values, *i.e.* the adsorption values reached at equilibrium as a function of the bulk concentration $C°$ as described in chapter 3 (paragraphs 3.3 and *3.4.5*) in Theory and Experimental. The equilibrium values of adsorption in this chapter are experimental and obtained in microsystems. In previous chapters the notation $\Gamma_{eq}^{\mu syst}$ was used: for simplicity Γ_{eq} will be used in this chapter. The equilibrium adsorption as a function of different ionic strengths and pH values was also measured.

5.2.4 SEM pictures

The pictures were taken with a Philips XL 30 FEG electron microscope after delaminating the microchannels of the PE/PET sheet. To observe the PET channels with SEM avoiding the accumulation of charges on the surface, they were previously coated with a gold layer almost 20 nm thick.

5.3 Results and Discussion

5.3.1 Aspect of the Microchannel Surface

All the results for the two different kinds of TiO_2 nanomaterials, with different active surface area, are similar. We are reporting now only the results from the anatase 400 $m^2 \cdot g^{-1}$ rods.

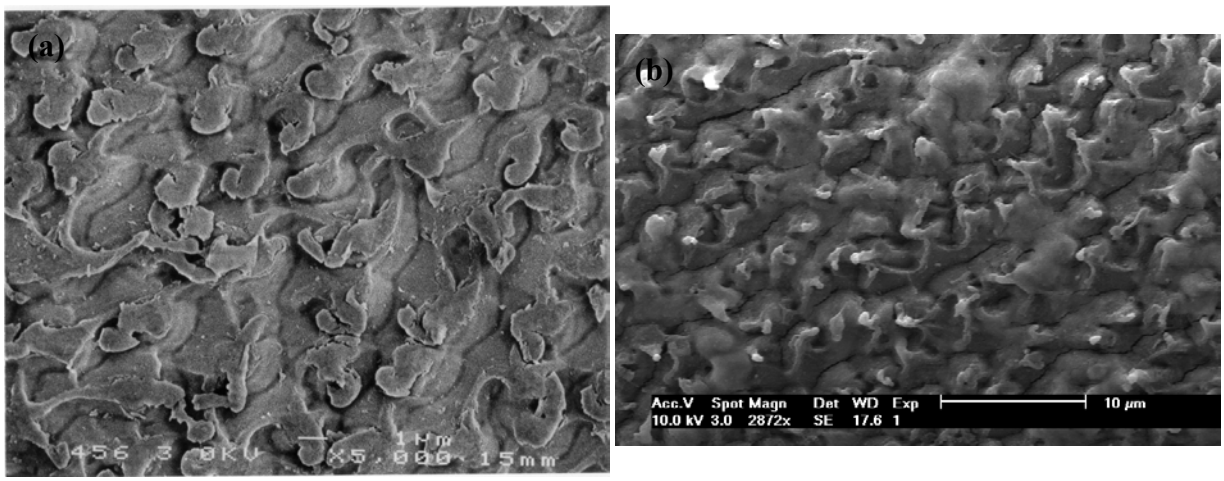

Figure 5.1. SEM images: Laser ablated PET before **(a)** and after **(b)** oxidation. In Tab. 5.1 it can be observed that the initial number of active sites Γ_{max} increases from bare PET to oxidized PET. The SEM picture of the laser ablated PET shows that the surface presents a lot of "hills". These formations, smoothed during the polishing, are enhanced with the NaOH oxidation: this can also explain the slight increase in Γ_{max}.

In Fig. 5.1a, the SEM pictures of the surface of a laser ablated PET microchannel are shown and compared with the ablated surface after treatment with NaOH in Fig. 5.1b.

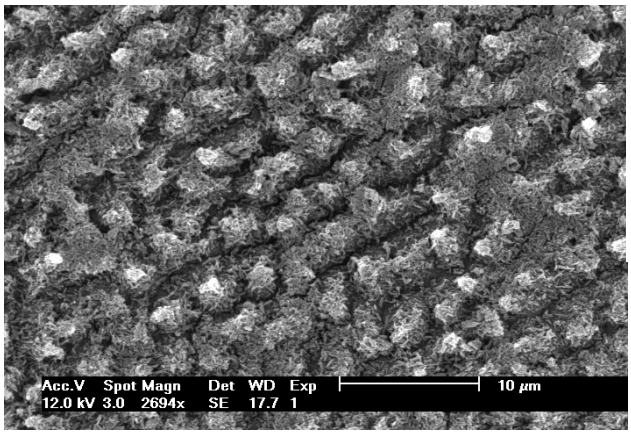

Figure 5.2. SEM image of TiO2 nanorods coated microchannel. The active surface is further enhanced by fixing the nanorods and nanowhiskers on the surface.

The microstructures present on the surface, resembling hills about 1 μm high, must not be confused with redeposited debris. They are the result of differential etching between amorphous and crystalline regions of the polymer exposed to short pulses of the ultraviolet radiation of the excimer laser at fluences higher than 100 $mJ \cdot cm^{-2}$. The hills correspond to the more crystalline material and the valleys to the amorphous one. The aspect of the surface of a TiO_2 amorphous nanorods coated microchannel is shown in Fig. 5.2. The aspect of TiO_2 anatase nanowhiskers coated microchannel is similar to the one coated with nanorods. A compact and stable layer of particles is obtained: “hills” and “valleys” are entirely covered with TiO_2 nanoparticles, which are firmly attached to the surface. A confocal microscope scan through the microchannel shows a uniform distribution of adsorbed IgGs on these supports.

5.3.2 Kinetics of adsorption

The adsorption kinetics of IgG on the three surfaces (oxidised PET, anatase TiO_2 and amorphous TiO_2) is represented in Fig. 5.3. The kinetics of adsorption on laser ablated, non-oxidised PET (bare PET) at $C° = 6.67 \times 10^{-7}$ M is also reported (full rhombi, dashed lines) in order to illustrate the improvement obtained after surface modifications. On all the three

phases the adsorption is faster at higher concentrations, as foreseen by the Langmuir kinetic (eq. 3-2).

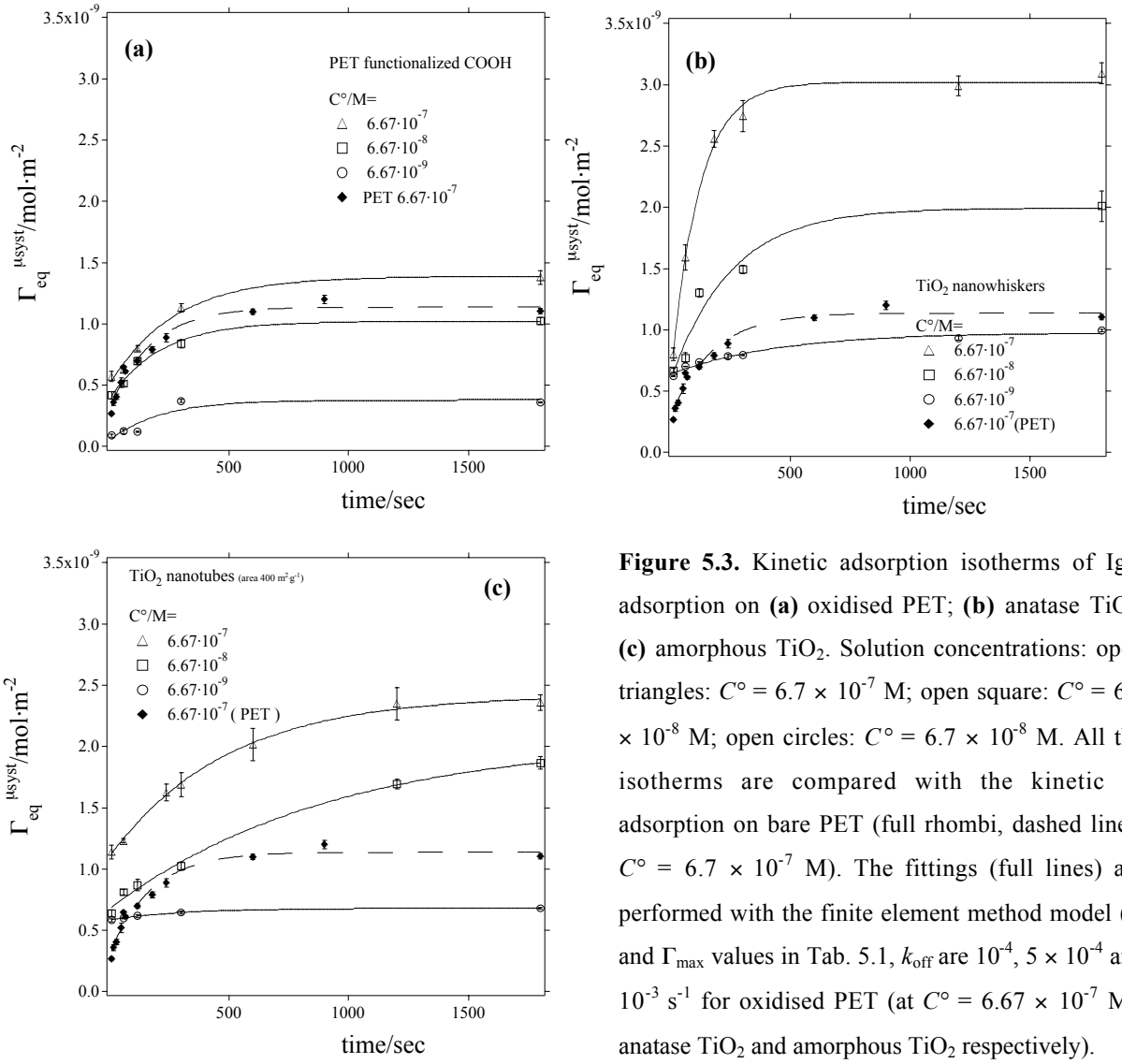

Figure 5.3. Kinetic adsorption isotherms of IgG adsorption on **(a)** oxidised PET; **(b)** anatase TiO_2; **(c)** amorphous TiO_2. Solution concentrations: open triangles: $C°$ = 6.7 × 10^{-7} M; open square: $C°$ = 6.7 × 10^{-8} M; open circles: $C°$ = 6.7 × 10^{-8} M. All the isotherms are compared with the kinetic of adsorption on bare PET (full rhombi, dashed lines: $C°$ = 6.7 × 10^{-7} M). The fittings (full lines) are performed with the finite element method model (K and Γ_{max} values in Tab. 5.1, k_{off} are 10^{-4}, 5 × 10^{-4} and 10^{-3} s^{-1} for oxidised PET (at $C°$ = 6.67 × 10^{-7} M), anatase TiO_2 and amorphous TiO_2 respectively).

The transport of the proteins to the surface can be limited both by the diffusion in solution and by the adsorption kinetics onto the surface. To investigate the mass transfer characteristics, the isotherm kinetics in Fig. 5.3 have been fitted with the help of the finite element model already described in the chapters 3 and 4. The values of K and Γ_{max} used in the simulations are those of Tab. 5.1, obtained by linearisation of the steady-state adsorption isotherms as explained in chapter 3, and below in this chapter.

The value of k_{off} that has been taken for the diffusion limitation regime is 100 s^{-1} (the difference with the case of 10 s^{-1} is 2% of that at 10 s): for this value all the proteins arriving to the surface are immediately adsorbed. For higher values of k_{off} (keeping constant the value of $K = k_{on}/ k_{off}$) no change in the adsorption kinetics is observed, proving that the mechanism is diffusion controlled.

support	$K \cdot 10^4/m^3 \cdot mol^{-1}$	$k_{on}/ m^3 \cdot mol^{-1} \cdot sec^{-1}$	k_{off}/ sec^{-1}	$\Gamma_{max} \cdot 10^{-9}/mol \cdot m^{-2}$
bare PET	0.80	8	10^{-3}	1.30
oxidized PET	8.43	8.43	10^{-4}	1.38
amorphous TiO_2 (320 $m^2 \cdot g^{-1}$)	3.58	35.8	10^{-3}	2.20
amorphous TiO_2 (400 $m^2 \cdot g^{-1}$)	2.59	25.9	10^{-3}	2.40
anatase TiO_2	4.88	24.4	5×10^{-4}	3.13

Table 5.1. Values of K and Γ_{max} as obtained from the linearised isotherms of Fig. 5.4.

The two rates k_{on} and k_{off} were lowered from the diffusion limiting values to fit the experimental curve of Fig. 5.3. The values found for k_{off} are 10^{-4} for oxidised PET (at $C° = 6.67 \times 10^{-7}$ M), 5×10^{-4} for anatase TiO_2 and 10^{-3} s^{-1} for amorphous TiO_2. This means that the adsorption processes on all the surfaces are limited by the actual adsorption, as already observed for IgG adsorption on PET.[17]

This is a non-negligible factor when envisaging microimmunoassays. Microdimensions, in fact, allow speeding up the test when the adsorption of the capture antibody or the subsequent immunoreaction is fast. If the adsorption is slow, the experimental times or the time-to-response of a test can be considerably higher than expected. Adsorption of low concentrated

solutes, for instance, can take more than 30 minutes to complete, as shown, for instance in the adsorption kinetics on amorphous TiO_2 in Fig. 5.3c.

5.3.2.1 Oxidised PET

Adsorption on oxidised PET presents a higher value for K than on bare PET.[17] This is due to the value of k_{off} which is one order of magnitude lower on oxidised PET, while the k_{on} values are almost the same for the two surfaces. To evaluate the influence of the surface charge of the two surfaces on the k_{on} value, this quantity was calculated (using the values from electroosmotic flow measurements from A. Ros' Ph D dissertation[18]). The surface charge is $\delta = \zeta\kappa\varepsilon$, where κ is the Debye-Hückel parameter, ε is the dielectric constant of the solvent and ζ is the zeta potential of the surface ($\zeta = \mu_{eo}\eta/\varepsilon$ where μ_{eo} is the electroosmotic mobility of the solvent per unit field strength which is accessible experimentally, and η is the viscosity of the solvent).

The values for δ and ζ for the two surfaces are reported in Tab. 5.2.

surface	$\mu_{eo}\cdot10^{-8}/m^2\cdot V^{-1}\cdot sec^{-1}$	ζ/mV	$\delta/C\cdot m^{-2}$
bare PET	5.4	78	0.067
oxidised PET	5.0	72	0.062

Table 5.2. Comparison of the calculated δ and ζ for bare and oxidised PET. κ = 12.4 m^{-1} from Grossman, [19] ε = 6.95×10^{-10} $C^2\cdot J^{-1}\cdot m^{-1}$ for water,[20] η = 0.001 $N\cdot s\cdot m^{-2}$.[20] μ_{eo} are from Ros.[18]

It can be observed that the surface charge is almost equivalent for the two cases: the proteins approaching the two different surfaces experience an equivalent electrostatic force, which confirms the k_{on} values, close one another. What helps in stabilising the attachment in the oxidised surface (and in the increasing of K) are, more likely, electrostatic forces and covalent bonds. Carboxylic groups are indicated for covalent binding of IgG on polymers: all these binding possibilities concur to increase the thermodynamic constant of adsorption.

Furthermore, for oxidised PET, we found a lower kinetic rate at higher concentrations, k_{on} and k_{off} being equal to 0.84 $m^3 \cdot mol^{-1} \cdot sec^{-1}$ and 10^{-3} s^{-1}, respectively, for $C° = 6.67 \times 10^{-8}$ M and 6.67×10^{-9} M instead of 10^{-4} s^{-1} for $C° = 6.67 \times 10^{-7}$ M. This is peculiar because, normally, the same set of adsorption and desorption rates are used to simulate all the adsorption kinetics, varying just in $C°$ values. This behaviour has already been explained:[21] at larger surface coverages obtained at higher concentrations, the arriving proteins require a specific orientation to avoid the repulsion from the molecules already attached and, at the same time, to adsorb onto the surface, inhibiting the adsorption.

5.3.2.2 Anatase TiO_2

On this substrate a fast and strong adsorption occurs: Γ_{eq}, reached in 10 minutes, has a threefold value with respect to the one on bare PET. Anatase TiO_2 has a point of zero charge at pH 6, and the pI of the antibodies falls in a range between 6 and 8. When a protein pI matches the point of zero charge of a surface, the classical mechanism for non-specific adsorption is followed. In the isoelectric region IgG antibodies are in their compact structure.[22] The antibodies classically adsorbed in compact form through the Fc part at pH 7.4 hinder less the adsorption of further molecules, as would happen with unfolded forms.[23]

IgG surface binding on other surfaces than TiO_2[24] was established to be due to hydrophobic forces in cooperation with electrostatic forces. In the pH range 6.0 – 7.0, the predominant TiO_2 anatase surface groups are $Ti_2{=}O^-$, TiO^- and Ti-OH.[11] Possible electrostatic reactions are the ion-dipole interactions between the monocoordinated surface –OH groups and the aminium groups in the protein.

The fact that electrostatic forces can be claimed in the IgG/PET and IgG/TiO_2 systems is proved by the lower adsorption values found at relatively high salt concentration (see below), where the electrostatic charges of the surface and the proteins are shielded.

5.3.2.3 Amorphous TiO_2 (Electrostatic Adverse Conditions)

IgG adsorption on amorphous TiO_2 coated microchannels is quite fast, since only 20 minutes are necessary for reaching the surface concentration at equilibrium Γ_{eq} at the highest bulk concentration. It can be observed that the amorphous TiO_2 coating enhances twofold the adsorption, in comparison to the bare PET isotherm. This kind of amorphous TiO_2 nanorods have been chosen because the negative surface charge exhibited allows for exploring the importance of electrostatic interaction for IgG adsorption on TiO_2. For the negative surface of amorphous TiO_2, the predominant $Ti_2=O^-$ and $Ti\text{-}O^-$ forms are postulated, so that the same mechanism of adsorption described for the phases above can be envisaged.

5.3.3 Steady State Isotherms

The steady state adsorption isotherms of these systems are shown in Fig. 5.4 (see eq. 3-4).

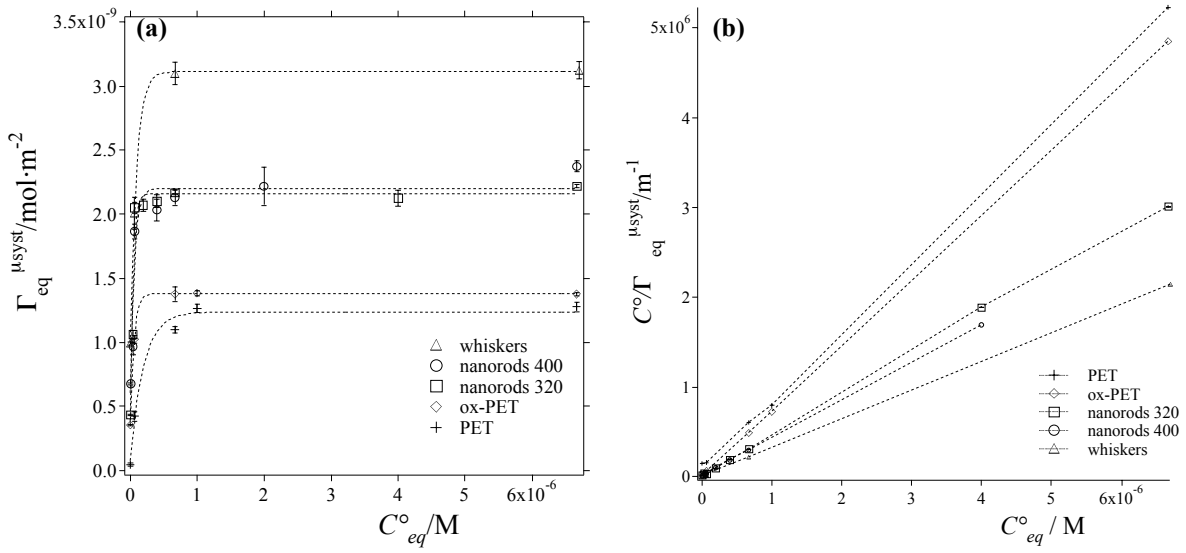

Figure 5.4. (a) Steady state isotherms of adsorption of all the systems: open triangles: TiO_2 anatase nanowhiskers, open circles: amorphous TiO_2 nanorods (active surface 400 $m^2 \cdot g^{-1}$); open squares: amorphous TiO_2 nanorods (active surface 320 $m^2 \cdot g^{-1}$); open rhombi: oxidised PET; crosses: laser ablated PET. **(b)** Linearised isotherms.

The isotherms develop a well established plateau at around 1 μM concentration. Since it has been proven by many studies[10] that proteins adsorption reaches its maximum at a pH close to

the isoelectric point (pI) of the proteins, the isotherms have been recorded at the pH of the buffer solution, *i.e.* at pH 7.4. The pI of polyclonal antibodies should span from 6 to 8.

The steady state isotherms can be linearised (see Fig. 5.4b) reporting $C°/\Gamma_{eq}$ versus $C°$, as described in eq. 3-15. This gives the initial number of active sites Γ_{max} and the thermodynamic constant K as the values of the slope and the y-intercept respectively, which are reported in Tab. 5.1. The lowest values of K and Γ_{max} are those of bare PET, and they are higher for treated surfaces.

The steady state isotherms of Fig. 5.4 show greater adsorption values on modified surfaces compared to those on bare PET. The amount of adsorbed protein at low degrees of surface coverage relative to the amount in solution is a measure of the protein affinity for the surface. Thus, when this amount reaches a constant value at low concentrations in solution, it indicates that a high affinity isotherm is operating. Low affinity isotherms are characterised by a slight increase of the adsorbed protein (as on bare PET, where electrostatic repulsion is active).

5.3.4 Adsorption on PET at Different Salt Concentrations

In Fig. 5.5a, Γ_{eq} as a function of pH for different ionic strengths is plotted for oxidized PET. This is possible because the fluorescence properties of Cy5 don't change with the pH, as shown in Fig. 5.5b. The maximum of the adsorption on PET occurs at a concentration of 10^{-3} M NaCl, at pH 5, while at a higher concentration of 0.1 M NaCl the concentration is almost independent from the pH (the surface concentration Γ_{eq} spans from 0.6 to 0.9 × 10^{-9} mol·m^{-2}) and is drastically reduced of about one half.

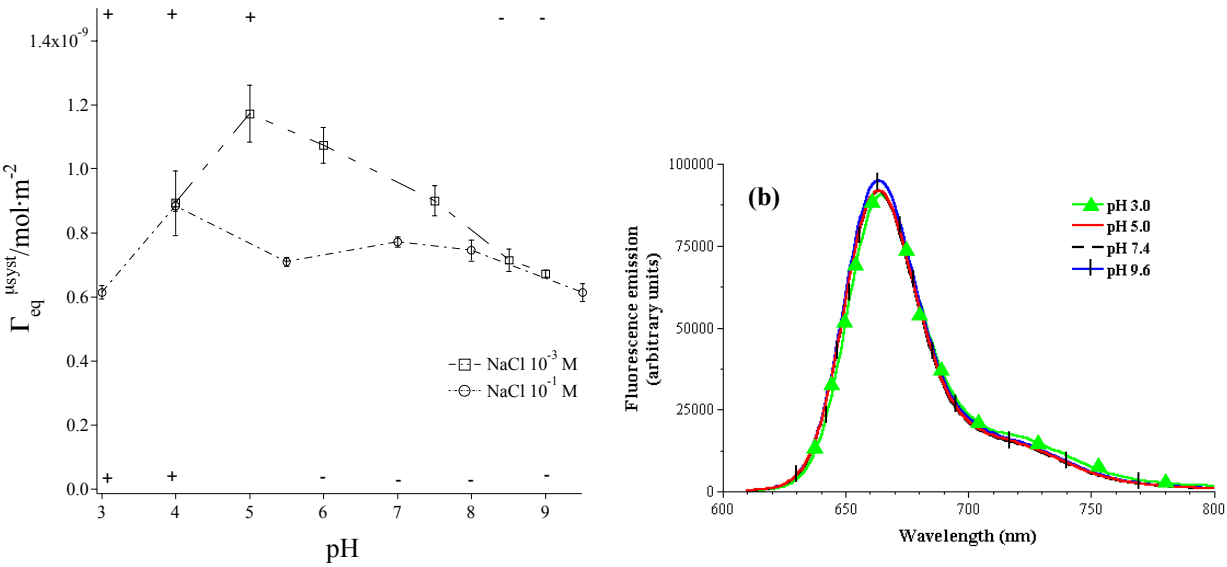

Figure 5.5. (a - left) Dependence on pH of the plateau values of the adsorption on oxidised PET at an ionic strength of 10^{-3} M (open squares, dashed and continuous line) and 0.1 M NaCl (open circles, dotted and continuous line). The overall charge of the proteins is indicated on top and that of the surface at the bottom of the graph. (**b)** Emission spectra of Cy5 dye at pH 3, 5, 7.4 and 9.6.

This is probably the result of increased screening of the PET surface charge by the sodium ions, weakening the strength of the electrostatic interaction with the protein. This again reflects the electrostatic nature of the protein/PET interaction.

The electrolyte concentration or ionic strength can also influence the protein size and the intermolecular interactions, which can be analysed by a model that considers protein molecules as rigid spherical particles.[11] The thickness of the double layer surrounding each rigid sphere depends on the ionic strength of the buffer: it is equal to $1/\kappa$, where κ, the Debye-Hückel parameter is given by the Debye equation:

$$\kappa = \left(\frac{e^2 1000 N_{\mathrm{Av}} \sum_i z_i^2 c_i}{\varepsilon k_{\mathrm{B}} T} \right)^{1/2} \qquad (5\text{-}1)$$

Here e is the elementary charge, N_{Av} the Avogadro constant, z_i and c_i the number of charges and the concentration of the electrolytes of the buffer, k_{B} and T the Boltzmann constant and the temperature.

It can be inferred from this expression that an increase in the ion concentration (NaCl in our case) could produce a decrease in the effective size of the rigid particle due to compactness of the electrical double layer around the protein molecule. The dimensions of the double layer depending on the ionic strength are reported in Table 5.3.

solution [a]	ionic strength[b]/M	κ^{-1}/nm	A_{eff}/nm^2 [c]	A_κ/nm^2	A_{eff}/A_κ
PBS pH 7.4	9.64×10^{-2}	0.98	1268	143	9
NaCl 0.1 M	5×10^{-2}	1.35	2371	161	15
NaCl 10^{-3} M	5×10^{-4}	13.6	1380	1380	1

Table 5.3. Double layer thickness and area values for the rigid particle model under different experimental conditions. [a] Buffer as indicated in text. [b] Ionic strength = $\frac{1}{2}\sum_i z_i^2 c_i$. [c] The values of A_{eff} are taken from eq. (5-3) suing the values obtained experimentally in Fig. 5.5 and 5.6.

The diminution of the double layer extension, and thus the distance at which the repulsive forces between particles become considerable, should allow a greater accumulation of the protein molecules at the surface with the increase in ionic strength. This behaviour is not observed here.

Giacomelli et al.[10] have proposed an approximate calculation of the molecular area taking into account the contribution of the double layer and the effect of the ions in solution. Thus, it is possible to define A_κ as the area of the rigid particles as follows:

$$A_\kappa = \left(\sqrt{A_{str}} + \frac{2}{\kappa}\right)^2 \qquad (5\text{-}2)$$

where A_{str}, the structural protein area, is here taken as 100 nm^2. The results calculated according to eq. (5-2) are also shown in Table 5.3. It can be observed that at high ionic strength the A_κ values are remarkably lower than the areas calculated with the experimental data in Fig. 5.5 and 5.6 (see also below in Fig. 5.7a). This fact (together with the fact that we

observe a greater accumulation of proteins with the decrease in ionic strength) suggests that the particles do not behave as rigid ones. We can conclude that the electrostatic repulsion between molecules is negligible, that the effect of the double layer should be minimum and, therefore, that the electrostatic interactions between the proteins and the surface are the main responsible for the behaviour described in Fig. 5.5.

The calculation for the area is valid at low ionic strengths, suggesting that electrostatic repulsion between molecules plays a role in the final surface concentration (even if a correlation with higher ionic strength situations is not allowed).

5.3.5 Adsorption as a Function of pH

The dependence of Γ_{eq} on pH is plotted in Fig. 5.6. The overall charge of the protein at different pH is indicated on the top of the graph, and the charge on the surface on the bottom. The dashed lines and the triangles show the value of fluorescence measured after desorption: the results are discussed below. For oxidized PET, important values of adsorption occur between the pH values of 5 and 7.4 (and the maximum is reached at 7.4). The Γ_{eq} equilibrium values are lower on both sides of the pI and this decrease is stronger at the basic side of the curve. On anatase TiO_2, the maximum is at pH 7.4. On amorphous TiO_2, the maximum value occurs at pH 9.5.

Both on oxidised PET and anatase TiO_2 (Fig. 5.6a, b) IgG adsorption is consistent with the trend normally observed[10] for electrostatic adsorption: the maximum adsorbed amount is found at the pI of the protein. Adsorption on anatase TiO_2 at pH 7.4 exhibits the most important value registered in this work. On the contrary, at pH values far from the pI, the general electrostatic repulsion between the ionised groups on the surface of a protein causes unfolding of a protein which has a substantial net charge: in fact, such repulsions would be minimised in the unfolded state.

The Γ_{eq} values are lower at both sides of the pI because of the electrostatic repulsion between the protein and the sorbent or between already adsorbed proteins and the newly arriving proteins. For the adsorption in acidic conditions, it must be noticed that a domain in the Fc part of the antibody (the C_H3 domain shown in Fig. 1-3) unfolds at pH 4,[25] leading to oligomerisation of the two chains of the domain. This exposes hydrophobic groups, such as the lateral chain of tryptophan, which are normally buried in the protein, rendering them available for bonding.

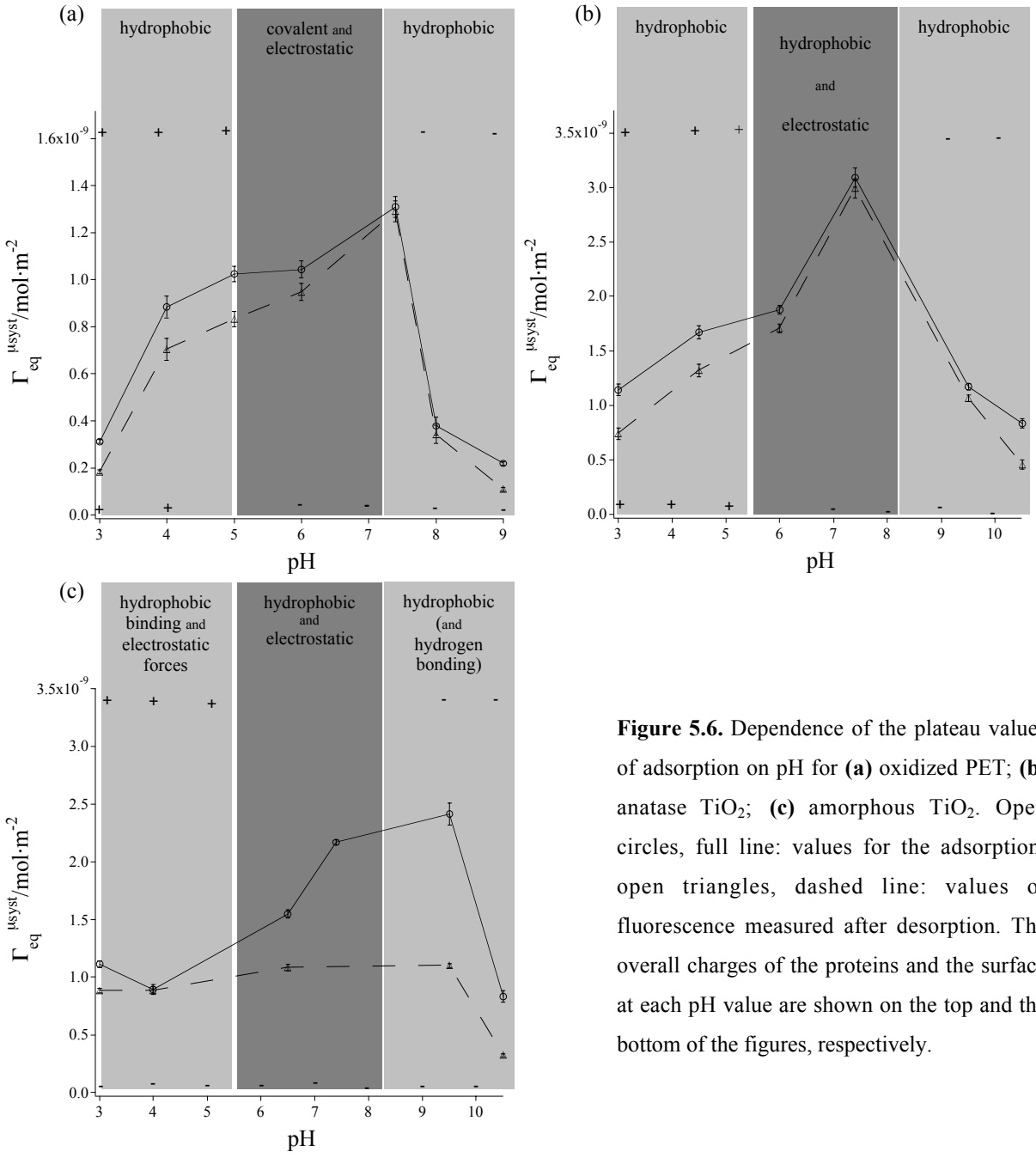

Figure 5.6. Dependence of the plateau values of adsorption on pH for **(a)** oxidized PET; **(b)** anatase TiO_2; **(c)** amorphous TiO_2. Open circles, full line: values for the adsorption; open triangles, dashed line: values of fluorescence measured after desorption. The overall charges of the proteins and the surface at each pH value are shown on the top and the bottom of the figures, respectively.

The binding of proteins to surfaces carrying the same overall charge of the sorbent surface (Fig. 5.6c) as on amorphous TiO_2 at high pH is due to the fact that proteins always have patches of the opposite charge on their surface, that allow localised binding. Binding under adverse electrostatic conditions would also indicate that hydrophobic interactions are able to overcome electrostatic repulsion: Gibbs et al.[26] says that IgG binds best at slightly basic pH, which exposes hydrophobic groups due to partial denaturation. Hydrogen bridges between TiO_2 and the aminium group can occur with the following schemes:[11] Ti-OH + $R\text{-}NH_3^+ \rightarrow$ Ti-OH$\cdots$:NH_2-R + H^+ and $Ti\text{-}O^-$ + $R\text{-}NH_2$: + $H_2O \rightarrow$ Ti-OH$\cdots$:NH_2-R + OH^-, as proved below by results from desorption.

5.3.6 Strength of the Adsorption

Reversibility of the adsorption process was tested by filling with water the microchannel that had reached the equilibrium of adsorption and waiting overnight for desorption to take place. After washing, the amount of antibodies still adsorbed was measured with the confocal microscope. The results plotted in Fig. 5.6 with the dashed lines show that desorption is stronger for the antibodies that adsorbed in basic and very acid conditions, while it is less pronounced when the adsorption occurred at the pI. After adsorption, proteins normally undergo structural modifications that stabilise their interaction with the surface. Usually, not more than 10% of desorption is found on most systems, and almost no desorption is found on oxidised PET and TiO_2 anatase.

Dramatic desorption is measured from amorphous TiO_2 corroborating that part of the bonding can occur through hydrogen bonding and electrostatic forces.[27] The fact that not all the antibodies are removed from the surface suggests that two types of proteins, weakly and strongly bound, are present.[10] This was also suggested in other works. At pH 4, almost no desorption was found. Structural rearrangements are registered at acid pH in

immunoglobulins G; as explained above, the interior of the protein is exposed, increasing the number of available active sites of the molecule to the TiO_2.

Data are also shown in Fig. 5.7 as a function of the effective area[10], A_{eff}, giving the area, in nm, which is available for each antibody molecule defined as:

$$A_{eff} = \frac{10^{18}}{\Gamma_{max} N_{AV}} \qquad \text{eq. (5-3)}$$

where 10^{18} is a conversion factor and N_{Av} is the Avogadro constant. Γ_{max} is expressed in $mol \cdot m^{-2}$. It is possible to calculate the maximum number of IgGs adsorbable on a surface with the area of the molecule, 10 nm×10 nm, leading to a value of Γ_{max} of 10^{-9} $mol \cdot m^{-2}$. In other words, we will obtain a surface density of 1 molecule per 100 nm^2.

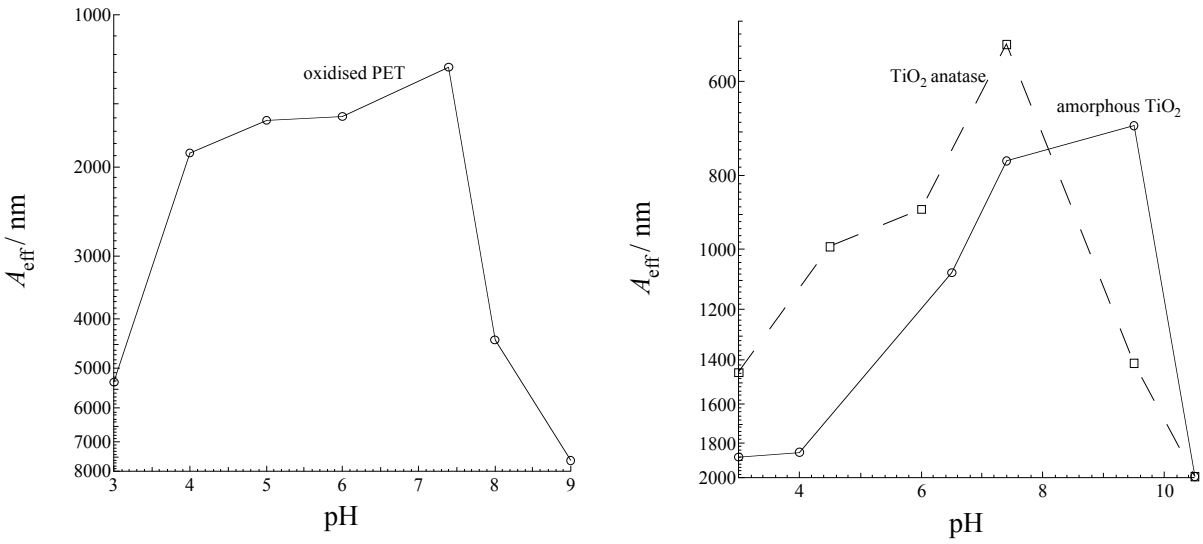

Figure 5.7. Values of the effective area A_{eff} in nm as a function of pH for oxidised PET **(a - left)** and TiO_2 **(b - right)** nanoparticles.

To obtain this maximum value, the surface must be very active like after silanisation followed by activation with glutaraldehyde (as for AFM experiments and, in this work, as explained in paragraphs *2.2.2* and *2.3.2*). If the adsorption occurs on a surface that does not

grant a packed monolayer, each molecule is allowed an area bigger than the theoretical 100 nm^2.

In the case of PET, a decrease of active sites concentration was measured[17] in the ratio of 1/10 $mol \cdot m^{-2}$. This is equivalent to saying that each molecule has an available surface area of 1000 nm^2, or that the surface density is of 1/1000 nm^2, which is what happens at pH 7.4. Since the conditions for adsorption are less favourable at acid and basic pH, the effective area is 7000 nm^2 (*i.e.* the surface density reaches 1/7000 nm^2) at pH 9. The maximum of the adsorption on anatase TiO_2 is at pH 7.4, where a value of the available area for adsorption is about 500 nm^2.

The same plot is reported for IgG adsorption on amorphous TiO_2. As the adsorption is enhanced, the area available for each molecule decreases: here, the area is about 750 nm^2 at the maximum, *i.e.* at pH 9.5. The adsorption decreases at acid and basic pH. In other studies,[10, 11] A_{eff} represents the molecular area, changing with structural modifications that depend on the adsorption environment. In this work, A_{eff} has more to do with the concept of area still available for adsorption.

5.3.7 Competition between PBS and IgG for the adsorption on TiO_2

The experiments leading to the results of Fig. 5.5 are carried out in PBS, which is the environment in which antibodies maintain their structure, granting for a good antigen-antibody interaction. It has been shown that the phosphate ion binds to TiO_2 as a bidentate ligand[28] and that saturated coverage is reached at a phosphate concentration of less than 0.01 M.[12] It has been demonstrated that phosphate can displace the weakly bound IgG antibodies at concentrations higher than 0.01 M and at pH 7. This can explain the lower value found for adsorption at pH 7 than at pH 10 on amorphous TiO_2.

To check the importance of the competition between phosphate ions and IgGs for the active sites on amorphous TiO_2, the adsorption was carried out in 0.001 M PBS and 10^{-3} M NaCl. In

Fig. 5.8 (full line), showing the values of Γ_{eq} as a function of pH, it can be observed that in these conditions the maximum is again shifted to pH 7.4, and that the plot as a function of pH exhibits the classic features. The antibodies that could not adsorb on the TiO_2 because of the high phosphate concentration (as shown in Fig. 5.5c) can now bind, though weakly. The values after desorption (dashed line) are also plotted: important values of desorption are registered in all the pH range, stressing again the importance of hydrogen bonding at high pH and of electrostatic forces at low pH in this phase.

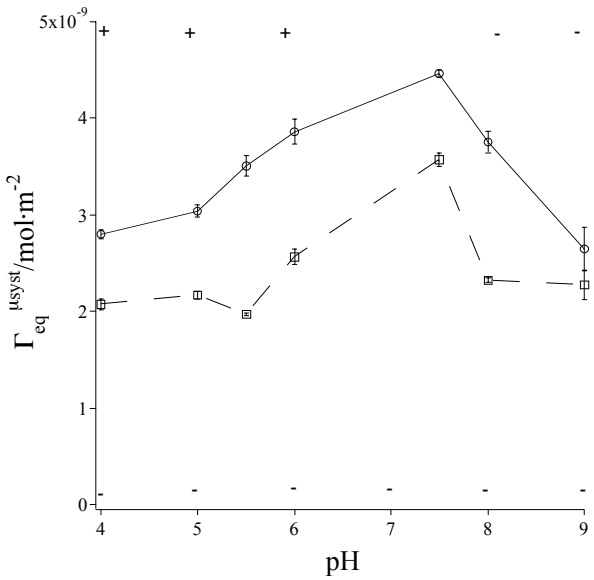

Figure 5.8. Dependence on pH of the plateau values of the adsorption on amorphous TiO_2 in 10^{-3} M NaCl. Open circles, full line: values for the adsorption; open squares, dashed line: values for the desorption. The overall charges of the proteins and the surface at each pH value are shown on top and bottom of the graph respectively.

5.4 Conclusions

The adsorption of IgG polyclonal antibodies on TiO_2 nanomaterial coated microchannels is studied. In the literature only another contribution on this subject is found to enlighten the competition between the phosphate group and IgG for adsorption in titania.

TiO_2 is used under the form of anatase nanowhiskers with a point of zero charge at pH 6, and amorphous TiO_2, with a p.z.c. below pH 3. The two materials are similar in their active surface area. The kinetics of IgG adsorption on TiO_2 is compared to the kinetic of adsorption on bare and oxidised PET, revealing that both the thermodynamic constant and the Γ_{max} are

increased up to three times compared to that of PET, when the maximum possible amelioration is about 10 times in the case of a monolayer of IgG.

The kinetics of adsorption is also faster for the TiO_2 anatase. In any case, the kinetic is adsorption limited: the simulations carried out with the finite element model described in chapter 3 give kinetic constants which are much lower than those for a diffusion limited process. Energetic barriers between the surfaces and the IgG molecules can explain this fact. It was found that electrostatic forces play a major role in the binding, both on PET and TiO_2: lower adsorption values, in fact, were found at high salt concentrations, where the electrostatic charges of the surface and the proteins are shielded. The adsorption as a function of pH follows the normal trend for PET and anatase, with a maximum in the adsorption at the pI of the protein and lower values at acid and basic pH. For the amorphous TiO_2 the maximum occurs at pH 9.5. This would indicate that the binding occurs mainly through hydrophobic forces or, more likely, hydrogen bonds, even because a strong desorption is measured for this substrate.

References:

(1) Walls, K. W.; Bullock, S. L.; English, D. K. *Journal of Clinical Microbiology* **1977**, *5*, 273-277.

(2) Colyer, C. L.; Tang, T.; Chiem, N.; Harrison, D. J. *Electrophoresis* **1997**, *18*, 1733-1741.

(3) Sato, K.; Tokeshi, M.; Kimura, H.; Kitamori, T. *Analytical Chemistry* **2001**, *73*, 1213-1218.

(4) Carnevale, S.; Rodriguez, M. I.; Santillan, G.; Labbe, J. H.; Cabrera, M. G.; Bellegarde, E. J.; Velasquez, J. N.; Trgovcic, J. E.; Guarnera, E. A. *Clinical and Diagnostic Laboratory Immunology* **2001**, *8*, 174-177.

(5) Bernard, A.; Michel, B.; Delamarche, E. *Analytical Chemistry* **2001**, *73*, 8-12.

(6) Weiping, Q.; Bin, X.; Lei, W.; Chunxiao, W.; Danfeng, Y.; Fang, Y.; Chunwei, Y.; Yu, W. *Journal of Colloid and Interface Science* **1999**, *214*, 16-19.

(7) Roberts, C. J.; Davies, M. C.; Davies, J.; Dawkes, A. C.; Tendler, S. J. B.; Williams, P. M. *Abstracts of Papers of the American Chemical Society* **1995**, *209*, 308-POLY.

(8) Topoglidis, E.; Cass, A. E. G.; Gilardi, G.; Sadeghi, S.; Beaumont, N.; Durrant, J. R. *Analytical Chemistry* **1998**, *70*, 5111-5113.

(9) Ellingsen, J. E. *Biomaterials* **1991**, *12*, 593-596.

(10) Giacomelli, C. E.; Avena, M. J.; DePauli, C. P. *Journal of Colloid and Interface Science* **1997**, *188*, 387-395.

(11) Oliva, F. Y.; Avalle, L. B.; Camara, O. R.; De Pauli, C. P. *Journal of Colloid and Interface Science* **2003**, *261*, 299-311.

(12) Moulton, S. E.; Barisci, J. N.; McQuillan, A. J.; Wallace, G. G. *Colloids and Surfaces a-Physicochemical and Engineering Aspects* **2003**, *220*, 159-167.

(13) Horbett T. A., e., Brash J. L., ed. *Proteins at interfaces II : fundamentals and applications*; Washington, DC : American Chemical Society, 1995, 1995.

(14) Rossier, J. S.; Gokulrangan, G.; Girault, H. H.; Svojanovsky, S.; Wilson, G. S. *Langmuir* **2000**, *16*, 8489-8494.

(15) Roberts, M. A.; Rossier, J. S.; Bercier, P.; Girault, H. *Analytical Chemistry* **1997**, *69*, 2035-2042.

(16) Chen, W.; McCarthy, T. J. *Macromolecules* **1997**, *30*, 78-86.

(17) Lionello, A., Josserand, J., Jensen, H., Girault, H. H. *submitted for publication* **2004**.

(18) Ros, A. PhD Thesis, Lausanne, 2000.

(19) Grossman, P. D.; Colburn, J. C. *Capillary Electrophoresis: Theory and Practice*, 1992.

(20) Weast, R. *Handbook of Physical Chemistry*, 66th ed., 1985.

(21) Buijs, J.; vandenBerg, P. A. W.; Lichtenbelt, J. W. T.; Norde, W.; Lyklema, J. *Journal of Colloid and Interface Science* **1996**, *178*, 594-605.

(22) Norde, W. *Advances in Colloid and Interface Science* **1986**, *25*, 267-340.

(23) Vikholm, I.; Teleman, O. *Journal of Colloid and Interface Science* **1994**, *168*, 125-129.

(24) Butler, J. E.; Ni, L.; Nessler, R.; Joshi, K. S.; Suter, M.; Rosenberg, B.; Chang, J.; Brown, W. R.; Cantarero, L. A. *Journal of Immunological Methods* **1992**, *150*, 77-90.

(25) Thies, M. J. W.; Kammermeier, R.; Richter, K.; Buchner, J. *Journal of Molecular Biology* **2001**, *309*, 1077-1085.

(26) Gibbs, J.; Root, D.; Brown, K. *Clinical Chemistry* **1989**, *35*, 1190-1190.

(27) Hofstee, B. H. J.; Otillio, N. F. *Journal of Chromatography* **1978**, *159*, 57-69.

(28) Connor, P. A.; McQuillan, A. J. *Langmuir* **1999**, *15*, 2916-2921.

Multi “Stop-Flow” for Microimmunoassays

6.1 Introduction

The advantages of the integration of immunoassays, such as the reduced assay time and the lowered consumption of samples have been reported several times even in this dissertation. On the other hand, miniaturisation implies some drawbacks that must be overcome to widely diffuse microimmunoassays. During the immunotest, some steps require the incubation of the molecule: in chapter 3 we have studied the problem of the solute depletion that can occur in this case. This phenomenon, implicit in microsystems, eventually leads to a smaller adsorption of the biomolecules involved in the immunoreaction, finally causing a decrease in the signal from the probes that are being analysed. Renovating the depleted solutes and performing the incubation in more than just one step with a multistep “stop-flow” procedure can be a way to alleviate (and resolve) the problem. This can easily be done, as miniaturised systems can be easily connected to pumping devices.

In chapter 3 we observed that solute depletion is more important when the analyte is at low concentration and when the sorbent is very active in adsorption. It could seem we fall into a paradox: on one side, in order to enhance the final signal, we look for phases that adsorb more actively the antibody or the antigens; on the other side, these phases deplete the solution even in a strong way, decreasing the performance of the test. The multi “stop-flow” procedure comes handy, as it is especially effective with those phases that are more active than the simple PET, used until now in our lab.

While developing heterogeneous immunoassays, another fundamental issue is often overlooked: the decrease in the activity of the passively adsorbed antibodies,[1] due to conformational changes

upon the process of adsorption,[2-7] resulting in a loss of sensitivity of the test. A classical example of this problem is represented by polyclonal capture antibodies that immobilised on Immulon 2 polystyrene, used in the microtiter wells for a common ELISA, retain only 10% of their activity. It is necessary to research new phases that could overcome this problem.

In this study, heterogeneous immunoassays are carried out in microchips presenting three different sorbent phases: PET, amorphous TiO_2 nanorods and anatase TiO_2 nanowhiskers. The stop flow is used to obtain the ideal coverage on the surface of the microchannel and to enhance the final response of the assays in the three cases. The three phases studied here present different capacity binding values (a parameter defined in the chapter 4 of this dissertation); this allows to exploring the effects of this quantity on the sensitivity of immunoassays performed with the multi “stop-flow” procedure.

For this study, the immunoassays are carried out in the competitive format (the main features of a competitive immunoassay were explained in chapter 1). In this format the antigen competes with a labelled antigen for a few active sites, namely the antibodies adsorbed on the polymer support at low surface concentration. This allows an efficient competition between the two forms of antigen, in order to obtain a reproducible calibration curve for an assay with a low limit of detection (LOD), *i.e.* with good sensitivity. Different calibration curves as a function of the concentration of the antigen and for different surface concentrations on the capture antibody are shown in Fig. 6.1. It is illustrated that for any given concentration of the antibody, increases in antigen concentration only alter the (fluorescence) signal above a critical region of antigen concentration. Below that point, in the region of constant proportional binding, changes in antigen concentration give only imperceptible changes in the percentage of total antibody bound. The position of this critical region decreases with decreasing concentration of antibody. The use

of low antigen concentrations therefore necessitates the use of correspondingly low antibody concentrations to maintain the assay in the region where further addition of antigen gives detectable displacement of the labelled antigen binding. In other words, to have a low LOD, *i.e.* a good test performance, low surface concentrations of capture antibody must be used.

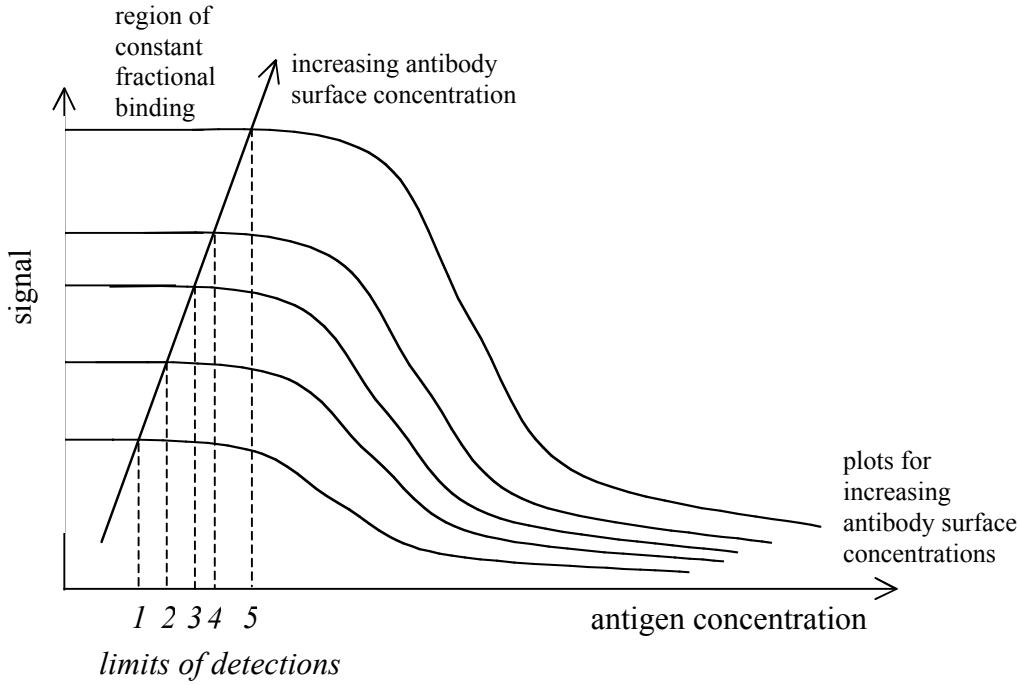

Figure 6.1. Effect of the antibody surface concentration on the calibration curves for a competitive immunoassay.

To obtain this, the antibodies are adsorbed from low concentrated solutions. We can easily imagine that, if we perform this operation on a strong adsorbing phase, the consequences of the solution depletion on the test performance can be disastrously surprising, as the antibody surface concentration obtained can be much lower that the theoretical one: in that case, the LOD will be good, but the signal extremely low.

In this work, the multi “stop-flow” is used to increase the surface concentration of antibodies and also during the antigen-antibody reaction, incubating the antigen manifold. The results of the test are analysed in terms of the activity of the capture antibody. The confocal microscope is used here as a fluorescence detector as already done, and also to pattern the homogeneity of the adsorbed antibodies: a constant and homogeneous signal from the entire channel is required in fact for a reliable and reproducible immunoassay.

6.2 Experimental

6.2.1 Immunoassays

The PET microchannels were built by laser ablation, oxidised and coated with TiO_2 nanorods and nanowhiskers as already described in the previous chapters.

The immunoassays were performed on the different phases according to the following steps: capture anti-goat IgGs (SIGMA) raised in mouse were adsorbed for 1 hour from a 10^{-2} mg·mL^{-1} solution in PBS (SIGMA; pH 7.4). The channels were then washed 3 times pushing in the channel a 0.1% solution of Tween-20 (SIGMA) in PBS with a pipette. After blocking the surface with a 5% solution of BSA (SIGMA) for 2 hours and washing, the immunoassays were carried out in the competitive format. To do that, 10 μL of 6.7×10^{-8} M solution in PBS of Cy5 linked anti-rabbit IgG raised in goat (Amersham-Pharmacia) were mixed to 40 μM of differently concentrated solutions in PBS of non-labelled anti-rabbit IgG raised in goat (SIGMA): the labelled and non-labelled complements to the capture antibody were let react for 1 hour. Then, the channels were washed with the Tween-20 solution and the fluorescence measured with the confocal microscope as already described.

6.2.2 Stop-flow for the capture antibody

Several incubation steps of one hour were performed with the capture antibody. The channel was washed just after the final *N* step and, after blocking with BSA, the two complements to the antibody was let incubate as described above and the fluorescence measured. Different channels were used for the result for each number of steps *N*.

6.2.3 Stop-flow for the antigen

After the *N* (depending on the phase) incubations of the antibody, the channel was washed and blocked with BSA. The mixture of labelled and non-labelled antigen was incubated several times. After the last step *N*, the channel was washed and the fluorescence measured.

6.2.4 Activity of the antibodies on the three phases

It can be measured with an immunoassay. In order to know the surface concentration of the capture antibodies, Cy5-linked anti-goat immunoglobulins G (from Amersham) were adsorbed on PET, TiO_2 nanowhiskers and nanorods modified microchannels from a 6.7×10^{-7} M solution in PBS (pH 7.4), in carbonate buffer (pH 9.2) and citrate buffer (pH 4) for 30 minutes and the fluorescence measured. The same non-labelled antibodies (from SIGMA) were used to coat other microchannels in which, after washing and blocking with BSA, the reaction with the fluorescent complement (Cy5 linked anti-rabbit IgG raised in goat (Amersham)) to the antibody was performed at pH 7.4. The fluorescence was finally measured. The ratio of the fluorescence from the antigens to the fluorescence of the antibodies is taken as an indication of the activity of the capture antibodies.

6.2.5 Confocal microscope scanning of the channels

The different surface treated microchannels were coated with a 6.7×10^{-7} solution of Cy5 linked anti-mouse IgG for one hour. After washing, the channels were scanned with the confocal

microscope. Different scans distant 10 μm from one another were carried out in order to have an image of the uniformity of the protein in the channel.

6.3 Results and Discussion

6.3.1 How to use φ and α

The final value of the antibody surface concentration in an ideal system can be obtained from eq. 3-4, knowing the concentration $C°$ of the antibodies, the thermodynamic constant K of the system antibody-sorbent and the concentration of active sites on the support Γ_{max}. However, as just said, the final value of the adsorbed analyte will be lower than the theoretical value. The final value of the coverage in the microsystem can be obtained using the plots of Fig. 3-6, knowing the ideality in binding of the microchannel φ ($= h/K\Gamma_{max}$), defined in this dissertation in eq. 3-14, and the "motivating force to adsorption" ψ ($=KC°$),[8] both depending on K and therefore on the type of surface employed. Once that we know φ for a determined system, the relative adsorbing capacity of that system α can be calculated ($\alpha = 1/(1+\varphi)$, from eq. 4-4). This parameter renders us able to know the number of steps necessary to attain the theoretical coverage with a multi "stop-flow" procedure.

The surfaces studied here are PET, amorphous TiO_2 nanorods and anatase TiO_2 nanowhiskers. The values of φ and α for these systems are reported in Tab. 6.1. The plot for φ values between 0 and 5 is proposed in Fig. 6.2a, as it comprises the values for the microsystems here studied. The plots for the corresponding α values are given in Fig. 6.2b (obtained in the same way of the plots of Fig. 4.3).

From the plots of Fig. 6.2a it can be observed that the adsorption in a microsystem compared to an ideal one increases when φ increases. This effect can be explained by observing that a

microsystem is more similar to an ideal semi-infinite diffusion system when the first has a high ideality in binding φ, *i.e.* K or Γ_{max} low compared to the height of the system.

This is exactly what happens in any semi-infinite diffusion system where the adsorption is small compared to the amount in solution (which is infinite!). From Fig. 6.2b it can be observed that number of necessary loads to obtain full coverage increases when the relative adsorbing capacity of the microsystem α increases.

Support	φ	α	N
bare PET	4.8	0.24	3
oxidised PET	0.42	0.78	9[a]
amorphous TiO_2 (320 $m^2 \cdot g^{-1}$)	0.63	0.70	7
amorphous TiO_2 (400 $m^2 \cdot g^{-1}$)	0.8	0.65	7
anatase TiO_2	0.32	0.82	10[b]

Table 6.1. Values of α and φ for the different sorbents coating the PET channels. N represents the number of multi "stop-flow" steps necessary to obtain the full coverage, as described in Fig. 6.2b. The values of K and Γ_{max} used to calculate φ and α are those obtained from the isotherms described in chapter 5 for the same surfaces (Tab. 5.1).
a) Number of steps to obtain 95% of the full coverage: the PET is oxidised to fix TiO_2 particles on PET; b) number of steps necessary to obtain 90% of the full coverage with the plots of Fig. 6.2b.

When φ is high, the surface has a low α value, so that it loads all the adsorbate that it can adsorb in only a few steps. On the contrary, the process works with an optimal effectiveness when the surface can load a lot of adsorbate for a lot of steps.

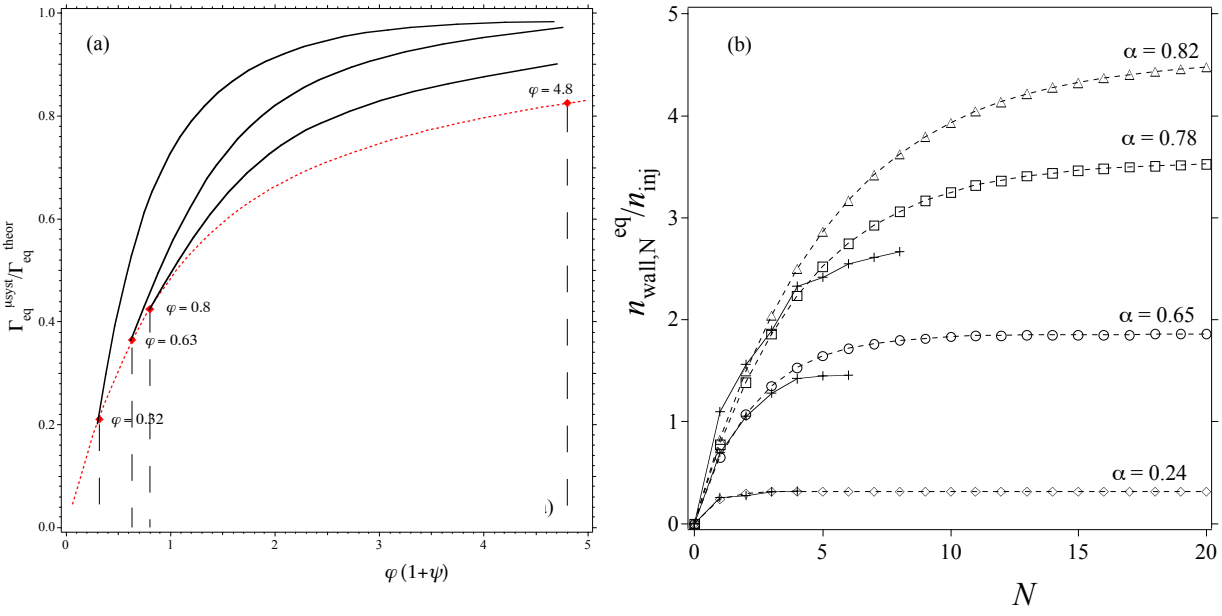

Figure 6.2(a). Working curves to estimate the coverage in a microsystem as depicted in chapter 3 (Figure 3.6). The dotted line shows the lowest possible values of $\Gamma_{eq}^{\mu syst}/\Gamma_{eq}^{theor}$ obtainable in a microsystem characterised by a defined φ (from left to right $\varphi = 0.32$ for TiO_2 anatase, $\varphi = 0.68$ and 0.8 for TiO_2 amorphous coated microchannels and $\varphi = 4.8$ for PET). Each full line curve is obtained for growing values of $KC°$.

(b). Representation of the number of moles adsorbed at equilibrium compared to the number of moles injected in the microchannel as a function of the number N of successive loads in a multi "stop-flow" procedure. The plots, calculated as those of Fig. 4.3, represent the cases of PET, TiO_2 nanorods and TiO_2 nanowhiskers coated microchannels. They are useful to calculate how many multi "stop-flow" steps are needed to reach the full coverage of the walls. When $\alpha = 0.24$ (PET) 3 steps are necessary, while when $\alpha = 0.65$ (amorphous TiO_2), and 0.82 (anatase), 7 and 10 steps (to reach 90% of the coverage) are needed. The experimental results for PET, amorphous TiO_2 and anatase, are shown with +.

Performing the multi "stop-flow" on bare PET is useless because the relative adsorbing capacity α is low. For the competitive immunoassay, we can consider performing the adsorption of the antibody from a solution with a concentration $C° = 10^{-8}$ M, which leads to $\psi = 0.08$, since the thermodynamic constant for IgG adsorption on PET is $K = 0.8 \times 10^7$ M^{-1} ($\psi = KC°$). For PET $\varphi = 4.8$ and from Fig. 6.2a, we can see that for these conditions a coverage in the microsystem of about 80% of the theoretical coverage is possible. From Fig. 6.2b it can be observed that for

PET, with α = 0.24, 3 steps are needed to reach the plateau of the plot, *i.e.* the theoretical coverage.

In chapter 5 it is shown that with amorphous TiO_2 nanorods the adsorption of the capture antibody is improved twice. It was shown that hydrophobic forces and hydrogen bonds might play a major role in the IgG adsorption on this phase. As α = 0.65, 7 multi "stop-flow" steps are needed to reach 99% of Γ_{eq}^{theor} (Fig. 6.2b). In this case the multi "stop-flow" procedure will be very effective and useful as the coverage after one step, in fact, is less than 50% of the theoretical one (as shown in Fig. 6.2a for φ = 0.7).

Anatase TiO_2 nanowhiskers represent a more efficient phase. As seen in chapter 5, they improve the capture antibody binding by 3 times with respect to PET. The driving force of the adsorption seems to be mainly electrostatic forces. This phase is very active in adsorption: α is very high (α = 0.82, and the ideality for binding of the microsystem is very low: φ = 0.32). The coverage after one step adsorption is about 20% of the theoretical one (see Fig. 6.2a), therefore, the multi "stop-flow" is very useful in this case. 10 steps are required to reach 92% of the theoretical coverage, as shown in Fig. 6.2b.

6.3.2 The "stop-flow" for the microchannel coating

In Fig. 6.3 the results of immunoassays performed in PET microchannel are shown. The antibody was coated with the multi "stop-flow" procedure. Theoretically 3 steps were required: 4 steps were performed before the immunoreaction showed the saturation was reached, with a gain in the fluorescence signal of 15%. The LOD after one step (*i.e.* as after a normal immunoassay) is 7×10^{-9} M, while after 4 loads is 10^{-8} M. Obviously, after increasing the antibody surface concentration, we follow here the classical behaviour of competitive immunoassay shown in Fig. 6.1, improving the signal with a loss of sensitivity.

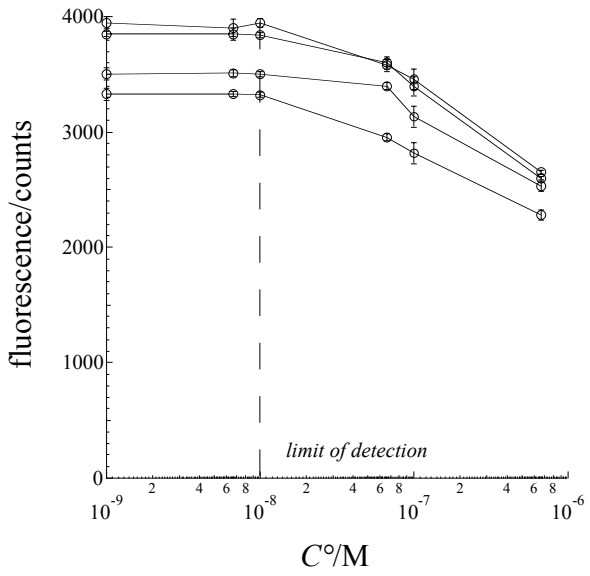

Figure 6.3. Immunoassays for which the IgG adsorption on PET was performed with a multistep "stop-flow" procedure. The fluorescence intensity from the IgG raised in goat used as a complement to the capture anti-goat antibody in the assays is given as a function of the concentration of goat IgG. A constant concentration of the labelled antigen was used in all the experiments ($C° = 10^{-8}$ M) and aliquots of 10 μL were added to the aliquots at different concentrations of 40 μL of the non-labelled anti-mouse IgG. Since the two species in the sample compete for antibody binding, the amount of labelled antigen decreases when the concentration of antigen in the sample increases. The concentration of the antigen in a given sample can therefore be determined by tracking the amount of antibody-bound fluorescent antigen.
The coating of the capture antibody has been carried out with a multistep "stop-flow": one step was performed for the first lowest plot, then the reaction with the antigen was done and the fluorescence measured. In another channel, a two steps coating was done and so forth, up to the *N* step.

The same procedure is followed for IgG adsorption on amorphous TiO_2 and the results are shown in Fig. 6.4. Theoretically 7 steps were required to obtain the full coverage: 6 steps were performed and no change in the fluorescence is displayed after 5 steps. An increase of more than 40% of the signal is obtained, with a reduction of sensitivity from 3×10^{-9} M to 10^{-8} M. The difference of LOD loss with respect to PET is easy explainable by observing that, in the case of PET, $\Gamma_{eq}^{\mu system}$ is 80% of Γ_{max}^{theor} and in the case of TiO_2 is 40%: the increases in the $\Gamma_{eq}^{\mu syst}$

towards Γ_{max}^{theor} at each "stop-flow" step are smaller for PET than for amorphous TiO_2 and this translates into lower decrease in sensitivity.

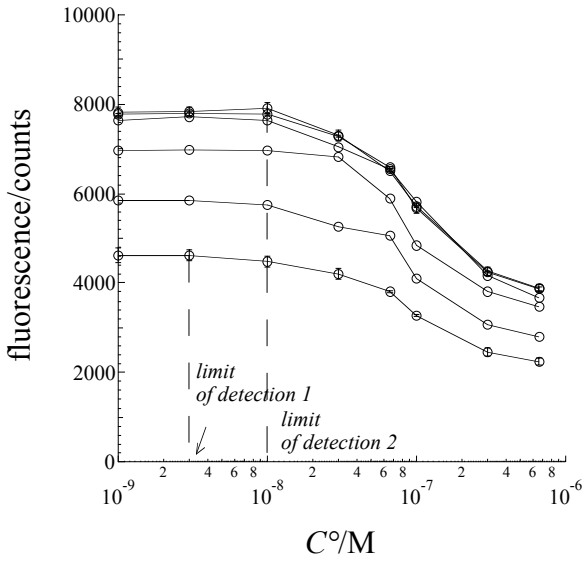

Figure 6.4. Immunoassays for which the IgG adsorption on amorphous TiO_2 was performed with the same multistep "stop-flow" procedure as in Fig. 3. The LOD at the beginning of the procedure is 3×10^{-9} M, while at the end, after 6 step is 10^{-8} M

Fig. 6.5 shows that on anatase TiO_2 the saturation is reached after 8 coatings (instead of 10), which is well in accordance with the 10 steps theoretically required. The increase in the signal is more than 50% with no appreciable decrease in sensitivity (10^{-8} M).

It is interesting to observe that the same trend in the signal gain as in the gain of the coverage theoretically predicted is followed for the three phases. In Fig. 6.2a it is shown that for PET after the first coating $\Gamma_{eq}^{\mu syst}$ is 80% of Γ_{eq}^{theor}; for amorphous TiO_2 we have 40% and for anatase TiO_2 about 20%. From the results of the multi "stop-flow", the value for $\Gamma_{eq}^{\mu syst}$ at the first step is

85%, 60% and 47% of Γ_{eq}^{theor} for the three systems respectively. The gain in fluorescence is the same as $\Gamma_{eq}^{theor} - \Gamma_{eq}^{\mu syst}$.

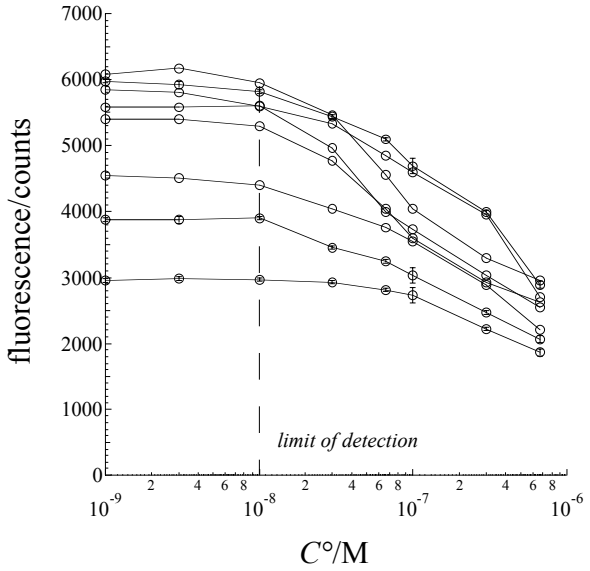

Figure 6.5. Immunoassays for which the IgG adsorption on anatase TiO_2 was performed with the same multistep "stop-flow" procedure as in Fig. 6.2.

We can now comment the experimental data displayed in Fig. 6.2b (crosses) which were calculated from the results of Fig. 6.3, 6.4 and 6.5 at antigen concentration $C° = 10^{-9}$ M. The moles of antibody adsorbed at each step (obtained from the fluorescence counts with the calibration plot described in chapter 2) were divided by the number of moles of antibody injected. The results fit well in the case of PET (unless a factor due to the activity of the antibody on the different surfaces, as explained below). In the case of the titania surfaces a good agreement is found for the first 4 steps. The slight deviation found after is due to the fact that the antibody concentration used ($C° = 10^{-8}$ M) gives $\psi = 0.08$ for PET, 0.3 for amorphous TiO_2 and 0.5 for anatase. In the first case we are in the good conditions for the "stop-flow", while for the

titania phases ψ is higher, leading to a weaker depletion effect: consequently the saturation is reached in fewer steps than expected.

6.3.3 The "stop-flow" for the immunoreaction

The usefulness of the multi "stop-flow" was also tested for the reaction between the antigen and the antibody. This was possible because of the low concentrated solutions implied in the test (the multi "stop-flow" assumes low concentrated solutions). The thermodynamic data on the antigen-antibody reaction also suggest that the multi "stop-flow" can lead to significant results in this case. The thermodynamic constant K of the immunogenic reaction has values from 10^8 to 10^{12} M^{-1}.[9] The active sites concentration Γ_{max} is a percentage of the total number of antibodies adsorbed on these supports, which normally ranges from less than 1% to about 10% for passive adsorbed antibodies. Only the active antibodies can be taken into account: this means that the active antibodies surface concentration should be around 10^{-10} and 10^{-9} mol·m^{-2}. Knowing that the microchannels are 50 μm high, a φ value between 0.5 and 5 can be estimated, which is in the

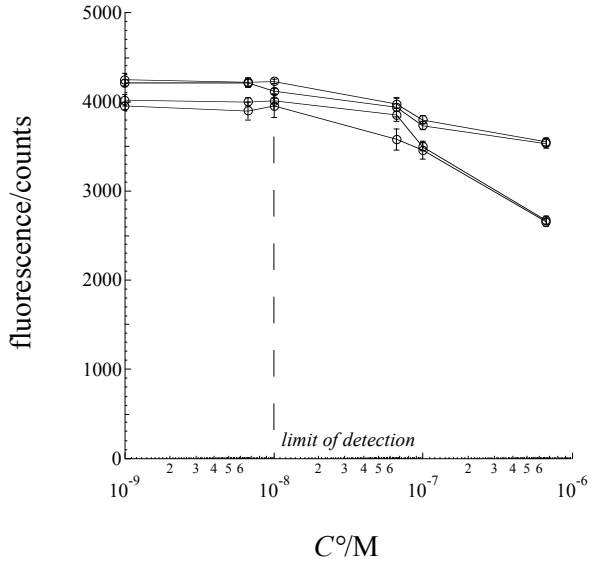

Figure 6.6. Results for immunoassays performed on PET microchannels with a multistep "stop-flow" procedure for the antigen immunoreaction. The "stop-flow" incubations were realised until no change in the signal was observed (here 5 steps were done). No change in the LOD was obtained.
The coating of the antibody was also realised with the "stop-flow": the first, lowest plot in fact corresponds to the highest plot of Fig. 6.3.

range for an efficient multi "stop-flow".

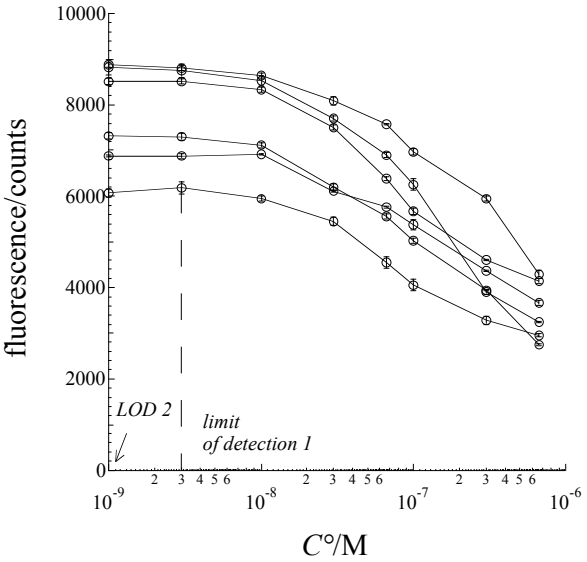

Figure 6.7. Results for immunoassays performed on amorphous TiO_2 coated microchannels with the same multistep "stop-flow" procedure for the antigen immunoreaction as in Fig. 6.6. A LOD gain from 3×10^{-9} M to 10^{-9} M is obtained.

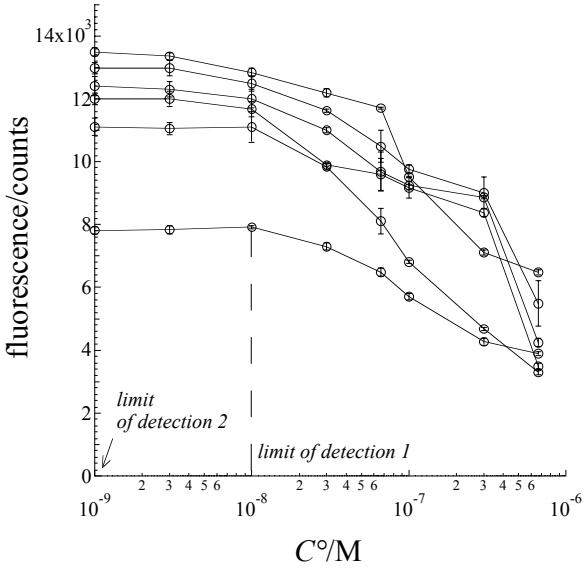

Figure 6.8. Results for immunoassays performed on anatase TiO_2 coated microchannels with the same multistep "stop-flow" procedure for the antigen immunoreaction as in Fig. 6.6. A LOD gain from 10^{-8} M to 10^{-9} M is obtained.

The results of an immunoassay where the multi "stop-flow" was performed for the immunoreaction between the antibody and the antigen are shown in Fig. 6.6, 6.7 and 6.8 for PET, amorphous and anatase TiO_2 respectively. The capture antibody coating was also done with the multi "stop-flow" as just described above, *i.e.* the first lowest plots in the figures 6.6, 6.7 and 6.8 correspond to the last highest plots in Fig. 6.3, 6.4 and 6.5. The multi "stop-flow" incubations of the antigens were performed until no change in signal was observed.

For PET (Fig. 6.6), 4 steps were performed, gaining 10% of the maximal fluorescence signal but without improving the limit of detection (LOD), which is 10^{-8} M. On amorphous TiO_2 coated microchannel (Fig. 6.7), an increase in the signal of about 40% and a LOD one order of

magnitude better are observed. This amelioration is comparable to that obtainable using an enzyme labelled antigen. A similar result is obtained on anatase TiO_2 and shown in Fig. 6.8, where the gain in fluorescence is about 30% with an improvement in the LOD to 10^{-9} M.

6.3.4 Activity of the physisorbed antibodies

In order to verify the antibodies activity, a simple immunoassay was performed and the fluorescence from the antigen was displayed in Table 6.2 as the percentage of active antibodies adsorbed in acid, neutral and basic pH. The value registered in this work for the activity of antibodies adsorbed on PET at pH 7.4 is 7%. In chapter 5 it is shown that there is an important variation of the amount of antibodies adsorbed at different pH. Here it is verified that there is no substantial change in the activity of the antibodies adsorbed in acid and basic conditions. This shows that the possible structural changes, which occurred in basic and acid environments, are then recovered in the neutral pH at which the antibody-antigen reaction occurs. The antibodies adsorbed on amorphous TiO_2 at three different pH exhibit almost the same activity (~ 11%).

It is worth noticing that the value of 14% for the activity for the IgG adsorbed at pH 4 is relative to a value of adsorbed capture antibody, which in chapter 5 we observed to be almost 3 times lower than that at pH 7.4: therefore, we endorse the position of J. E. Butler, saying that at acid pH the adsorption decreases even if a higher proportion of functional activity might be retained.

support	pH 4	pH 7.4	pH 9.2
bare PET	9.3 %	7 %	6.9 %
amorphous TiO_2 (400 $m^2 \cdot g^{-1}$)	14.5 %	11.7 %	12.1 %
anatase TiO_2	10.5 %	11.0 %	11.9 %

Table 6.2. The proportion of functional active sites of the capture antibody after passive adsorption on oxidised PET, amorphous TiO_2 and anatase at pH 4, 7.4 and 9.2.

Adsorption on anatase shows the same features, even if the activity is incremented almost twice with respect to PET. As already observed[1] for passive adsorption of IgGs on polystyrene, these data show that in these microsystems there is a dramatic loss of the protein function, even if on TiO_2 the activity is double with respect to PET. This is due to molecular alterations, which in turn can alter function. Many studies on adsorbed monoclonal antibodies have suggested an adsorption induced denaturation.[10] In monoclonal antibodies, losses of 97 % of the activities have already been observed, while for polyclonal antibodies the losses are around 90 – 93%, which is in accordance with the values found in this work. The activity of the capture antibody on TiO_2 coated microchannels, doubled with respect to that of PET, certainly plays a role in the efficiency of the multi “stop-flow” procedure because the competition between labelled and non-labelled antigens can achieve completion in more steps that for the capture antibodies adsorbed on PET.

As a decrease in activity hampers a homogeneous distribution of the passively adsorbed

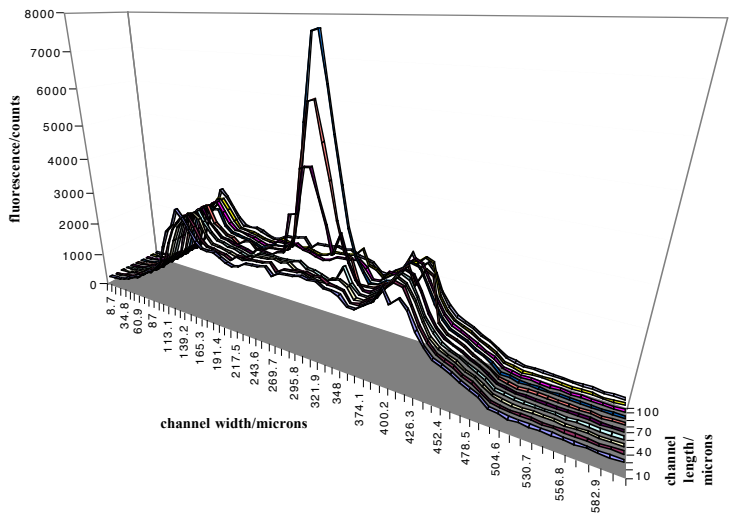

Figure 6.9. Confocal scan of a PET microchannel: the microchannel was scanned horizontally 10 times with steps of 10 μm. The fluorescence spike in the centre of the channel represents at least one possible aggregate of labelled antibody. The edges of the channel exhibit a stronger fluorescence because the signal from part of the vertical wall is collected.

antibodies on polystyrene, the sorbent phases were scanned with the confocal microscope after adsorption of the fluorescent IgG. On PET, aggregates of proteins are observed.

The scan of the channel in Fig. 6.9 shows a peak almost 70 μm wide. Since the longitudinal resolution of the microscope is 20 μm, this probably means that several aggregates may lay within this distance. Aggregates of proteins may be adsorbed because of the potentially larger number of contact sites with the surface.[1] Such a mechanism would be proven by the correlation between adsorption avidity and molecular weight, which suggests that large molecules are preferentially adsorbed. It was also speculated that clusters of IgGs adsorbed on polystyrene represent the surviving functional capture antibodies.[1] Because of that, the activity of the adsorbed proteins in view of an immunoassay will not be homogeneous all over the coated surface.

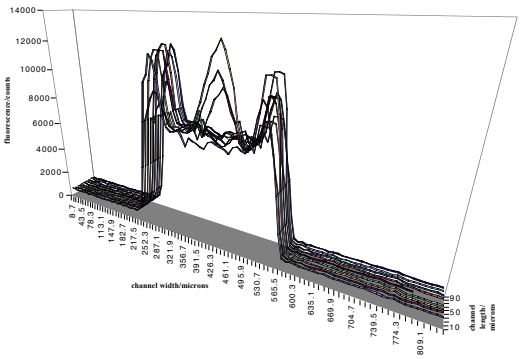

Figure 6.10. Confocal scan of an amorphous TiO_2 coated microchannel: the microchannel was scanned horizontally 10 times with steps of 10 μm. An aggregate is present in the centre of the channel like in Fig. 6.9. The edges of the channel exhibit a stronger fluorescence than in the rest of the surface as explained in Fig. 6.9. The signal from the edges is higher than in PET because the adsorption on the walls is more important.

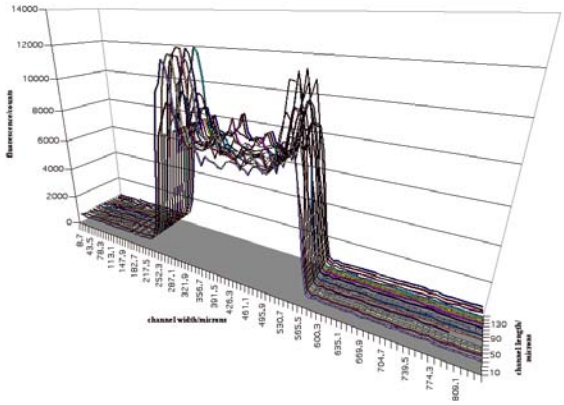

Figure 6.11. Confocal scan of an anatase TiO_2 coated microchannel: the microchannel was scanned horizontally 15 times with steps of 10 μm. The distribution of antibodies al over the surface is regular. The spikes at the edges of the channels represent the fluorescence from part of the walls collected by the microscope, as in Fig. 6.9.

Aggregates of proteins were observed also on amorphous TiO_2 as shown in Fig. 6.10: they render the coating and the antibody activity non-homogeneous. The distribution of the antibodies after the adsorption is perfectly regular on anatase TiO_2, as it can be seen in Fig. 6.11. Anatase coated microchannels could thus be a possible candidate for a disposable microimmunoassay.

6.4 Conclusions

The multistep “stop-flow” procedure has been used to improve the final limit of detection (LOD) of microimmunoassays. The tests were performed in the competitive format using the couple anti-goat IgG / goat IgG. The antigen was Cy5 labelled for fluorescence detection by confocal microscopy. The supports for the assays were PET microchannels that were also coated with amorphous TiO_2 nanorods and anatase TiO_2 nanowhiskers. The ideality for binding φ was calculated for the three different microchannels. With this value it is possible to know the percentage of coverage of the capture antibody obtainable in a microsystem with respect to the one of a bigger system: starting the adsorption from the same concentration solution, we will have relatively a less covered surface in the more adsorptive systems due to the bulk solution depletion. This can lead to surprisingly low signals, especially using those active supports that are supposed to improve the performance of the test.

This is an even trickier disadvantage for the competitive format than for the “two site” assay. Theoretically, a competitive immunoassay gives the best results when the surface concentration of the capture antibody tends to zero. The adsorption of the antibodies is then performed from low concentrated solutions, for which the depletion effect is more evident. For PET the coverage should be 80% of the ideal one, for amorphous TiO_2 it should be less than 50%, and for anatase TiO_2, around 20%.

To obtain the ideal coverage, the “stop-flow” procedure is indicated. We calculated that we needed 3, 7 and 10 steps to obtain the ideal capture antibody coverage in the three phases respectively. Experimentally 4, 6, and 8 steps were required experimentally to attain no variation in the signal from the antigen that reacted with the antibody. A slight decrease of the limit of detection (higher LOD) was observed after the “stop-flow”, as it should be, in competitive immunoassays when high surface antibody concentrations are used. Lower coverages should be tried risking a diminution of the fluorescence signal and therefore a worse test result.

The usefulness of the “stop-flow” procedure has been verified even for the immunoreaction in the three systems. This led to an improvement of one order of magnitude for the LOD on the titania phases, which is comparable to the improvement obtainable using, for instance, an enzyme labelled antigen. An explanation for the difference of behaviour between PET and TiO_2 can be the doubled activity found for antibodies adsorbed on TiO_2 phases compared to that of PET adsorbed IgG. This allows for the competition between labelled and non-labelled antigens to arrive to completion in more steps than in PET microsystems.

The microsystems were also scanned with the confocal microscope to verify the uniformity of the capture antibodies coverage, revealing that the anatase nanowhiskers, which coat uniformly the entire microchannel surface, are a reliable material for micro-immunoapplications.

References:

(1) Butler, J. E.; Ni, L.; Nessler, R.; Joshi, K. S.; Suter, M.; Rosenberg, B.; Chang, J.; Brown, W. R.; Cantarero, L. A. *Journal of Immunological Methods* **1992**, *150*, 77-90.

(2) Bull, H. B. *Biochimica Et Biophysica Acta* **1956**, *19*, 464-471.

(3) Oreskes, I.; Singer, J. M. *Journal of Immunology* **1961**, *86*, 338-&.

(4) Nyilas, E.; Chiu, T. H.; Herzlinger, G. A. *Transactions American Society for Artificial Internal Organs* **1974**, *B 20*, 480-490.

(5) Kennel, S. J. *Journal of Immunological Methods* **1982**, *55*, 1-12.

(6) Kochwa, S.; Brownell, M.; Rosenfie.Re; Wasserma.Lr *Journal of Immunology* **1967**, *99*, 981-&.

(7) Hollander, Z.; Katchalskikatzir, E. *Molecular Immunology* **1986**, *23*, 927-933.

(8) Reinmuth, W. H. *Journal of Physical Chemistry* **1961**, *65*, 473-&.

(9) Masters B. R., e. T. B. J. *Selected papers on confocal microscopy*, 1996.

(10) Suter, M.; Butler, J. E.; Peterman, J. H. *Molecular Immunology* **1989**, *26*, 221-230.

The FEM Model for Biosensoring

7.1 Introduction

Direct immunosensors detect biomolecular interactions measuring changes in capacitance,[1] mass,[2] fluorescence.[3] Optical sensors measure the change of an intrinsic optical property of a surface where a dielectric material (as a biomolecule) is loaded. They represent the most widely used instrument to obtain dynamic data of biomolecular interactions. One of the most exploited phenomena is the surface plasmon resonance (SPR). SPR is excited at a metal/dielectric interface by a monochromatic light beam under conditions of total reflection. It is observed as a deep in the intensity of reflected light at a specific angle. The position of the resonance angle depends on several factors, one of which is the refractive index of the medium in close proximity to the non-illuminating side of the metal film. The refractive index is, in turn, directly correlated to the concentration of dissolved material in the medium.

The biosensor cell has two regions as shown in Fig. 7.1, the flow channel and the region in which the biointeraction takes place. One of the reactants, the ligand, is immobilised on the sensor surface, while the other, the analyte, flows continuously over the surface.

The major advantage of this instrument is the label-free detection in real time of the binding and the dissociation processes. A disadvantage is the need to immobilise the ligand to enhance the number of bound analyte molecules. Several immobilisation chemistries are suitable for SPR immunoassays in order to immobilise the antibodies in a functional and controlled orientation. Alkanethiols,[4] silanes,[5] polipeptides[6] were used to attach the recognition elements to the SPR sensor. The most famous method involves a flexible hydrogel matrix[7] composed of carboxylmethylated dextran chains that forms a porous three dimensional linking system. The

hydrogel is attached to the sensor surface and extends about the length of the plasmon originated from the gold surface (100 nm). Adsorbing or linking a biomolecule to the gel can dramatically change its activity as the protein's tertiary structure at, or near the active site where the bond of interest is located may be altered by the immobilisation, thus changing its properties. The hindrance encountered by the analyte in the hydrogel represents a further disadvantage.[9-14]

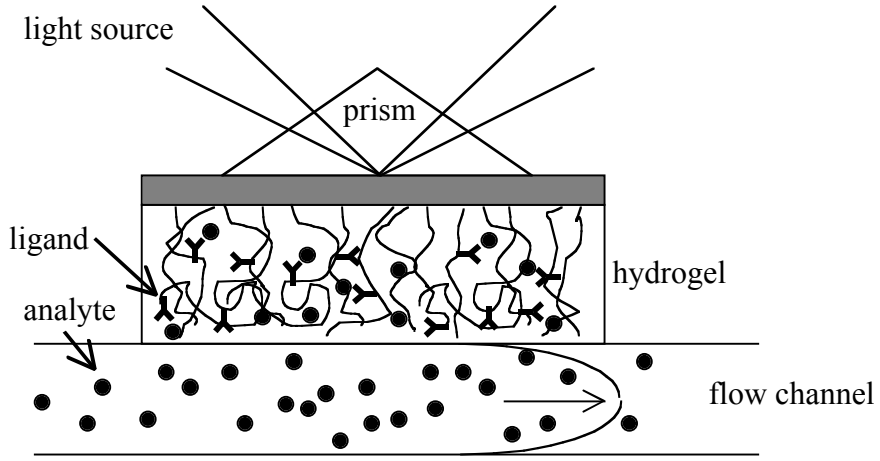

Figure 7.1. The BIACORE optical biosensor (not to scale). The hydrogel is 100 nm high approximately; the flow channel for a standard instrument is 2.4 mm long, 50 μm high and 500 μm width.[8] The ligand (antigen, receptor...) is immobilised in the hydrogel, the analyte (antibody, messenger...) flows in the channel and diffuses in the gel where binds to the ligand. The light beams probes the hydrogel and detects changes in the local refractive index due to the accumulation of analyte mass. The depth of the evanescent wave is 100 nm towards the hydrogel, *i.e.* the thickness of the hydrogel itself.

In our lab a new kind of biosensor has been developed. It is based on the capacitive coupling between electrodes placed on one side of a dielectric substrate (the polymer in which the channel is etched) and the solution in contact with the other side, in the microchannel. The principle is to form a capacitor where the charges on one side are those of the electrodes, and the charges on the other side are the ionised groups generated on the PET surface by photoablation process.[15]

This technique has been called super-capacitive admittance tomoscopy (SCAT). With the SCAT we can study the adsorption of (biological) molecules on a surface or the interaction between biomolecules (when one of them is adsorbed on the polymer surface). The molecules need not to be labelled, as in an optical biosensor, even if they need to be attached to the surface coupled with the electrodes when a biomolecular interaction is at study.

The surface can, however, be of various kinds, depending on the modification of the polymer surface. In this way the effects of the surface on the activity of the biomolecules can be studied. The diffusion of the molecules is not hindered, unless, of course, adsorption in a gel is studied.

As this is an intrinsic surface analytical technique, the dynamic data of the bioadsorption are obtained. This was not possible with the confocal microscope, unless rinsing in order to isolate the surface signal from the signal of the channel, thus interrupting the adsorption process. The SCAT is more practical and less time-consuming. The amount of data collected allows a correct interpretation of the adsorption dynamic.

The most important information obtainable from biosensors is the adsorption and desorption rates of a biointeraction by fitting the experimental data with a numerical model. SPR sensors are interesting as they have stemmed an enormous amount of numerical studies.[8,16] However, a model[17] that could study the hindered transport in the hydrogel was developed 5 years after the apparition of the first model for the BIACORE (the most famous SPR based sensor). Moreover, until Sikavitsas's model in 2002,[18] details such as the diffusion in the direction of the flow, which can affect the results especially at the entrance of the channel or using a PDF flow, were not kept into account.

The aim of this chapter is to prove that the model developed in this dissertation work fits well the data collected under flow conditions by super-capacitive admittance tomoscopy (SCAT). SCAT

coupled to the FEM model is useful to study the dynamic of adsorption of biomolecules onto different surfaces, or the interactions of biomolecules when one is linked to the surface coupled to the electrodes. This is of paramount importance for studying the dynamic of the immunoreaction in heterogeneous immunoassays on different surfaces.

A comparison with previous results from mathematical models for the BIACORE will be given, underlining that our FEM model could eventually describe hindrance in a gel by an accurate choice of the diffusivity of the adsorbing layer.

7.2 Experimental

7.2.1 Device structure

The channel in which the solution flows has been prepared by laser ablation and laminated as usual (the channels are 50 μm deep, 100 μm wide). On the other side of the PET film, two parallel microchannels with the same dimensions as the flow channel were photoablated perpendicularly to it (see Fig. 7.2). The distance between the two parallel microchannels is 200 μm centre to centre. The two channels were filled with a commercial screen-printing graphite ink (ElectraΩ ED5000 series, from Electra Polymers (England) in which gold nanoparticles (∅ = 19 nm) were mixed in order to increase the charging capacity (an aliquot of 50 μL of colloidal solution containing 48 $mg \cdot L^{-1}$ of gold nanoparticles id added to 500 mg of graphite ink). After curing at 60°C for 4 hours, the PET film was laminated on both sides as previously described. The distance between the electrodes and the microchannel is 5 μm and the detection surface area per microelectrode is 66 × 100 μm.

The admittance measurements were performed by applying an AC modulated signal with frequency ranging from 1 kHz to 1 MHz (for the calibration of the instrument) and amplitude of 3 Volts (finally, the experiments are performed at 1 MHz).

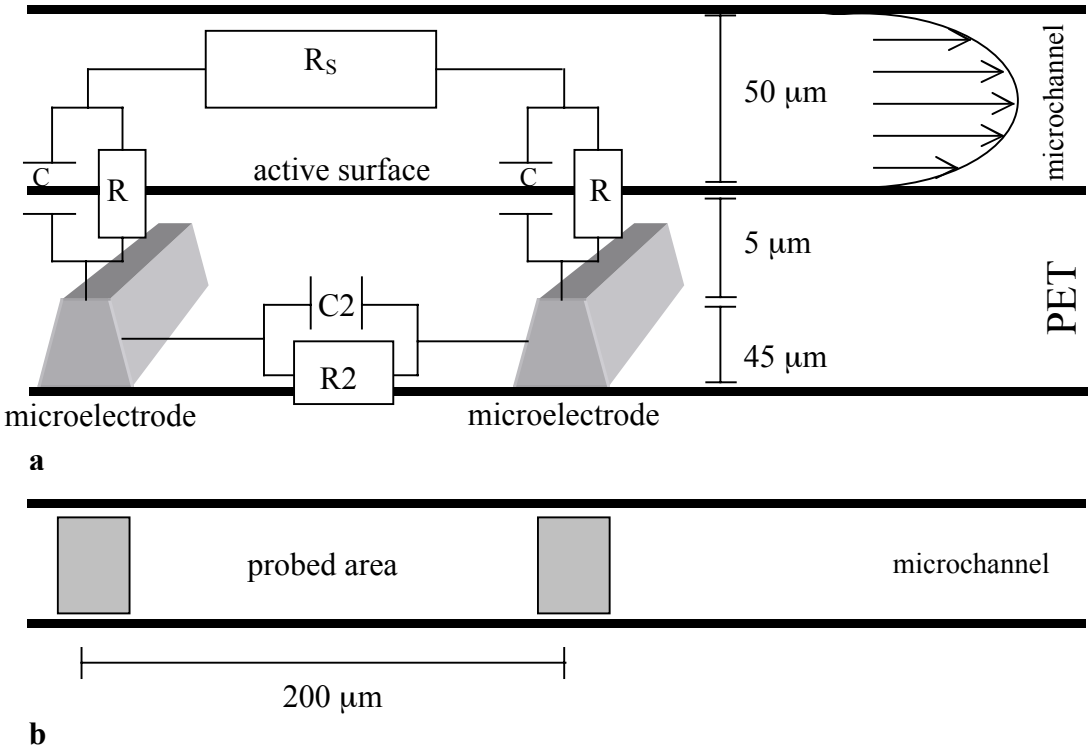

Figure 7.2. (**a)** Scheme of the super capacitance admittance tomoscope (SCAT). Two channels are etched perpendicularly to the flow channel, 5 μm distant from it and 200 μm from each other. The three channels (the flow one, 50 μm deep, and the electrodes, 45 μm) are 100 μm wide. *R* represents the resistance of the PET dielectric layer between the electrodes and the channel (it results in R_1 in the circuit of Fig. 7.3), R_2 the resistance between the two electrodes, and R_S the solution resistance through the bulk of the channel; *C* is the capacitance of the electrode/PET/channel (it results in *C* in Fig. 7.3) interface and C_2 is the stray capacitance between the electrodes. **(b)** Top view of the microchannel, with the two microelectrode on the bottom, not in contact with the solution.

A frequency response analyser is used (FRA 1255B, Solartron UK) together with a Dielectric Interface 1296 (Solartron, UK), which extends the frequency range from 10 μHz to 10 MHz. The

current measurement range of the system varies from 6 mA to 100 fA; therefore high values of impedance (100 Ω to 100 TΩ) and low capacitance values (1 pF to 0.1 F) can be collected. Data acquisition is made with the company made software SmaRT, which allows for a sampling time of 5 sec.

The evolution of the admittance measurements performed on the device filled with a buffer solution shows that the device can be regarded as a capacitive system at frequencies higher than 10 kHz (data not shown).

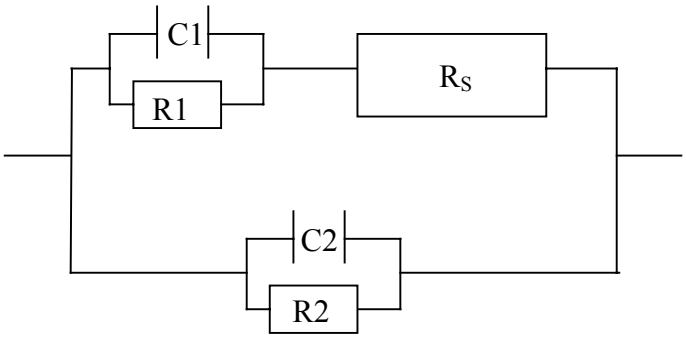

Figure 7.3. Equivalent electric circuit of the device.

The system can be modelled using the equivalent circuit in Fig. 7.3, for which the admittance corresponds to:

$$Y(\omega) = \frac{1 + j\omega R_2 C_2}{R_2} + \frac{1 + j\omega R_1 C_1}{R_S + R_1 + j\omega R_S R_1 C_1}$$

where R_1 represents the resistance of the PET dielectric layer between the electrodes and the channel, R_2 the resistance between the two electrodes, and R_S the solution resistance through the bulk of the channel; C_1 is the capacitance of the electrode/PET/channel interface and C_2 is the stray capacitance between the electrodes. Any surface channel modification results in a modification of the C_1 value. When charged molecules are adsorbed on the channel surface, the capacitance C_1 changes inducing a variation in the admittance Y (or impedance Z).

It is well known that the PET capillary surface-solution interface behaves like a capacitor. At a given potential, there will exist a charge on the polymer, q^E, and a charge in the solution, $q^S = -q^E$. The charge in solution is made up of an excess of either cations or anions in the vicinity of the capillary surface. As it is known, the whole array of charged species resembles that existing at the electrode-solution interface, and it is called electrical double layer, which is roughly modelled in Fig. 7.4. At a given potential, the electrode-solution interface is characterised by a double layer capacitance, C_d (however, unlike real capacitors, whose capacitances are independent of the voltage across them, C_d is often a function of potential).

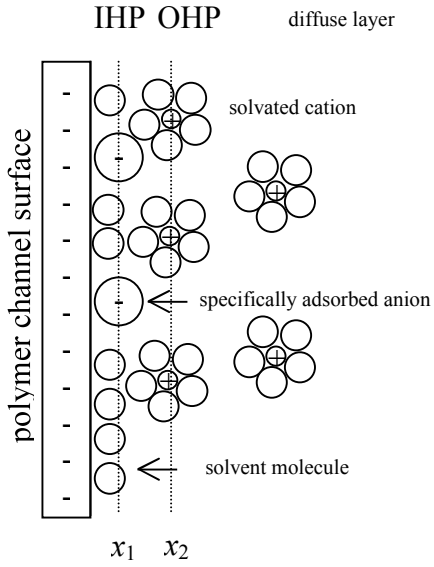

Figure 7.4. Proposed model of the double layer region under conditions where anions are specifically adsorbed.

The closest layer to the surface of the microchannel, the *inner layer*, contains solvent molecules and sometimes other species (ions or molecules) that are said to be specifically adsorbed. This inner layer is also called the *compact*, *Helmoltz* or *Stern layer*.[19] The locus of the electrical centres of the specifically adsorbed ions is called the inner Helmoltz plane (IHP), which is at a

distance x_1 from the surface. Solvated ions can approach the metal only to a distance x_2; the locus of the centres of these nearest solvated ions is called the outer Helmoltz plane (OHP). The interaction of the solvated ions with the charged electrode involves only long range electrostatic forces, so that their interaction is essentially independent of the chemical properties of the ions. These ions are said to be *non-specifically adsorbed*. Because of thermal agitation in the solution, the non-specifically adsorbed ions are distributed in a three-dimensional region called the *diffuse layer*, which extends from the OHP into the bulk of the solution. The excess charge density (the charges divided by the electrode area) in the diffuse layer is σ^d, hence the total excess charge density on the solution side of the double layer σ^S is given by $\sigma^S = \sigma^i + \sigma^d = -\sigma^E$ where σ^i and σ^E are the charge densities of the IHP and of the surface respectively.

Biomolecules non-specifically adsorbed to the polymer surface contribute to increase the excess charge density (and of course an even major change occurs for covalently bound molecules). This causes a change in the capacitance C_1 that results in a change of the measured admittance. Also ions like phosphate contribute to this change. The background due to the solution must be carefully measured to be subtracted from the total signal.

7.2.2 Protein adsorption under flow conditions

Solutions of labelled antibody (Fluorolink Cy5 labelled antirabbit IgG, Amersham Pharmacia Biotech) with concentrations ranging from 6.6 nM to 0.66 μM in 0.01 M PBS were pumped in a 1 cm long microchannel by a syringe pump (Kd Scientific) at a rate of 90 μL/h. The IgG adsorb onto the polymer surface and the variation in the admittance is recorded versus time at 1 MHz.

The kinetic isotherms obtained were simulated with the FEM model already described to obtain the kinetic rates of adsorption and desorption of the system. In order to fit the experimental data, these were normalised by Arg (Z_{max}) (assuming that the experimental plateau corresponds to the

theoretical maximum) and the 0 in the *y*-axis was taken at the signal given by the buffer solution; the modelled curves were normalised by the thermodynamic maximum.

7.3 Results and Discussion

7.3.1 The Damköhler number

To decide which values of the rates of adsorption k_{on} and desorption k_{off} give a kinetic or diffusion controlled adsorption with our model, we have to perform the simulations with the parameters of the case studied, raising the rates up to when a further augmentation doesn't lead to an increment in the velocity of adsorption. Diffusional, kinetic and mixed regimes are easily defined. In a diffusional regime, a change in the kinetic rate doesn't lead to an enhancement in the velocity of adsorption. Under kinetic limitation, the diffusivity of the analyte does not influence the adsorption. We are under a mixed regime when the influence of the two is comparable.

A non-dimensional number, the Damköhler number $Da = k_{on}\,\Gamma_{max}\,\delta/D$ can be used to quantitate if the adsorption is governed by kinetics or mass-transfer. The Da number is used for instance to discuss BIACORE results since with this tool, both under kinetic and diffusion control, mass-transfer limitations in the hydrogel can create important deviations from the model. Talking in absolute terms of diffusion or kinetic limitation becomes, thus, meaningless, and the Da number reveals its usefulness. This number is the ratio of the intrinsic forward reaction-rate to the diffusional rate and it is of critical importance in the models for optical biosensors. In the BIACORE, for instance, Γ_{max} represents the total immobilised ligand concentration: it is usually called C_L and its units are $mol \cdot m^{-3}$, so that we can use the quantity Γ' of our model, which has the same dimensions, so that $Da = k_{on}\,\Gamma_{max}'\,\delta^2/D$. The Da number has an experimental meaning

when the analyte diffuse in a matrix that can lower its diffusivity. In the present study, we cannot speak of a Da number for such a phase; however, as our model presents a 2D adsorption region, we will use it here in the context of the modelling.

The effect of different Da values in the SCAT is shown in Fig. 7.5, where the coverage at the end of the channel in function of time is plotted. The parameters used for the simulations are those obtained in paragraphs *3.4.5.2* and *4.4.2.3* for IgG adsorption on PET. As the curves are normalised by Γ_{max}, the maximum shown on the axis is not 1 as it would have been with a normalisation by Γ_{eq}. It is shown that the plots become more similar as the Da number increases, reaching the diffusion control. Over Da = 50, no further adsorption is observed. Under Da = 5×10^{-3}, a pure kinetic controlled adsorption is observed as the reaction time is $t_{reac} = 1/k_{on}C° = 1000$ sec and the diffusion time towards the wall of the channel, where there is the sensor, is $t_{diff} = h^2/2D = 31$ sec. (Similar plots in the BIACORE show a kinetic controlled adsorption faster than diffusion controlled, due to the hindrance slowing down the entire process).

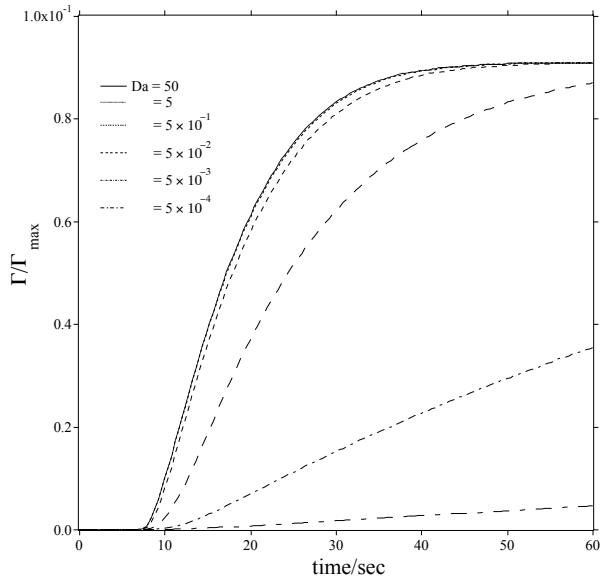

Figure 7.5. Simulation results of the wall concentration (Γ/Γ_{max}) in function of time for different Da number at the end of the channel. $D = 4 \times 10^{-11}$ m^2·sec^{-1}, $\Gamma_{max} = 10^{-9}$ mol·m^{-2}, $K = 10^4$ m^3·mol^{-1}, $C° = 10^{-5}$ mol·m^{-3} (values for IgG adsorption on PET). The Da number was changed by changing the k_{on} from 10 to 10^8 m^3·mol^{-1}·sec^{-1} and k_{off} from 10^{-3} to 100 sec^{-1}.

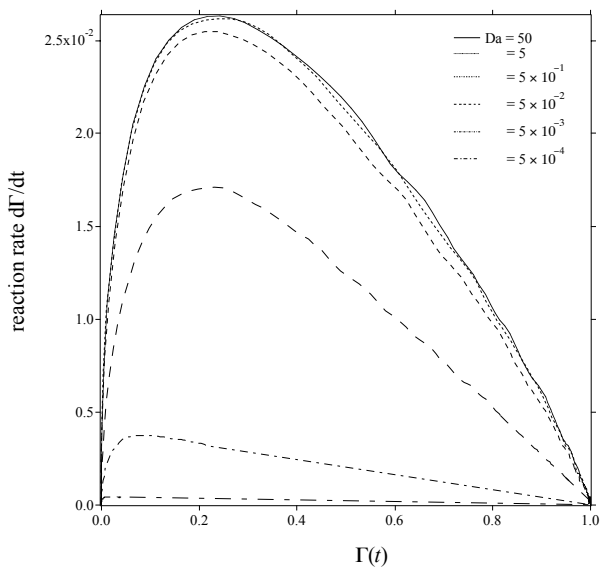

Figure 7.6. Rate of reaction vs. bound concentration as a function of Da. The same parameters of Fig. 7.5 are used for the simulations.

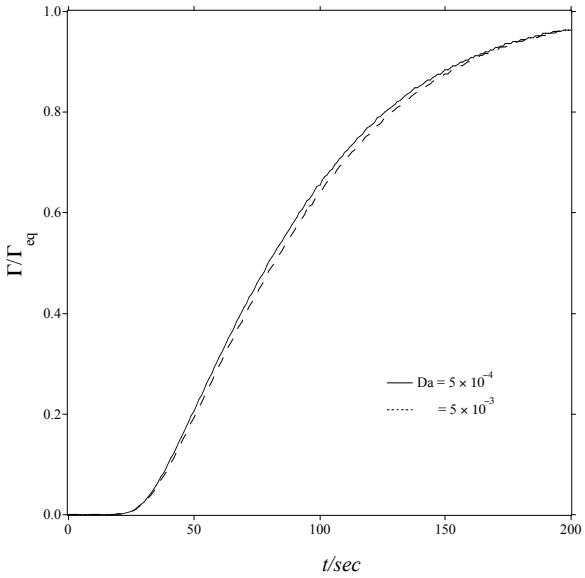

Figure 7.7. Variation of the adsorption at the end of the channel, at low Da numbers (under kinetic control). The same parameters as in Fig. 7.5 are used for the simulations; k_{on} = 10 $m^3 \cdot mol^{-1} \cdot sec^{-1}$; $D = 4 \times 10^{-11}$ and 4×10^{-12} $m^2 \cdot sec^{-1}$ for Da = 5×10^{-4} and 5×10^{-3} respectively.

The data of Fig. 7.5 can be reported as reaction-rate vs. the bound concentration plots, averaging all the values over the length of the channel. This is done in Fig. 7.6. The short initial transient period is due to the analyte passing through the channel. The reaction rate reaches its maximum when the wall is still void of analyte and then the reaction rate decreases continuously to reach zero at equilibrium. As the bound concentration was normalised by Γ_{max}, the maximum abscissa value is 1. The linear fit of the last part of the experimental data plotted in this form is the usual method for estimating kinetic constants in experimental BIACORE experiments. It is clearly shown that the ideal situation to obtain the kinetic constants is at low Da values. The plots are, in fact, very close to linearity. At high Da, a slight deviation from linearity is shown, so that the interpolation must be done in a smaller part of the curve (the last part).

In Fig. 7.7, it is shown that, at low Da values, a variation of just 1% is observed in the adsorbed analyte if D varies by an order of magnitude. This effect is more important at high Da values. When using a gel to attach a biomolecule to the surface, the kinetic rates can be miscalculated; with the SCAT this cannot happen.

7.3.2 Experimental SCAT results

The kinetics of IgG adsorption on laser ablated PET channels measured with SCAT are shown in Fig. 7.8a-d. As foreseen from the Langmuir isotherm, the equilibrium is reached sooner at higher concentrations: about 200 sec are needed when $C° = 6.67 \times 10^{-7}$ M, while 400 sec for $C° = 1.65 \times 10^{-8}$ M. All the curves were fitted with the FEM model and an adsorption rate value $k_{on} = 150$ $m^3 \cdot mol^{-1} \cdot sec^{-1}$ is found. For $C° = 6.67 \times 10^{-7}$ M, lower kinetic rates were found. This phenomenon was already found studying the adsorption by confocal microscopy: at larger coverages, the protein specific orientation needed to find an active site in the reduced available surface slows down the adsorption. The difference between experimental and simulated curves is at worst 15% in the case of $C° = 1.65 \times 10^{-8}$ M.

The kinetic rates found are one order of magnitude higher than those obtained with the confocal microscope, even though they are still under kinetic control. This can be due to a delay occurred while measuring the fluorescence and also to the fact the data collected automatically with the SCAT technique are much more numerous, allowing for a more precise determination of the rates. The reaction-rates versus bound concentration are shown in Fig. 7.9. All the curves show more or less the same linear trend (in BIACORE experiments, a concave shape of the curve is sometime observed at high concentration, meaning that the apparent association rate constant decreases as the reaction proceeds to completion. Low concentrations of the ligand are therefore recommended to obtain good results).

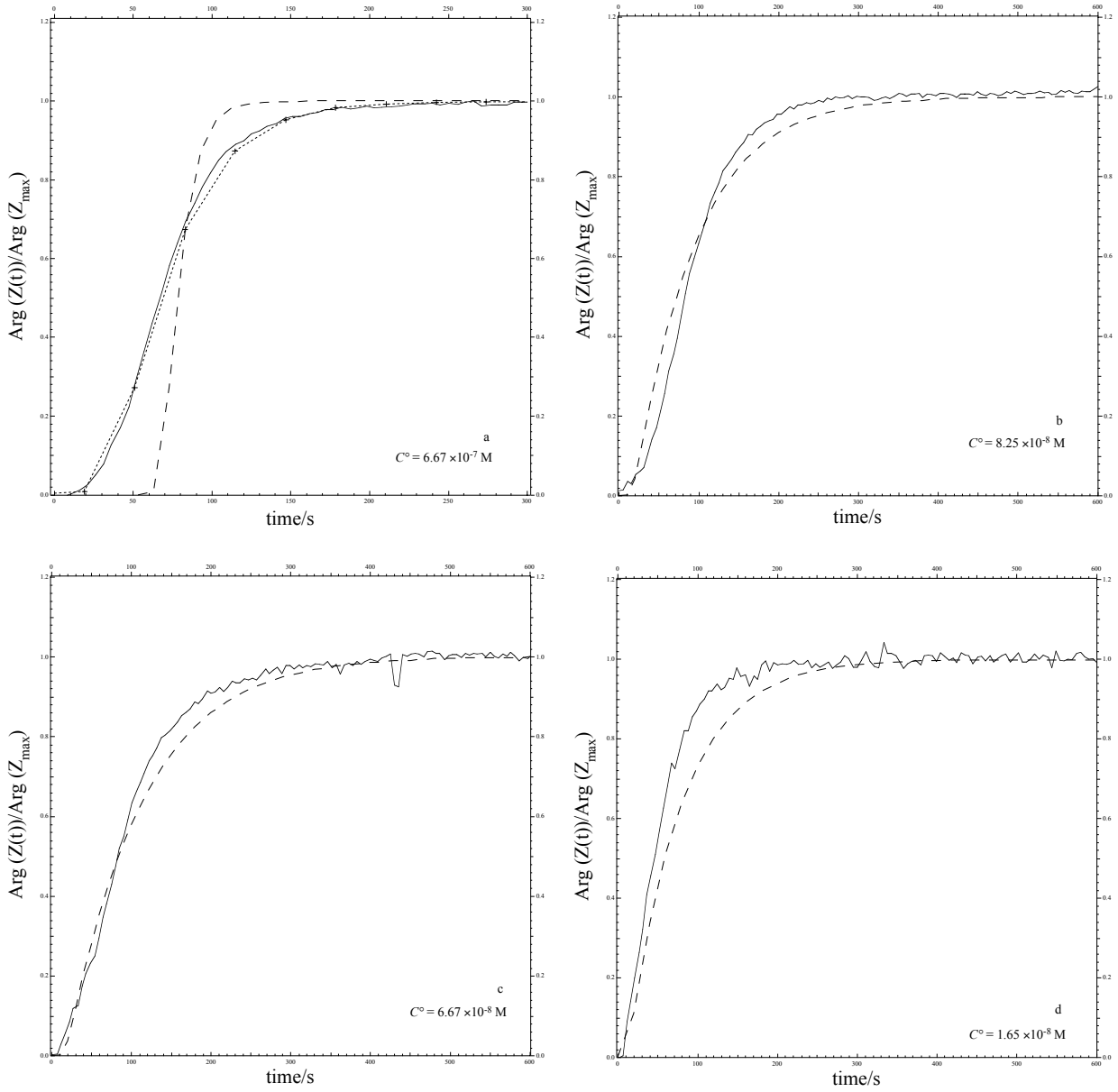

Figure 7.8. Experimental results for the adsorption of IgG antibodies on a PET microchannel by SCAT (full line). $C° = 6.7 \times 10^{-4}$, 8.25×10^{-5}, 6.7×10^{-5}, 1.65×10^{-5} mol·m^{-3} for a, b, c, d respectively; $V = 90$ μL·h^{-1}. The argument of the impedance is reported as a function of time. The simulations are run with $D = 4 \times 10^{-11}$ m^2·sec^{-1}, $\Gamma_{max} = 9.26 \times 10^{-10}$ mol·m^{-2} and $K = 1.15 \times 10^4$ m^3·mol^{-1}; these last two values are obtained from the linearisation of the isotherm of Fig. 7.11. $k_{on} = 150$ m^3·mol^{-1}·sec^{-1}, $k_{off} = 1.3 \times 10^{-2}$ sec^{-1}. The experiment at 6.67×10^{-7} mol·m^{-3} was better fitted with $k_{on} = 50$ m^3·mol^{-1}·sec^{-1} and $k_{off} = 5 \times 10^{-3}$ sec^{-1} (dotted lines – crosses). $V = 100$ μm·sec^{-1}, which corresponds to $V = 90$ μL·h^{-1} for the 2.5 mm long experimental channel.

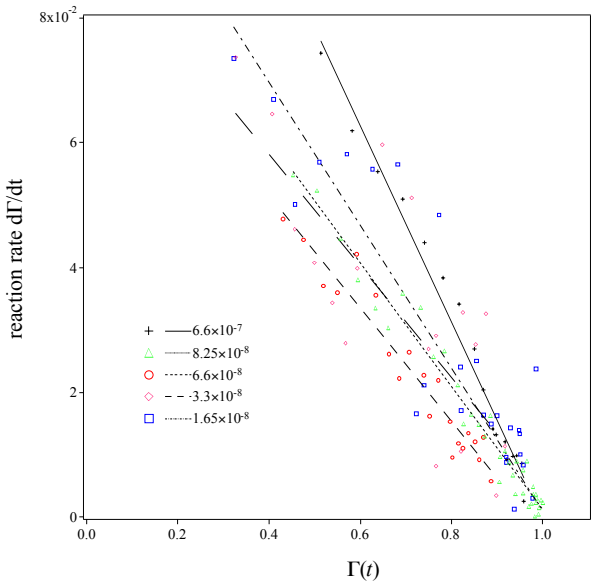

Figure 7.9. Reaction rate as a function of the bound concentration with time of the experimental results (markers) and the simulations (full lines) of Fig. 7.8.

All the curves have the same slope (slightly higher at higher concentration): the average value of the kinetic constant obtained in this way is k_{on} = 105 $m^3 \cdot mol^{-1} \cdot sec^{-1}$, quite close to the one from the model. Under the conditions of these experiments Da values were small (Da = 7.5 × 10^{-3}), therefore presenting no mass-transfer problems.

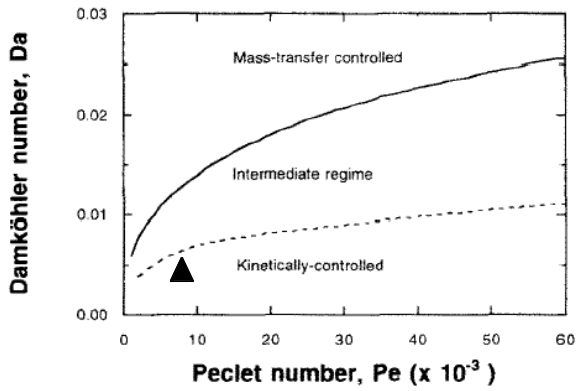

Figure 7.10. Maximum Damköhler number for operation in kinetic regime as a function of Peclet number (adapted from Yarmush).[17] The IgG adsorption on PET studied in this work is represented by the full triangle.

Yarmush plotted the limiting Da values that define kinetically, intermediate and mass-transfer controlled regimes in function of the Peclet number. It is true that in our discussion on the different regimes in chapter 4, the importance of the Peclet number has been overlooked. Anyhow, as it can be seen in Fig. 7.10, the variation of Da for a kinetic controlled process is just 0.007 for Pe varying from 0 to 6×10^4. The conditions of our experiments fall well in the kinetic controlled regime, as we stated previously.

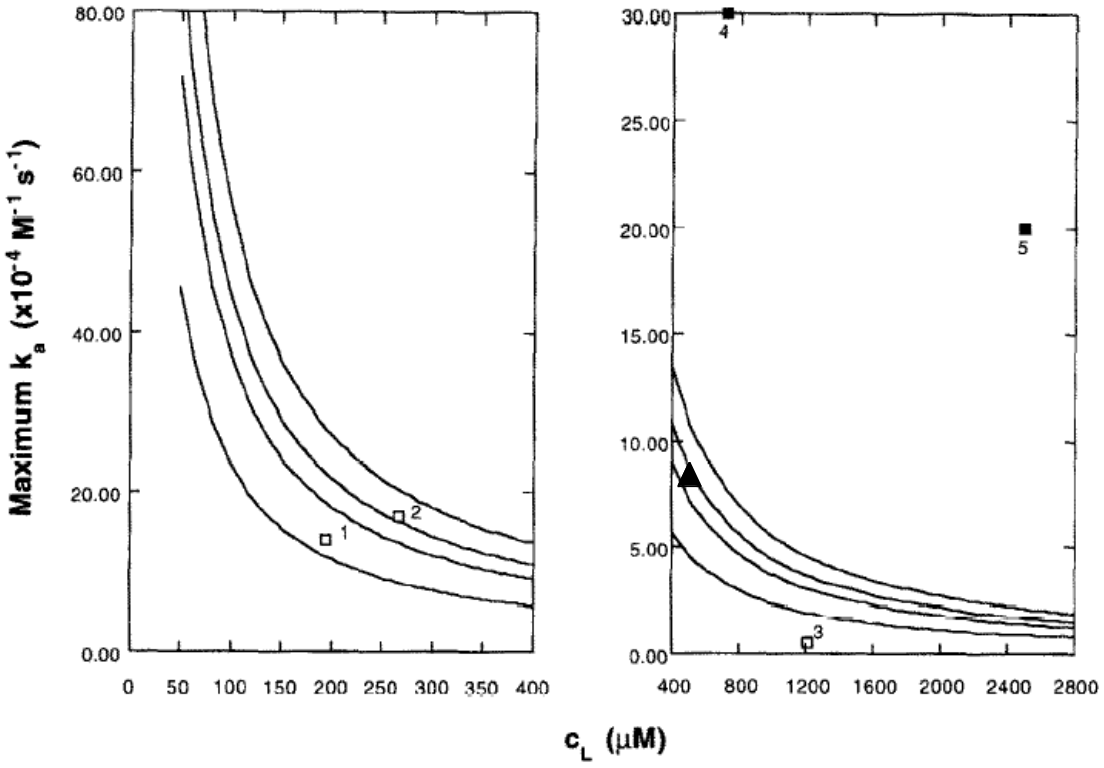

Figure 7.11. Maximum association rate constant at which the reaction took place in a kinetic regime (adapted form Yarmush).[17] Experimental points marked correspond to result reported in the literature: 1 – Karlsson et al.;[20] 2 – End et al.;[21] 3 – Cooper et al.;[22] 4 – Borrebaeck et al.;[23] 5 – Van Cott et al.[24] Open squares represent conditions in the kinetic regime and full squares represent condition in the mass-transfer-limited regime. The triangle represents the result from this work.

The operating variables at which the transition from kinetic to mass-transfer controlled regime occurs are presented in dimensional form in Fig. 7.11 for a diffusivity value of 6×10^{-11} $m^2 \cdot sec^{-1}$ (which is close to the one used in our experiment: no variations are felt in our models when D_{wall} changes so little). Even in this representation, it is evident that our experiment is under kinetic controlled regime. Yarmush reports many studies that did not keep into account the affectation in the measurements because of mass-transfer resistances (full squares in Fig. 7.11).

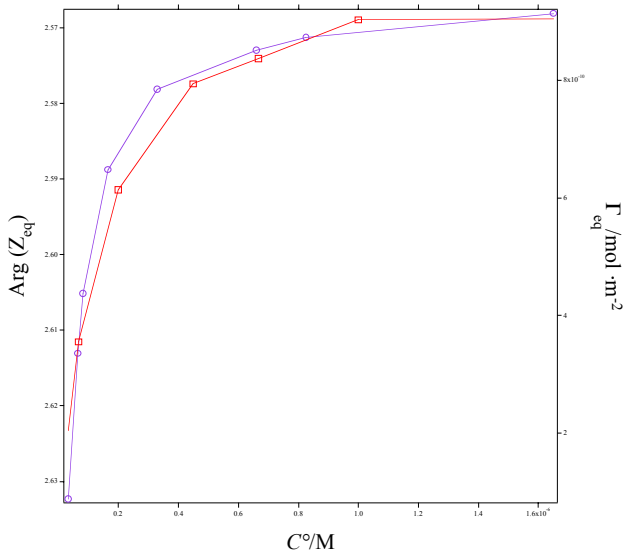

Figure 7.12. Comparison between the isotherms of IgG adsorption on PET microchannels obtained by fluorescence (on the right axis – open squares) and by SCAT (left axis – open circles).

A drawback of SCAT is that it doesn't provide direct information on the amount of bound analyte. Assuming that the thermodynamic equilibrium is reached for all the concentrations used, a comparison is made in Fig. 7.12 between the isotherm obtain by fluorescence and the SCAT measurements. In this way we will be able to quantitate the analyte adsorbed.

7.4 Conclusions

In this chapter the FEM model already described was used to simulate results obtained from surface signals in real flowing conditions, verifying that the results obtained by confocal microscopy in pseudo-flowing conditions can be trusted. The FEM model is also proved to be a powerful tool to obtain information such as the kinetic rates, from such systems.

For the experiments, a new technique introduced in this lab was used, the super-capacitance admittance tomoscopy (it is not the aim of this work to give a thorough description of it, nor of the instrument). Nevertheless, some comments about the results and the effectiveness of the technique can be made.

The SCAT doesn't need a specific phase like a gel where the ligand must be bound. In this way the simulation results can give a truthful account of the dynamic of the reaction at study. The surface where the ligand is can be of various kinds, thus allowing the study of the effects of the binding on the ligand.

Even if a 3D-adsorption phase is not present in the SCAT, it has been foreseen by the FEM model, so that a description of results obtained in gel matrixes can be provided. The determination of the kinetic constants under mass transport limitation remains in both cases intrinsically impossible.

Results of IgG adsorption on PET channels from SCAT are simulated with the FEM model. The study confirms a kinetic limited adsorption, already stated by confocal microscopy, which in turn is confirmed as a good, though more time-consuming tool to study fluorescently labelled biomolecules adsorption on a transparent support.

A comparison between the confocal microscopy and the SCAT results is given in order to build a calibration isotherm adsorption useful to quantitate SCAT results.

References:

(1) Berggren, C.; Bjarnason, B.; Johansson, G. *Biosensors & Bioelectronics* **1998**, *13*, 1061-1068.

(2) BenDov, I.; Willner, I.; Zisman, E. *Analytical Chemistry* **1997**, *69*, 3506-3512.

(3) Schmid, E. L.; Tairi, A. P.; Hovius, R.; Vogel, H. *Analytical Chemistry* **1998**, *70*, 1331-1338.

(4) Duschl, C.; SevinLandais, A. F.; Vogel, H. *Biophysical Journal* **1996**, *70*, 1985-1995.

(5) Sasaki, S.; Nagata, R.; Hock, B.; Karube, I. *Analytica Chimica Acta* **1998**, *368*, 71-76.

(6) Woodbury, R. G.; Wendin, C.; Clendenning, J.; Melendez, J.; Elkind, J.; Bartholomew, D.; Brown, S.; Furlong, C. E. *Biosensors & Bioelectronics* **1998**, *13*, 1117-1126.

(7) Lofas, S.; Johnsson, B. *Journal of the Chemical Society-Chemical Communications* **1990**, 1526-1528.

(8) Myszka, D. G.; He, X.; Dembo, M.; Morton, T. A.; Goldstein, B. *Biophysical Journal* **1998**, *75*, 583-594.

(9) Arnold, F. H.; Blanch, H. W.; Wilke, C. R. *Chemical Engineering Journal and the Biochemical Engineering Journal* **1985**, *30*, B9-B23.

(10) Wimalasena, R. L.; Wilson, G. S. *Journal of Chromatography-Biomedical Applications* **1991**, *572*, 85-102.

(11) Opong, W. S.; Zydney, A. L. *Aiche Journal* **1991**, *37*, 1497-1510.

(12) Stenberg, E.; Persson, B.; Roos, H.; Urbaniczky, C. *Journal of Colloid and Interface Science* **1991**, *143*, 513-526.

(13) Kitano, H.; Nakamura, K.; Hirai, Y.; Kaku, T.; Ise, N. *Biotechnology and Bioengineering* **1988**, *31*, 547-552.

(14) Arve, B. H.; Liapis, A. I. *Aiche Journal* **1987**, *33*, 179-193.

(15) Bianchi, F.; Wagner, F.; Hoffmann, P.; Girault, H. H. *Analytical Chemistry* **2001**, *73*, 829-836.

(16) Myszka, D. G.; Morton, T. A.; Doyle, M. L.; Chaiken, I. M. *Biophysical Chemistry* **1997**, *64*, 127-137.

(17) Yarmush, M. L.; Patankar, D. B.; Yarmush, D. M. *Molecular Immunology* **1996**, *33*, 1203-1214.

(18) Sikavitsas, V.; Nitsche, J. M.; Mountziaris, T. J. *Biotechnology Progress* **2002**, *18*, 885-897.

(19) Bard A. J., F. L. R. *Electrochemical methods : fundamentals and applications*; Wiley: New York, 2001.

(20) Karlsson, R.; Michaelsson, A.; Mattsson, L. *Journal of Immunological Methods* **1991**, *145*, 229-240.

(21) End, P.; Gout, I.; Fry, M. J.; Panayotou, G.; Dhand, R.; Yonezawa, K.; Kasuga, M.; Waterfield, M. D. *Journal of Biological Chemistry* **1993**, *268*, 10066-10075.

(22) Cooper, L. J. N.; Robertson, D.; Granzow, R.; Greenspan, N. S. *Molecular Immunology* **1994**, *31*, 577-584.

(23) Borrebaeck, C. A. K.; Malmborg, A. C.; Furebring, C.; Michaelsson, A.; Ward, S.; Danielsson, L.; Ohlin, M. *Bio-Technology* **1992**, *10*, 697-698.

(24) Vancott, T. C.; Loomis, L. D.; Redfield, R. R.; Birx, D. L. *Journal of Immunological Methods* **1992**, *146*, 163-176.

General Conclusions

To study protein adsorption in microchannels, a confocal microscope was built. With this tool we can observe the specimen one focal plane at time, eliminating the noise coming from the optical planes out of focus, so that we can obtain high signals compared to the background. This is very important in microenvironments, where the concentrations are often under the nanomolar range, and femtomoles of analyte must be detected.

This confocal microscope works exciting molecules at 650 nm wavelength. It has a horizontal resolution of about 20 microns and a vertical one comparable to the microchannel dimensions. The adsorption of fluorescent labelled proteins can be studied with it, and immunoassays with fluorescent detection can be performed, with a limit of detection in the nanomolar range.

The problem of adsorption in microsystem is approached with the help of a finite element (FEM) model. The model has been conceived for adsorption phenomena following the Langmuir assumptions, which are the more general and adaptable to different systems. As an example, even if not strictly valid for the protein adsorption, they can used also to study the immunoreaction between an antibody and an antigen.

Microchannels behave as adsorptive systems differently from ideal systems where the solute diffusion is semi-infinite. During the adsorption the solution depletes of the solute absorbing onto the walls. The solution concentration lowers as the adsorption proceeds resulting in a lower value of the adsorption compared to what expected from theory. This can lead to surprisingly low values of adsorption, and a deceptive low limit of detection for immunoassays. The FEM model provided an important amount of data that collected

together allow for drawing a picture of adsorption in microsystem. In this way we could define a parameter $\varphi = h / K\Gamma_{max}$, called the "ideality for binding of a microsystem". Through a working curve of the values of the adsorption on microchannels compared to ideal systems as a function of φ (Fig. 3-6), it is possible to know the coverage obtainable in a microsystem.

To alleviate the problem of the depletion, the adsorption can be performed in a static way and the depleted solution can be renovated many times, until the optimum coverage is reached. A parameter α, the "relative adsorbing capacity of the system", is introduced by which it is possible to predict the number of "stop-flow" steps than must be carried out to reach the optimum equilibrium. This multi step "stop-flow" procedure is simulated with the FEM model. The solution of the adsorbing species can also be continuously flown into the microchannel. The "stop-flow" is compared to the flow mode in terms of waste of product and time to reach the desired adsorption value. For the continuous flow, two criteria for the fluid velocity are found that should be respected in order to avoid a waste greater than with the "stop-flow" method.

The confocal microscope is used to observe IgG antibody adsorption on PET microchannels and the data obtained have been fitted with the FEM model, revealing a kinetic limited process. The value of adsorption in PET microchannels can be improved as well as the activity of the antibodies attached to the polymer. With this aim, the channels were coated with TiO_2 nanomaterials (anatase TiO_2 and amorphous TiO_2). The IgG adsorption is studied in these systems under different pH and salt concentrations, leading to the conclusion that adsorption on PET and anatase TiO_2 occurs through electrostatic interactions, possibly helped by hydrophobic forces, as it normally occurs

with proteins (adsorption on oxidised PET is mainly due to covalent and electrostatic forces). On amorphous TiO_2 electrostatic forces can play an important role. On the titania phases, the IgG adsorption is 3 times higher and the protein activity is doubled with respect to PET.

The "stop-flow" is used to improve the limit of detection of immunoassays performed in PET microchannels and in microchannels coated with the TiO_2 nanomaterials. The parameters φ and α are used to predict the coverage obtainable in each system and the number of steps needed to have the best response.

The results confirm the prediction: PET is a phase that adsorbs little, so that little improvement is expected and is obtained. The titania phases allow for an improvement of the limit of detection of 1 order of magnitude, as if an enzyme label was used.

The FEM model was used to fit the results obtained with a novel immunosensor developed in our lab, which measures the variation of capacitance occurring in the microchannel while the adsorption occurs. The fitting of the data allows to knowing the kinetic rates of adsorption and desorption of the system studied. The FEM model has been also compared to other models for biosensors: as it is a flexible tool, it can be used to study adsorption even in 3D phases like gels.

Andrea Lionello
Rue des Echelettes 8
1004 Lausanne
(021)624.85.52
andrea.lionello@epfl.ch

Personal information

Born on May 26, 1972 in Genoa, Italy. Italian citizen.
Married, father of one child (Leonardo, born February 27, 2004).

Education

Laurea in Chimica (July 1999). *University of Genoa*.
Dissertation in inorganic chemistry: "Crystal structure of the RCuZn, RAgZn and RAgAl intermetallic compounds (R = rare earth metals)".

Maturità classica (July 1991). *Liceo Classico G. Mazzini, Genoa.*

Employment

Research grant at the Italian National Research Centre (2000-2001) *Genoa, Italy*.
Study of superficial properties of metallic and ceramic materials to produce joints.

Publications

Lionello A., Josserand J., Jensen H., et al., Dynamic Protein Adsorption in Microchannels. *Lab on a Chip* 2005, *in press*.

Lionello A., Josserand J., Jensen H., et al., Protein Adsorption in Static Microsystems: Effect of the Surface to Volume Ratio. *Lab on a Chip* 2005, *5*, 254-260.

Costa G.A., Mele P., Lionello A., et al., Wetting of YBCO by liquid silver, *International Journal of Modern Physics* B 17 (4-6): 960-965.

Leisure activities

Ski de randonnée, cycling, reading.